

The Pennsylvania State University  
The Graduate School  
Department of Crop and Soil Sciences

**INTEGRATED APPROACH TO IDENTIFYING  
SUBSURFACE FLOW IN A FOREST CATCHMENT**

A Dissertation in  
Soil Science  
by  
Jun Zhang

©2011 Jun Zhang

Submitted in Partial Fulfillment  
of the Requirements  
for the Degree of  
Doctor of Philosophy

December 2011

The dissertation of Jun Zhang was reviewed and approved\* by the following:

Hangsheng (Henry) Lin  
Associate Professor of Hydropedology/Soil Hydrology  
Dissertation Advisor  
Chair of Committee

Guoray Cai  
Associate Professor of Computer Science and Engineering

Jack Watson  
Professor of Soil Science  
Head of the Department of Crop and Soil Sciences

Gary Petersen  
Distinguished Professor Emeritus of Soil and Land Resources

Max Schlossberg  
Associate Professor of Turf grass Nutrition/Soil Fertility

\*Signatures are on file in the Graduate School

## ABSTRACT

During the last three decades, significant progress has been made in understanding the mechanism of subsurface lateral flow (SLF). However, the spatial and temporal occurrence of SLF remains poorly understood because of the complex subsurface heterogeneity and the lack of appropriate tools to identify such heterogeneity. The overall goal of this study is to develop an integrated hydrologic and geophysical database that can elucidate spatial and temporal patterns of SLF at the Shale Hills Critical Zone Observatory (CZO). Specifically, this study assembles a large database of Ground Penetrating Radar (GPR) images and real-time soil moisture monitoring, which is used to address the following four research objectives: 1) to identify spatial and temporal occurrence of SLF, 2) to investigate flow patterns in two contrasting soils-landform units, 3) to study the effect of soil horizonation on the seasonal change of GPR signals, and 4) to develop a new software to process, display, and interpret time-lapsed GPR data.

Under objective 1), the direct evidence of SLF was revealed by comparing real-time soil moisture storage change in each monitored soil horizon at each site with rainfall inputs. Results indicated that SLF was ubiquitous across all the monitoring sites and 52% of 97 rainfall events from 2007 to 2009 produced SLF. However, individual monitoring site showed spatial and temporal variation in the occurrence of SLF, which was related to soil type, hillslope location, rainfall characteristics, and initial soil moisture. The results also clearly showed a rainfall threshold to initiate SLF, which increased from 1.1 to 2.3 mm from wet to dry seasons. Although SLF occurred at each site, only 9 out of the 97 rainfall events analyzed showed the connectivity from the hilltop to the valley floor. Under wet condition, only 1.1~2.3 mm rain could connect SLF from the hilltop to the valley floor, while under dry condition, 14.6 mm rain was needed to deliver water from the hilltop down to the valley floor. In addition, we found that the layers where SLF most likely to occur also varied among different hillslope locations that had different

soil types: SLF in the shallow Weikert soil occurred mostly in the R horizon, while in the deep Rushtown soil SLF frequently occurred in the Bw and C horizons. This study enhanced the understanding of the mechanism, actual location, and potential flow pathway of SLF in a forested catchment and can improve process-based hydrological modeling.

Under objective 2), time-lapsed GPR imaging was combined with real-time soil moisture monitoring to identify SLF pathways in two contrasting transects of soils. The real-time soil moisture monitoring showed that SLF occurred in top 20-cm soil after artificial water infiltration into the shallow Weikert soil in a planar hillslope (30% slope), whereas vertical flow dominated in the deep Rushtown soil located in a concave hillslope (swale) with 15% slope. The time-lapse GPR radargrams revealed the general infiltration wetting front and preferential flow pattern that were significantly different between the two types of soils and hillslopes, which were then confirmed by simulation modeling results. Through comparing simulated radargrams generated from four conceptual flow models with the field observed GPR data, we were able to confirm that subsurface lateral macropore flow was dominant in the shallow Weikert soil, while a combination of vertical macropore flow and lateral matrix flow was dominant in the deep Rushtown soil under the experimental conditions of this study. Time-lapsed GPR is proved to be a useful methodology for improved understanding of hydrologic connectivity in the subsurface, which can facilitate the formulation and test of different conceptualizations of subsurface network modeling.

Under objective 3), GPR was combined with high resolution real-time soil moisture monitoring to examine seasonal changes of GPR signals at the interfaces of soil layers in two different soils. The results indicate that in the deep Rushtown soil reflection in the BC-C horizon interface became clearer as soil became wetter. High resolution real-time soil water monitoring and field observations indicated that this increased reflection may be due to SLF above and below the BC horizon, which increased the contrast along the interface. In contrast, in the shallow Weikert soil, reflections at the soil -bedrock interface and weathered-unweathered rock interface

became intermittent as soil became wetter. This was likely caused by non-uniform distribution of water into the fractures of the shale bedrock, which created locally strong contrasts between soil and bedrock thus leading to point scatter of GPR reflection. The results also indicated optimal time to detect soil horizons in the two soils studied. Wet condition without rainfall event is optimal for detecting the BC-C interface in the Rushtown soil, while dry condition is optimal for detecting the soil-bedrock and weathered-unweathered interface in the Weikert soil. Our results also indicated that seasonal GPR survey with high resolution real-time soil water content monitoring is a promising methodology for understanding, explaining and conceptualizing hydrologic processes in the hillslope.

Under objective 4), MATLAB-based software called Time-lapsed GPR (TGPR) has been developed as an alternative to expansive commercial software to process, display, and interpret GPR data collected in the Shale hills catchment. The TGPR can process both 2D and 3D GPR survey data and has ability to batch process surveys containing several profiles instead of single file as the commercial software usually does. With user-friendly interfaces, the TGPR can allow users to interactively edit radargrams and manually or automatically correct topography. The TGPR also provides several utilities to enhance 2D and 3D visualizations of GPR data. These utilities include trace view, wiggle view, and image view of 2D data; slice view, cube view, and transparent view of 3D data; ten built-in color table to enhance image display quality; layer editing on 2D image. Furthermore, with structured programming, TGPR can be easily expanded and customized.

Overall, high temporal resolution real-time soil moisture monitoring data can be used to identify the occurrence of SLF, analyze SLF processes, and seasonal soil moisture change at the point scale. Combined with high spatial resolution GPR survey, spatial flow pattern can be identified, flow mechanism can be confirmed, and flow pathways can be traced at the hillslope scale. Such an integrated approach that combines the point and hillslope scales investigations

provides valuable insights into the understanding of the complex and dynamic subsurface heterogeneity and how it impacts hydrologic processes.

## TABLE OF CONTENTS

LIST OF FIGURES .....	x
LIST OF TABLES .....	xiv
ACKNOWLEDGEMENTS .....	xv
Chapter 1 .....	1
Introduction.....	1
Goal and Objectives .....	1
Literature Review.....	3
Subsurface storm flow .....	3
Ground Penetrating Radar (GPR) .....	6
Hydrologic applications of GPR.....	8
Thesis Organization .....	12
References.....	13
Chapter 2 .....	20
Hydrological and Geophysical Databases for the Shale Hills Catchment .....	20
Introduction.....	20
Shale Hills Time Series Database (SHTSD).....	22
Background.....	22
Function and GUI design.....	23
Database Design and table structure .....	24
Shale Hills GPR Image System (GPRIS) .....	26
Background.....	26
Function and GUI design.....	26
Data organization and structure .....	27
References.....	28
Chapter3.....	44
Subsurface Lateral Flow in the Shale Hills Catchment as Revealed by Real-Time Soil Moisture	
Monitoring .....	44
Abstract.....	44
Introduction.....	45

Material and Methods .....	47
Study area and soil moisture monitoring sites .....	47
Data analysis .....	49
Results .....	52
Spatial and temporal occurrence of subsurface lateral flow .....	52
Effect of rainfall and seasonal soil moisture change on subsurface lateral flow .....	53
Effect of soil horizon on subsurface lateral flow occurrence .....	54
Connectivity from upslope to downslope .....	54
Discussion .....	55
Ubiquitous subsurface lateral flow .....	55
Pathway and connectivity along the hillslope .....	56
Implication for hydrologic modeling .....	57
Conclusions .....	58
References .....	59
Chapter 4 .....	78
Hillslope Subsurface Flow Revealed by Time-lapsed Ground Penetrating Radar and Real-Time Soil Moisture Monitoring .....	78
Abstract .....	78
Introduction .....	79
Material and methods .....	81
Study area and soils .....	81
Instruments .....	82
Experimental setup and time-lapse GPR survey .....	83
Simulation of GPR radargram using different flow models .....	84
Results and discussion .....	87
Soil water content changes and GPR radargrams in the Rushtown soil transect .....	87
Soil water content changes and GPR radargrams in the Weikert soil transect .....	90
Simulated vs. observed GPR radargrams .....	94
Summary and Conclusion .....	97
References .....	98
Chapter 5 .....	116
Seasonal GPR Signal Changes in Two Soils and Hillslopes .....	116
Abstract .....	116

Introduction.....	117
Materials and Methods.....	119
Study site and soils .....	119
Experiment setup .....	120
GPR instrument and survey .....	121
Subsurface Layer identification .....	121
Results and Discussion .....	123
Layer validation .....	123
Seasonal GPR signal change in the deep Rushtown soil .....	124
Seasonal GPR signal change in the shallow Weikert soil.....	125
Implications for understanding hydrological processes in contrasting soils and hillslopes .....	126
Summary and conclusion .....	128
References.....	130
Chapter 6.....	147
A MATLAB-based Software for Processing, Displaying, and Interpreting GPR Data.....	147
Abstract.....	147
Introduction.....	148
Program structure.....	149
Main features .....	150
2D or 3D survey.....	150
Interactively editing .....	151
Manual or auto topography correction.....	152
Filtering.....	153
2D radar display.....	153
3D radar Display.....	154
Examples.....	154
Summary .....	156
References.....	157
Chapter 7.....	168
Overall Summary and Future work.....	168
Overall Summary .....	168
Future Work.....	170

## LIST OF FIGURES

Figure 1-1: A general framework for the integrated study employed in this study.....	19
Figure 2-1: Outline of SHTSD application program interfaces (gray box) and functions (orange box).....	33
Figure 2-2: Demonstration of interfaces for SHTSD application program.....	36
Figure 2-3: A. Outline of Shale Hills time series database structure. B. Table relationships. ....	37
Figure 2-4: Outlines of interfaces (gray box) and functions (orange box) in GPRimagesys.....	38
Figure 2-5: A. Main interface with five functions labeled; B. Site info interface with three functions.....	39
Figure 2-6 : A. Radargram display in transect survey; B. Radargram display in grid survey; C. Radargram display in infiltration survey .....	40
Figure 2-7 : Data structure in GPRimagesys.. .....	41
Figure 2-8 : Illustration of BasicInfo.txt .....	42
Figure 2-9 : Illustration of Infiltration.txt .....	43
Figure 3-1: Location of the Shale Hills catchment and the study hillslope .....	68
Figure 3-2: A. An example of strong subsurface lateral flow occurred in site 15;B.An example of weak subsurface flow occurred in site 51left.....	69
Figure 3-3: Relationship between rainfall separation time and mean rainfall duration .....	70
Figure 3-4: Number of occurrence of strong and weak subsurface lateral flow in each of the 9 monitoring sites during wet, transition, and dry periods.....	71
Figure 3-5: Number of occurrence of subsurface lateral flow events at each of the 9 monitoring sites during wet, transition, and dry periods. ....	72
Figure 3-6: A. Relationship between rainfall amount and total storage increase (ds) during subsurface lateral flow (SLF) at each site during different periods. ....	73
Figure 3-7: Relationship between rainfall amount and storage increase in different horizons at each site during all of the 97 rainfall events. ....	74
Figure 3-8: Example of the disconnected flow from the hilltop to the valley floor.....	75
Figure 3-9: Example of the connected flow from the hilltop to the valley floor during a rainfall event.....	76

Figure 4- 1: An overview of the Shale Hills Critical Zone Observatory and the locations of two types of soils and hill slopes investigated .....	105
Figure 4- 2: Schematic of infiltration experiment setup in the concave (swale) hillslope with the Rushtown soil series .....	106
Figure 4- 3: Schematic of infiltration experiment setup in the planar hillslope with the shallow Weikert soil series.....	107
Figure 4- 4: Time series of soil moisture readings at different depths during the infiltration experiment in the Rushtown soil transect. ....	108
Figure 4- 5: Geometry of GPR simulations using different conceptual flow models for the Rushtown soil transect: A. Vertical matrix flow model; B. Vertical macropore flow model; and C. Combination of vertical macropore flow model and lateral matrix flow model. ....	109
Figure 4- 6: Geometry of GPR simulations using different conceptual flow models for the Weikert soil transect: A. Vertical matrix flow model; B. Vertical macropore flow model; C. Lateral matrix flow model; and D. Lateral macropore flow model.. ....	110
Figure 4- 7: A. Time-lapsed GPR images before and after the infiltration in the Rushtown soil transect. B. Differential radargrams between 4, 15, or 30 min after the infiltration, respectively, and that of initial condition before infiltration.....	111
Figure 4- 8: Time series of soil moisture readings at different depths during the infiltration experiment in the Weikert soil transect. Red arrow indicates the beginning of water infiltration and dark blue arrow indicates the end of the infiltration experiment. ....	112
Figure 4- 9: A. Time lapse GPR images before and after the infiltration in the Weikert soil transect. B. Differential radargrams between 5, 15, or 30 min after the infiltration, respectively. ....	113
Figure 4- 10: Simulated GPR radargrams using different flow models for the Rushtown soil transect and their comparisons to the real GPR radargrams. ....	114
Figure 4- 11: Simulated GPR radargrams for the Weikert soil transect using four conceptual flow models and their comparisons to the real GPR radargrams. ....	115
Figure 5-1: A. The study sites and locations of GPR survey grids. B. Layout of the Rushtown grid. C. Layout of the Weikert grid. D. EC-5 sensor location in Rushtown soil pit. E. EC-5 sensor location in Rushtown soil pit. ....	135
Figure 5-2: Reflection coefficient $r$ change in Rushtown soil .....	136
Figure 5-3: Reflection coefficient $r$ change in Weikert soil.....	137

Figure 5-4: A. Soil layers identified in the Rushtown soil B. the real time soil water content monitoring when GPR survey was conducted in Oct.2008. ....	138
Figure 5-5: A. soil layers identified in the Weikert soil. B. the real time soil water content monitoring when GPR survey was conducted in Oct. 2008. ....	139
Figure 5-6: A. Photograph showing weathered rock and unweathered rock in Weikert soil. B. soil profile in Rushtown soil.....	140
Figure 5-7: A.Seasonal GPR signal change in Rushtown soil B. Corresponding soil moisture content monitoring during GPR survey .....	141
Figure 5-8: A. Seasonal soil water content monitoring in Rushtown soil. B. soil water content increase in C horizon .....	142
Figure 5-9: A.Seasonal GPR signal change in Weikert soil B. Corresponding soil moisture content monitoring during GPR survey .....	143
Figure 5-10: Illustration of lateral flow through Bw3 horizon in Rushtown soil .....	144
Figure 5-11: Wet and dry GPR pattern in Rushtown (top) and Weikert soil (bottom).....	145
Figure 5-12: Optimal time to detecting soil horizon. A. BC-C interface in Rushtown soil at wet condition (April 24th, 2009) B. weathered-unweathered bedrock interfaces in Weikert soil at dry condition (October 20th, 2008).....	146
Figure 6-1: Main interface and the entry point of TGPR.....	158
Figure 6-2: Physical data structure in the hard drive. ....	159
Figure 6-3: A. GUI of marker edit displaying marker information and interactively adding marker B. GUI of time zero adjustment displaying time zero pick at first positive peak C. GUI of marker interpolation displaying trace information and radargram after interpolation....	160
Figure 6-4: A. manual topography correction by drawing relation elevation line;B. automatic topography correction by importing topography data file .....	161
Figure 6-5: A. Interactive fitting of a diffraction hyperbola (red lines) with observed hypobola and velocity is displayed in red font. B. color display radargram with time axis and depth axis and the blue dash line indicate the presence of layer. C. wiggle display of radargram.....	162
Figure 6-6: A. snap shot of interpolation along x-y plane;B. slice view along x,y and z direction;C. cube view of 3D data;D. slice view with increase color saturation and transparency ....	163
Figure 6-7: A. 2D radargrams of the Rushtown soil processed by the TGPR under dry and wet conditions; B. 2D radargrams of the Rushtown soil processed by the GPR-SLICE under dry and wet conditions.....	164

Figure 6-8: A. 2D radargrams of the Weikert soil processed by the TGPR under dry and wet condition. B. 2D radargrams of the Weikert soil processed by the GPR-SLICE under dry and wet condition..... 165

Figure 6-10: A. 3D slice view of the Weikert soil processed by the TGPR under dry and wet condition B. 3D slice view of the Weikert soil processed by the GPR-SLICE under dry and wet condition..... 167

## LIST OF TABLES

Table 2- 1 List of field name and descriptions relations for Shale Hills Time Series Database....	30
Table 3-1: Soil and landscape features at 9 monitoring stations.....	62
Table 3-2 : Statistics of the 97 rainfall events selected from 1/1/2007 to 12/31/2009 and SLF occurrence.....	63
Table 3-3: Statistics of SLF occurrence at each monitoring site from 2007-2009. ....	64
Table 3-4: Statistics of the occurrence of strong subsurface lateral flow during 97 rainfall events from 2007 and 2009.....	66
Table 3-5: Statistics of the occurrence of connectivity events .....	67
Table 4-1: Soil profile characteristics of the two soil series investigated in this study. ....	102
Table 4-2 : Summary of soil moisture sensor responses at different depths during the infiltration experiment in the Rushtown soil transect.....	103
Table 4-3 : Summary of soil moisture sensor responses at different depths during the infiltration experiment in the Weikert soil transect. ....	104
Table 5-1: Soil profile characteristics of the two soil series investigated in this study .....	134

## **ACKNOWLEDGEMENTS**

I would like to thank my advisor, Dr. Henry Lin, for his guidance as well as the opportunities he provided me with during my Ph.D. journey. I would also like to thank my graduate committee for all of their helpful suggestions and insight. Their knowledge intimidated me, their collegiality always reassured me.

Many thanks to my family and friends for without their patience, love, support, and encouragement, this would have been difficult to complete.

I would also like to thank Dr. Lin's Hydropedology lab group and many others that helped to make this degree possible for me including James Doolittle in USDA-NRCS.

Finally, I would like to thank everyone in the Crop and Soil Science Department for providing such an enjoyable learning atmosphere.

This study was partially supported by the NSF Shale Hills Critical Zone Observatory (EAR-0725019).

## **Chapter 1**

### **Introduction**

#### **Goal and Objectives**

Subsurface storm flow in hillslopes has been observed to be a dominant stream flow generating process (Whipkey, 1965; Weyman, 1973; Bonell, 1998; Jones and Connelly, 2002; Weiler et al, 2004). Subsurface flow also plays an important role in transporting contaminant and nutrients into surface water (Stieglitz et al., 2003; Ocampo et al., 2006). Although subsurface flow is now recognized as a widely observed phenomenon in natural hillslopes, particularly in steep catchments, there remain questions regarding when and where subsurface flow occurs and how it is related to different soil types and landscape positions in a catchment. Understanding spatial and temporal pattern of flow process is not an easy task due to the complex heterogeneity and the lack of appropriate tools to identify the subsurface heterogeneity and its impact on flow.

Hydrologic monitoring such as soil moisture monitoring can provide high temporal resolution of flow-related process. However, such monitoring is generally based on point-based measurements and is often invasive when installing the instrument (e.g., Freer et al, 2002; Gish, et al., 2002). As a result, spatially-varying occurrence of subsurface flow could not be easily and precisely determined (Lin, 2010). Geophysical survey provides non-invasive, spatially exhaustive information about subsurface features (Grasmueck, 1996; Truss, et. al., 2007; Poisson et al., 2009). However, geophysical survey has coarse temporal resolution compared with hydrologic monitoring. As a result, temporally-varying occurrence of subsurface flow could not be captured.

Therefore, integrating hydrologic and geophysical techniques can address some of shortcomings based only on either hydrologic or geophysical data.

The overall goal in this study is to integrate hydrologic and geophysical data to elucidate spatial and temporal subsurface flow process in the Shale Hills Critical Zone Observatory (CZO) in central Pennsylvania. Specifically, time-lapsed geophysical data are collected using Ground Penetrating Radar (GPR) in combination with high resolution time series of soil moisture content. The overall frame work is illustrated in Figure 1-1. The GPR image shows the spatial pattern of subsurface reflection, which is the results of subsurface features and spatial distribution of water. Soil moisture dynamics reflect the influence of subsurface features on water flow in soils and temporal distribution of water. By coupling GPR image with soil moisture dynamics, the spatial-temporal pattern of soil water movement in the subsurface can be better identified and explained.

Four specific research objectives are:

1. To identify the occurrence of subsurface lateral flow in space and time;
2. To investigate subsurface flow pattern in two contrasting types of soils and hillslopes;
3. To understand the effect of soil horizonation on the seasonal change in GPR signal;
4. To develop customized software for efficient processing, displaying, and interpreting

GPR data.

Under objective 1, real-time soil moisture monitoring in multi-depths at different locations in selected hillslopes were used to reveal the occurrence and frequency of subsurface lateral flow and the soil layers that favor lateral flow. Under objective 2, real-time soil moisture monitoring was used to explain observed GPR image patterns in combination with GPR simulations to test various hypotheses of subsurface flow paths. Under objective 3, subsurface feature was identified by GPR along with long-term soil moisture monitoring, and subsurface flow mechanism was inferred based on the integrated data analysis. Under objective 4, a user-

friendly GPR software was developed to facilitate the use and interpretation of time-lapsed GPR images.

## **Literature Review**

### **Subsurface storm flow**

Subsurface storm flow has many terms in the literature such as interflow, lateral flow, subsurface runoff or soil water flow (Weiler, 2006). Definition by Freeze (1972) was ‘that part of the lateral inflow derived from water that infiltrates the soil surface and moves laterally through the upper soil horizons toward the stream channels as unsaturated flow or shallow perched saturated flow above the main groundwater level’. The importance of subsurface storm flow on runoff generation in forest environment was first recognized by Switzerland hydrologist Engler (1919). Hursch and Brater (1941) were the first to quantify the role of subsurface storm flow in watershed. The detailed field studies for understanding the physical processes of subsurface runoff generation began to emerge since International Hydrological Decade (IHD) in sixties of last century (Weiler, 2006)

Currently, subsurface storm flow is considered to be ubiquitous especially in the steep and humid catchment (McDonnell, 1990; Bonell, 1998; McGlynn, et al., 2002; Kienzler and Naef, 2008). Many studies suggested that the occurrence and intensity of subsurface lateral flow are affected by soil properties, topography, and initial soil water content.

Soil properties include soil macropore properties, soil laying and soil depth. Soil macropores are referred as pores with diameters  $> 2\text{mm}$  and lengths  $> 2\text{cm}$ , which are formed by decayed and live roots, subsurface erosion, surface bedrock fractures, and animal burrows (Sidle et. al, 2001). Although individual macropore that make up preferential flow systems are typically very short, they are able to ‘connect’ over relatively long slope distances through various

mechanisms over relatively long hillslope distances (Noguchi *et al.*, 1999). Such mechanisms include: (i) interaction with the surrounding or adjacent soil (ii) contact with living and decayed roots; (iii) formation of a perched water table above bedrock, between A and B horizons; (iv) interaction with water moving through bedrock fractures; (v) interconnections with humus in the organic horizon. Soil pipes are large continuous macropores. Numerous studies have demonstrated significant hydrological fluxes attributable to pipe flow. For example, Kitahara *et al.* (1994) found that the ratio of pipe flow to total hillslope discharge for each storm increased with an increase in total amount of rainfall. Negishi *et al.* (2007) found soil pipes were estimated to have contributed approximately 50% of runoff. Soil layering has significant impacts on subsurface water movement because significant changes in texture or density across the boundary of two adjacent layers could noticeably alter water distribution. Brown *et al.* (1999) found rapid delivery of water through O-horizon to stream during summer rainstorms through tracer experiment. By using crest piezometers along slope, while Todd *et al.* (2000) identified the formation of perched water table at the clay rich B horizon that led to saturated flow downslope through more permeable upper A horizon. Based on the soil moisture monitoring, Lin (2006) found subsurface lateral flow at O-A or A-B horizon interfaces.

Topography has long been known as important control of flow direction. However, most of past research focused on surface topography, while more recent studies have indicated that subsurface topography (such as bedrock topography) was distinctly different from surface topography and that the bedrock topography has a considerable influence on local hydrological gradients and therefore may dominant subsurface flow directions. For instance, Freer *et al.* (2002) reported that total trench flow including macropore flow and matrix flow was correlated to contributing area of bedrock topography instead of surface topography in Panola mountain research watershed. Buttle and McDonald (2002) found that a saturated layer with thin soil may quickly develop above the lithic bedrock on forested slopes on the Canadian Shield. Haga *et al.*

(2005) demonstrated that saturated subsurface flow above soil–bedrock interface was dominant subsurface runoff in a small catchment in Mizugaki research watershed. Tromp-van Meerveld and McDennell (2006b) proposed the fill and spill hypothesis to explain the effect of bedrock topography on the hillslope-scale connectivity of subsurface saturated areas.

Soil moisture plays an important role in the initiation and connectivity of subsurface flow. Newman et al (1998) found that when soils were at or near saturation (greater than ~33% volumetric water content), very large volume of SLF can be produced. Grayson et al. (1997) studied the effect of temporal variation in soil moisture on the spatial patterns of soil moisture. In their study, two spatial pattern of soil moisture were proposed. One was the lateral flow-dominated spatial pattern and the other was vertical flow-dominated spatial pattern. They suggested that the transition between two patterns was likely to be in the range of relative soil saturation from 0.6 to 0.8. Study by McNamara et al. (2005) indicated that soil moisture status was related to the hillslope hydraulic connectivity: Low rates of water input to the soil during the winter allow dry soil regions to persist at the soil–bedrock interface, which act as barriers to lateral flow. Once the dry-soil flow barriers are wetted, whole-slope hydraulic connectivity is established, then lateral flow occurs, and upland soils are in direct connection with the near-stream soil moisture.

An important recent advancement is the recognition that the relationship between threshold value and hydraulic connectivity is a necessary condition for the initiation of subsurface flow. Sidle et al. (2000) found that lateral preferential flow occurs only after the hydrologic threshold is reached and subsurface pathways are connected. They proposed a conceptual network model with a series of nodes that link the preferential flow pathway. Three levels of node were proposed according to their easiness of switch on (essentially not switch on, require moderate wetness to switch on , require most wetness to switch on). Tromp-van Meerveld and McDennell (2006a) explicitly documented a threshold relationship between subsurface lateral

flow initiation and rainfall based on analysis of 147 rainstorms. Later Lehmann et al. (2007) applied the percolation theory to demonstrate such threshold behavior.

### **Ground Penetrating Radar (GPR)**

Ground penetrating radar (GPR) is a geophysical tool that uses high frequency electromagnetic (EM) radiation to produce high-resolution images of subsurface structure. GPR transmits pulse of energy into subsurface and records the subsequent reflections. During electromagnetic wave propagation, some of the electromagnetic wave directly transmits to receiving antenna through the air, and this is known as the airwave. Some wave, known as the ground wave, propagates to the receiving antenna through the soil along the soil-air interface and part of wave is reflected back to the receiving antenna after transmitting into the deep subsurface (Huisman et al. 2003). The energy reflected back is affected by electric conductivity, dielectric permittivity and magnetic permeability of the subsurface medium. For most soils magnetic permeability can be negligible (Powers, 1997) and dielectric permittivity has the most significant impact on the recorded GPR response. The dielectric permittivity of soil materials is strongly dependent upon moisture content. As a consequence, the amount of energy reflected back is greatly influenced by the abruptness and difference in moisture contents that exist between soil horizons, layers or features.

Ground penetrating radar system is conceptually simple. A GPR system consists of a transmitting unit, a receiving unit, a data display unit and a control unit that controls signal transmitting, receiving, converting and data storage. The objective of GPR system is to generate reflected amplitude versus time after excitation and form images of the subsurface. The image is two –dimensional data. A column in the image is called one trace or one scan, which records amplitude variation along depth at certain location. The image, which delineates subsurface profile that GPR pass through, is an ensemble of each trace collected while the antenna is moving.

According to implementing strategy of antennas, GPR has four operating modes..

The first is called single offset (also called common offset or fixed offset) method. In this method the distance between transmit and receive antenna is fixed when GPR is moving along a survey line. The moving system along the survey delineates the spatial variation in subsurface since variation in dielectric value causes partial reflection of the transmitted signals. Single offset survey can rapidly collect data and display the reflection as an image (radargram) from which it is possible to detect linear and point reflectors. The linear reflector is a strong and continuous band appeared in the image and usually indicates existence of a continuous medium such as soil-bedrock interface or a clay layer which has different dielectric constant to the surrounding medium. A point reflector is a hyperbolic shape appeared in the image and usually indicates existence of an anomaly in the part of survey line such as metal plate or tree root which also has significant dielectric contrast to the surrounding media. When multiple hyperbolas interweave together, crisscross pattern will appear in radar image, which indicate existence of multiple anomalies in subsurface. Single offset survey is the most commonly used and simplest way to apply GPR in the field. However, when applying this method to estimate the velocity of transmitted wave to certain reflector, the depth to reflector must be known a priori.

The second is called multi-offset method. In this method the distance between transmit and receive antenna is variable when GPR is moving along traverse line. If the receive antenna and transmit antenna move the same distance along certain point during the survey, this method is called common middle point (CMP). If one of antennas is fixed and the other is move stepwise, this method is called Wide Angle Reflection and Refraction (WARR). The advantage of this method is that it can estimate wave velocity to a linear reflector since increasing separation between antennae results in longer travel times. By comparing the change in antenna separation with the time taken for the reflected wave from reflectors, the velocity can be calculated.

However, since the separated antennas are not standard commercial equipments, the cost of this method is higher. In addition, the operation of this method is time consuming.

The third is called borehole method, in which the transmitting and receiving antenna are lowered into a pair of vertical access tubes. The arrival time of the electromagnetic wave between the boreholes and the known borehole distance is used to calculate the velocity and soil permittivity. According to antenna moving method, the borehole GPR can be divided into two categories. Zero offset gather (ZOG) method ensures no vertical difference between each antenna. While multiple offset gather (MOG) requires that one antenna be fixed and the other moves, producing a more detailed image using multiple raypaths. The advantage of this method is that it can measure the water content at different depth. However, the method is destructive and time consuming because it needs to dig hole to install antennas.

The fourth is called off-ground method. The GPR antennas are operated at some distance above the ground by mounting them on a vehicle or a low- flying air platform. What this method measures actually is reflection coefficient of the air–soil interface. This method is straightforward. However, this method requires flat ground surface and constant distance between antennas and ground. Variation of antenna elevation during field operation will lead to significant errors.

### **Hydrologic applications of GPR**

GPR has been used primarily to locate engineering and environmental targets in the upper 10 m of the earth (Grasmueck, 1996; Poisson et al., 2009). Hydrological application of GPR relies on the contrasting dielectric permittivity of media. For the most of natural soil, water content is the main factor to affect GPR reflection because the dielectric constant of water is about 80 while that of dry soil is between 3 and 5. It is such big contrast between water and surrounding soils that make hydrologic applications possible. Recently hydrological application

of GPR has increased dramatically, including soil water content estimation, water table depth estimation and flow process monitoring.

When GPR is applied to estimate soil water content, three relationships between the volumetric soil water content and dielectric permittivity are commonly used.

1. the most often used relationship is derived by Topp et al. (1980) as:

$$\theta = -5.3 \times 10^{-2} + 2.92 \times 10^{-2} \varepsilon - 5.5 \times 10^{-4} \varepsilon^2 + 4.3 \times 10^{-6} \varepsilon^3 \quad 1)$$

where  $\theta$  is volumetric water content.

2. A more theoretical relationship is described by a mixing model (Roth et al., 1990) as:

$$\theta = \frac{\sqrt{\varepsilon_b}}{\sqrt{\varepsilon_w} - 1} - \frac{(1-n)\sqrt{\varepsilon_s} - n}{\sqrt{\varepsilon_w} - 1} \quad 2)$$

where  $n$  is soil porosity;  $\varepsilon_w$ ,  $\varepsilon_s$  and  $\varepsilon_a$  are the permittivity of water, soil particles and air, respectively;  $\varepsilon_b$  is bulk permittivity of soil-water-air system.

3. A simple relationship suggested by Herkelrath et al. (1991) is:

$$\theta = a \sqrt{\varepsilon} - b \quad 3)$$

where  $a$  and  $b$  are calibration parameters.

Huisman et al. (2003) presented a comprehensive review about estimation soil water content from GPR using five GPR surveying techniques: (1) single-offset reflection methods (2) ground wave measurements (3) multiple-offset reflection methods (4) borehole transmission measurements and (5) surface reflection methods. They concluded that there is still a large difference in acceptance between these methods for soil water content estimation. Lunta, et al., (2005) used GPR to detect reflection of subsurface layer with known depth and use this information to estimate soil water content. Their results indicate GPR estimated soil water content had an accuracy that was comparable with existing conventional methods such as neutron probe and TDR. However, Weihermüller et al. (2007) compare two GPR techniques (ground wave and off-ground) to map

spatial variation of soil water content at the field scale. The results indicated that ground wave method was not suitable for the site studied. The variations of soil moisture content estimated using off-ground GPR results was lower than that measured by capacitance sensor and TDR. Based on the results they suggested the needs for a wider range of approaches to noninvasively map soil water content variation at the field scale. Slater and Comas (2009) indicated that application GPR to estimation soil water content is likely limited to the field scale and GPR cannot compete with satellite active or passive microwave-based methods at the catchment scale. Wijewardana and Galagedara (2010) use the borehole GPR method (ZOP and MOG) to estimate the spatio-temporal variability of soil moisture content in agricultural fields. The results indicate that soil moisture content estimated by GPR is correlated well with that estimated by the gravimetrically measured.

Water table represents an interface across which a relatively sharp change in soil water content occurs. It is therefore to expect that in some geologic conditions (e.g., clean sand, gravel, or limestone), the level of the water table can be detected with GPR. Bevan et al. applied GPR to investigate the drawdown in pumping test conducted in a sand aquifer. The results indicated that transition zone drawdown estimated by GPR is similar with that measured by neutron. Doolittle et al. (2006) applied GPR to estimate water table depth in areas of coarse-textured soils. Results indicated that over a 2-year period, GPR surveys revealed systematic spatiotemporal variations in water-table depths and radar interpretations of water-table depths were reasonably accurate. However, Daniels et al. (2005) found that the water table depth was not always accurately estimated GPR. They describe results of a tank experiment clearly illustrating that the primary GPR reflection was not from the water table but from the top of the capillary fringe. Another sand tank experiment by Pyke et al. (2008) also supported this conclusion. By changing water table in a controlled experimental environment, they found the main reflector of GPR energy was

indicative of the capillary fringe and not the actual water table. Well readings and estimates of the mass balance of water input into the experiment also confirmed their interpretation.

With the sensitivity to changes in water content, GPR has great potential to monitor flow dynamic in subsurface. Most GPR studies on water movement have focused on vertical water flow because in a flat area vertical flow can create more dielectric contrast to the surrounding media than lateral flow and thus cause GPR amplitude to increase more significantly. Birken and Versteeg (2000) used 4D GPR data set (3D + time) to visualize a dense non-aqueous liquid migration in a 9 by 9 by 3 m sand tank. Trinks et al. (2001) used time-lapsed GPR to study water infiltration in a sand tank and by comparing radargrams before and after infiltration they showed increased reflection below infiltration intake area due to vertical water migration. Freeland and Odhiambo (2006) used reflection patterns from GPR data to identify vertical preferential flow between loess-covered layer and clay layer in a cropland. In their study, some sections of GPR data showed columnar patterns around alluvium sand interface, which was associated with vertical preferential flow path. Truss et al. (2007) used densely sampled and precisely repeated GPR surveys to track vertical water movement in a karstic dissolution hole. Their results showed the process of how ponded water moved downward along the boundary of sand-filled dissolution hole. Saintenoy et al. (2008) also used time-lapsed GPR to monitor water infiltration through a borehole and used the simulated GPR data to explain reflections caused by the wetting front and the formation of saturation zone. Studies on hillslope lateral flow using GPR have been limited. For example Ronald et al. (2001) found a restricting soil layers with distinctly different dielectric properties, which impede vertical flow of water and have a significant influence on the lateral flow in the vadose zone. Holden et al. (2004) used GPR in conjunction with tracer to detect soil pipes (with diameter from 15 to 28 cm) and showed that the method could help establish hydrological connectivity of soil pipes within a complex subsurface drainage network.

## **Thesis Organization**

In the second chapter, hydrologic and geophysical data collected in the past few years in the Shale Hills catchment are summarized. Based on these data collected, two database systems are developed to provide effective management of soil moisture time series data and GPR image data, respectively. The detailed designs of the databases including graphical user interfaces (GUI) and data structures are described. Then the major functions of the two databases are illustrated.

In the third chapter, real-time soil moisture monitoring at different depths and locations along a concave hillslope is utilized to investigate the occurrence and frequency of subsurface lateral flow. The active layers that favor the subsurface lateral flow are identified by comparing the storage increase in each soil horizon with the rainfall inputs. By linking these active layers along the hillslope, potential preferential flow paths are delineated. Rainfall threshold and hydrological connectivity from the hilltop to the valley floor are then investigated.

In the fourth chapter, time-lapse GPR radargrams of artificial infiltration in two contrasting soils and hillslopes are compared to reveal the subsurface flow pattern. Real-time soil moisture monitoring data are used to analyze the flow processes and explain the observed radargrams. Based on the radargrams and soil moisture dynamics, four conceptual flow models are compared and examined using GPR simulations. Simulated radargrams are then compared to the field radargrams to identify the most likely flow process involved in each of the two soils.

In the fifth chapter, a water restricting layer and a soil-bedrock interface are identified in two contrasting soils, and seasonal GPR surveys are conducted to investigate the reflection change of these features. Seasonal changes of soil moisture are then used to explain seasonal GPR signal change. The GPR signal change reflects different flow processes in contrasting soils and suggests an optimal time for using GPR to detect soil layers.

In the sixth chapter, a MATLAB-based software package is developed for processing, displaying, and interpreting GPR data. The software program and related data structure are illustrated first. Major functions of the software are then demonstrated. A set of examples is used to compare this software with commercially available software to demonstrate its capability.

The final chapter provides the overall conclusions of this research, along with some speculated directions for future additional research.

## References

- Bevan, M.J., Endres, A.L., Rudolph, D.L., and Parkin, G. 2003. The non invasive characterization of pumping induced dewatering using ground penetrating radar. *Journal of Hydrology*, 281: 55–69.
- Birken, R., Versteeg, R., 2000. Use of four-dimensional ground penetrating radar and advanced visualization methods to determine subsurface fluid migration. *Journal of Applied Geophysics* 43, 215–226.
- Bonell, M., 1998. Selected challenges in outflow generation research in forests from the hillslope to headwater drainage basin scale, *J. Am. Water Resour. Assoc.* 34(4), 765–785.
- Brown, V.A., McDonnell, J.J., Burns, D.A., Kendall, C., 1999. The role of event water, a rapid shallow flow component, and catchment size in summer stormflow. *Journal of Hydrology*. 217(3–4): 171–190.
- Buttle, J.M., and McDonald, J.J., 2002. Coupled vertical and lateral preferential flow on a forested slope. *Water Resour. Res.* 38: 1060, doi:10.1029/2001WR000773.
- Daniels, J. J., R. Roberts, Vendl, M., 1995. Ground penetrating radar for the detection of liquid contaminants. *Journal of Applied Geophysics* 33, 195-207.

- Daniels, J.J., Allred, B., Binley, A., Labrecque, D., and Alumbaugh, D., 2005, Hydrogeophysical case studies in the vadose zone: in *Hydrogeophysics*, Rubin, Y., and Hubbard, S.S. (eds.), Water Science and Technology Library, 14, 413–438.
- Doolittle, J.A., Jenkinson, B., Hopkins, D., Ulmer, M. and Tuttle, W., 2006. Hydrogeological investigations with ground-penetrating radar (GPR): Estimating water-table depths and local ground-water flow pattern in areas of coarse-textured soils. *Geoderma*, 131: 317–329.
- Engler A. 1919. Untersuchungen über den Einfluss des Waldes auf den Stand der Gewässer. *Mitteilungen der Schweizerischen Zentralanstalt für das forstliche Versuchswesen* 12: 1–626.
- Freeland, R. S., Odhiambo, L O., 2006. Subsurface characterization using textural features extracted from GPR data. *Transactions of American Society of Agricultural and Biological Engineers*. 50, 287–293.
- Freer, J., McDonnell, J. J., Beven, K. J., 2002. The role of bedrock topography on subsurface storm flow. *Water Resources Research*. 38(12), WR000872.
- Freeze, R. A., 1972. Role of subsurface flow in generating surface runoff 2. Upstream source areas, *Water Resour. Res.* 8(5): 1272–1283.
- Grasmueck, M., R. W., and Horstmeyer, H., 1996. 3-D ground-penetrating radar applied to fracture imaging in gneiss. *Geophysics* 61(4), 1050-1064.
- Gish, T. J., Dualaney, W. P., Kung, K.J. S., Daughtry C. S. T., Doolittle J. A., and Miller P. T., 2002. Evaluating use of ground-penetrating radar for identifying subsurface flow. *Soil Sci. Soc. Am. J.* 66, 1620-1629.
- Grayson, R.B., Western, A.W, Chiew, F.H.S., Blöschl, G., 1997. Preferred states in spatial soil moisture patterns: local and nonlocal controls. *Water Resources Research* 33: 2897–2908.
- Haga, H., Matsumoto, Y., Matsutani, J., Fujita, M., Nishida, K. and Sakamoto, Y 2005. Flow paths, rainfall properties, and antecedent soil moisture controlling lags to peak discharge in a granitic unchanneled catchment. *Water Resour. Res.*, 41: W12410.

- Herkelrath, W.N., Hamburg, S.P. and Murphy, F., 1991. Automatic real-time monitoring of soil moisture in a remote field area with time domain reflectometry. *Water Resour. Res.* 27:857–864.
- Holden, J. 2004. Hydrological connectivity of soil pipes determined by ground-penetrating radar tracer detection. *Earth Surf. Process. Landforms* 29: 437–442.
- Huisman, J. A., Hubbard, S. S., J. D. Redman, and A. P. Annan., 2003. Measuring Soil Water Content with Ground Penetrating Radar: A Review. *Vadose Zone Journal* 2, 476–491.
- Hirsch, C.R. and Brater, E.F., 1941. Separating storm-hydrographs from small drainage-areas into surface- and subsurface-flow. *Transactions American Geophysical Union Part 3.* 22: 863–871.
- Jones, J.A.A, Connelly, L.J., 2002. A semi-distributed simulation model for natural pipeflow. *Journal of Hydrology.* 262: 28–49.
- Kienzler, P. M., and Naef, F., 2008. Subsurface storm flow formation at different hillslopes and implications for the ‘old water paradox’. *Hydrol. Process.* 22: 104–116.
- Kitahara, H., Terajima T, Nakai Y., 1994. Ratio of pipe flow to throughflow discharge. *Journal of the Japanese Forestry Society.* 71: 317–322.
- Lunt, I. A., Hubbard, S. S., Rubin, Y., 2005. Soil moisture content estimation using ground-penetrating radar reflection data. *Journal of Hydrology.* 307: 254-269.
- Lehmann, P., C. Hinz, G. McGrath, H. J. Tromp-van Meerveld, and J. J. McDonnell. 2006. Rainfall threshold for hillslope outflow: an emergent property of flow pathway connectivity, *Hydrol. Earth Syst. Sci. Discuss.*, 3, 2923–2961.
- Lin, H.S., W. Kogelmann, C. Walker, and M.A. Bruns., 2006. Soil moisture patterns in a forested catchment: A hydrogeological perspective. *Geoderma* 131:345-368.
- McDonnell, J.J., 1990. A rationale for old water discharge through macropores in a steep, humid catchment. *Water Resources Research* 26 (11), 2821–2832.

- McGlynn, B.L., McDonnell, J.J., Brammer, D.D., 2002. A review of the evolving perceptual model of hillslope flowpaths at the Maimai catchments, New Zealand. *Journal of Hydrology* 257, 1–26.
- McNamara, J. P., D. C., Mark Seyfried and Shiva Achet., 2005. Soil moisture states, lateral flow, and streamflow generation in a semi-arid, snowmelt-driven catchment. *Hydrological Processes* 19: 4023–4038.
- Negishi, J. N., S. Noguchi, Sidle, R. C., Ziegler, A. D., 2007. Stormflow generation involving pipe flow in a zero-order basin of Peninsular Malaysia. *Hydrological Processes* 21: 789–806.
- Newman, B.D., Campbell, A.R., Wilcox, B.P., 1998. Lateral subsurface flow pathways in a semiarid ponderosa pine hillslope. *Water Resources Research* 34: 3485–3496.
- Noguchi S, Tsuboyama, Y, Sidle R.C., Hosoda, I., 1999. Morphological characteristics of macropores and the distribution of preferential flow pathways in a forested slope segment. *Soil Sci. Soc. Am. J.* 63: 1413–1423.
- Poisson, J. Chouteau, M., Aubertin, M., Campos, D., 2009. Geophysical experiments to image the shallow internal structure and the moisture distribution of a mine waste rock pile. *Journal of Applied Geophysics* 67, 179–192.
- Pyke, K., Eyuboglu, S., Daniels, J.J. and Vendl, M., 2008. A controlled experiment to determine the water table response using ground penetrating radar. *Journal of Environmental and Engineering Geophysics* 13, Issue 4, pp. 335–342
- Ronald, E. Y., Freeland, R.S., Ammons, J.T. and Leonard, L. L., 2001. Mapping agricultural fields with GPR and EMI to identify offsite movement of agrochemicals. *Journal of Applied Geophysics* 47: 251-259.
- Slater, L and Comas, X., 2009. The contribution of Ground penetrating radar to water resource research: in *Ground penetrating radar theory and applications* Harry M.J (Eds.), Elsevier Science, 224-246.

- Saintenoy, A., Schneider, S., Tuchoka, P., 2008. Evaluating ground penetrating radar use for water infiltration monitoring. *Vadose Zone Journal*. 7: 208-214.
- Todd, M.S., Jeff, P.R., George M.H., 2000. Shallow subsurface storm flow in a forested headwater catchment: Observations and modeling using a modified Topmodel. *Water Resources Research* 36(9), 2575–2586.
- Topp, G. C., Davis, J. L., and Annan, A. P., 1980. Electromagnetic determination of soil water content: measurements in coaxial transmission lines. *Water Resour. Res.*16:574-582
- Trinks, I., Wachsmuth, D., H. Stümpel., 2001. Monitoring water flow in the unsaturated zone using georadar. *First Break* 19, 679-684.
- Truss S., Grasmueck M., Vega S., and Viggiano D. A., 2007. Imaging rainfall drainage within the Miami oolitic limestone using high-resolution time-lapse ground-penetrating radar. *Water Resources Research* 43, doi:10.1029/2005WR004395.
- Tromp-van Meerveld, I. and McDonnell, J.J., 2006a. Threshold relations in subsurface stormflow 1: A 147 storm analysis of the Panola hillslope trench. *Water Resources Research*. doi:10.1029/2004WR003778.
- Tromp-van Meerveld, H.J. and McDonnell, J.J., 2006b. Threshold relations in subsurface stormflow 2: The fill and spill hypothesis: an explanation for observed threshold behavior in subsurface stormflow. *Water Resources Research*, doi:10.1029/2004WR003800.
- Weihermüller, L., Huisman, J.A. Lambot, S., Herbst, M., Vereecken, H., 2007. Mapping the spatial variation of soil water content at the field scale with different ground penetrating radar techniques. *Journal of Hydrology*. 340:205-216.
- Weiler, M, and McDonnell, J.J., 2004. Virtual experiments: a new approach for improving process conceptualization in hillslope hydrology. *Journal of Hydrology* 285: 3–18.

- Weiler, M, McDonnell, J.J., Tromp-van Meerveld I, Uchida, T., 2006. Subsurface stormflow. In Encyclopedia of Hydrological Sciences, Volume 3, Part 10, Anderson MG, McDonnell JJ (eds). Wiley.
- Sidle, R., Noguchi, S., Tsuboyama, Y., Laursen, K., 2001. A conceptual model of preferential flow systems in forested hillslopes: evidence of self-organization. *Hydrological Processes* 15: 1675–1692.
- Stieglitz, M., Shaman, J., McNamara, J., Engel, V., Shanley, J., Kling, G.W., 2003. An approach to understanding hydrologic connectivity on the hillslope and the implications for nutrient transport. *Global Biogeochem. Cycles* 17 (4), 1105. doi:10.1029/2003GB00204.
- Weyman, D. R., 1973. Measurements of the downslope flow of water in a soil, *Journal of Hydrology*. 20: 267–288.
- Whipkey, R. Z. 1965. Subsurface stormflow from forested slopes, *Bull. Int. Assoc. Sci. Hydrol.* 10:74–85.
- Wijewardana, Y.G.N.S., and Galagedara, L.W., 2010. Estimation of spatio-temporal variability of soil water content in agricultural fields with ground penetrating radar. *Journal of Hydrology*, 391:24-33.

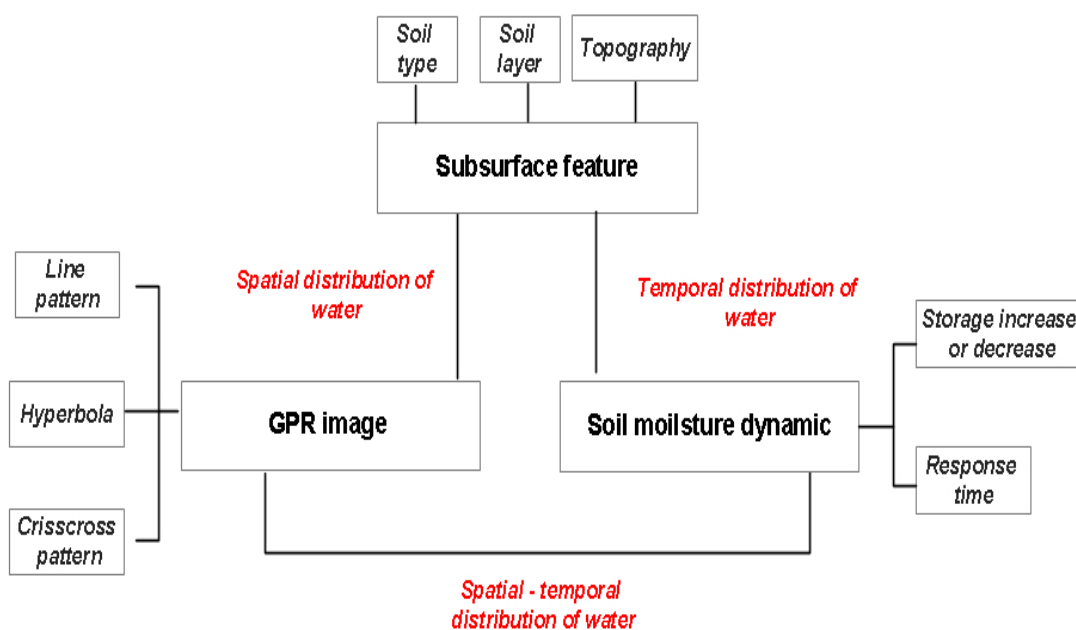


Figure 1-1: A general framework for the integrated study employed in this study. GPR image patterns such as line pattern, hyperbola shape and crisscross pattern reflect subsurface feature (soil type, soil layer, topography and so on) and spatial distribution of water. Soil moisture dynamic such as storage increase or decrease and response time reflect temporal distribution of water. By coupling GPR image with soil moisture dynamics, the spatial-temporal pattern of water movement in the subsurface can be better identified and explained.

## Chapter 2

### Hydrological and Geophysical Databases for the Shale Hills Catchment

#### Introduction

Understanding subsurface structure and its impacts on the occurrence and intensity of subsurface flow is becoming critical to reveal subsurface flow processes, identify subsurface flow direction and quantify contribution of subsurface runoff to stream flow. However, due to the complex subsurface heterogeneity, the spatial and temporal occurrence of subsurface flow is not yet well understood. Therefore, more extensive and intensive data about the subsurface and flow dynamics are required to better understand these fundamental processes. In essence, the more information that is gathered, the better the conclusions that can be synthesized, and a greater understanding of natural processes can be achieved. In this chapter, the hydrological data and geophysical data collected in the Shale Hills Catchment in the past few years will be introduced. Later chapters will apply the subset of these dataset to identify subsurface flow.

Since 2004, intensive hydrological monitoring has been established at different location to understand the occurrence and intensity of subsurface flow at the Shale Hills catchment. According to collection methods, these monitoring data can be grouped into two categories.

1. Manually collected data on an approximately weekly basis. These data include multi-depth soil moisture measured by Time Domain Reflectometry (TDR), multi-depth soil matric potential data measured by tensiometer and shallow water table data.

2. Automatically collected data on 10-minute interval. These data include:

- 1) Multi-depth soil moisture measured by the capacitance-type ECH2O probes

(Decagon Devices, Inc., Pullman, WA)

2) multi-depth soil matric potential measured by several different sensors including the 229 heat dissipation water matric potential sensors (Campbell Scientific Inc., Logan, UT), the specially-made Decagon matric probes (Decagon Devices, Inc., Pullman, WA) and 253 watermark soil matric potential (Campbell Scientific Inc., Logan, UT)

3) Soil temperature data measured by the 229 heat dissipation water matric potential sensor.

4) Rainfall data measured by TE525-WS tipping bucket rain gauge (Texas Electronics, Inc., Dallas, TX)

5) Soil redox potential measured by customarily-made sensor

In addition, to understand complex subsurface heterogeneity and its impacts on subsurface flow, a series of geophysical surveys using GPR has been conducted since 2004. According to purpose of survey, these GPR surveys can be grouped into three categories.

1. Transect surveys, these are the one survey line along or cross the slope to investigate static properties such as depth to bedrock and existing of soil layers.

2. Grid surveys, these are the parallel survey lines in a rectangular area to investigate the effect of seasonal change on GPR signal.

3. Infiltration survey, these can be short transecting survey or grid survey but with artificial water applied to investigate subsurface water movement.

Based on the extensive monitoring data, temporal stability in the soil moisture spatial pattern has been found to be governed by soil series and landforms (Lin, 2006). Four main subsurface preferential flow pathways down the hillslope have been identified and conceptualized (Lin et al., 2006). Direct evidence of vertical and lateral subsurface flow has been revealed by real time soil moisture monitoring (Lin and Zhou, 2008; Zhang and Lin, 2011). The controls and frequency of vertical preferential flow occurrence in different soil series and landscape positions has been determined (Graham and Lin, 2011). Based on the GPR surveys, two subsurface flow

patterns have been identified on two contrast soils in hillslope after infiltration. That is subsurface lateral macropore flow was dominant in the shallow Weikert soil, while a combination of vertical macropore flow and lateral matrix flow was dominant in the deep Rushtown soil (Zhang et al, 2011). A water restricting layer and soil bedrock interface have been detected by GPR surveys on the two contrasting soils and through the seasonal GPR survey, the optimal time to detect these layers has also been proposed (Zhang et al, 2011).

The above findings demonstrated the benefits of long-term hydrological monitoring and invasive GPR survey. However, with increased data collection, vast amounts of data were acquired and these data were collected at different location, at different spatial and temporal resolutions, using different method and had different data type. How to manage these data from multiple sources and retrieve these data in single workspace is fundamental for hydrological analysis and is also important for the data sharing in the hydrological research group. The objectives of this chapter are to 1) present the detailed design of Shale Hills Time Series Database (SHTSD) for the Shale Hills including table structures and overall graphic user interface (GUI) and 2) present the detailed design of GPR Image System (GPRIS) for Shale Hills including functions and GUI.

## **Shale Hills Time Series Database (SHTSD)**

### **Background**

Typically, hydrologic data are stored in a spreadsheet. Although spreadsheet provides a straightforward organization of data, it only stores two dimensional data. When extracting information from high dimensional data, multiple separated files are needed and continuous copy and paste are required to obtain interested information. For example, if we want to know the average soil moisture at depth 40 cm for some of interested monitoring site during past five days,

then we need five spreadsheets that store soil moisture data at depth 40cm for all sites, after that we begin to pick up the sites that we are interested from the five spreadsheets and finally get the results. Therefore, spreadsheet is not an ideal storage tool for large datasets. After relational model was present by Codd (1970), relational database management system (RDBMS) became most popular due to its increased efficiency of data storage and retrieval. However, although RDBMS were widely used in the hydrological data management systems, the spatial distribution of monitoring items were not explicitly expressed.

Based on the hydrologic data collected during past few years, we developed Shale Hills Time Series Database (SHTSD) to handle the extensive hydrologic data management. With friendly GUI, complex data sets can be easily retrieved. In addition, using spatial data as interface assisted with results interpretation and information integration.

### **Function and GUI design**

SHTSD is developed in Visual Basic 6 with ESRI MapObjects being used to provide the links to the location of monitoring sites in the catchment and Microsoft Access 2003 as database manage platform. In addition, Sigmaplot is also used for display the exported data. At current stage, the time series database is not fully coupled with GIS. The GIS is used only as interface for convenient retrieval of data.

Based on the monitoring items and data collection method, the main interface contains four sub interfaces (gray box in Figure 2-1). Main interface provides the access to four data categories (Figure 2-2A). Interface of Query auto monitoring site provides query based on monitoring site (Figure 2-2B). This is because only seven auto sites exist and the monitoring depth and item of each site is quite different. Interface of Query manually collected TDR and Query manually collected Tension can provide query by either monitoring site or depth (Figure 2-2C and 2-2D). By site query it means that user can select any depth at one site for query and by

depth query it means that user can select any site at one depth for query. Although redox data are also automatically collected, they were collected since 2010 and the site locations are different from the previously established auto monitoring site. Therefore, they are separated as independent interface (Figure 2-2E). All interfaces have functions to query data by site, display monitoring location in the catchment, preview the query data, export query data to Excel for further analysis. For the automatically collected data the interface also has function to query data by the monitoring items and for manually collected data, the interface has function to query data by depth in which data are measure (orange box in Figure 2-1). For the automatically collected data including previously established auto site and newly established redox data, both interfaces have functions to export query data to SigmaPlot for graphical display and editing since the query contains large amount of data and Sigmaplot provide easy manipulation of plot.

### **Database Design and table structure**

Microsoft access 2003 is used as database management platform. Based on the four interface mentioned above, the data base is divided into four categories: automatically monitoring data, TDR data, Tension data and Redox data. Figure 2-3 outlines the database structure with table relationships.

Tables are grouped into two basic types: reference tables and data tables. Reference tables hold the reference information related to the data tables but these information are separated from data table and can referred by a unique ID number . Usually reference tables described static information and recorded only once. For example, *siteinfo* table describes related information about the monitoring site when the site has been established such as site name, soil series in the site; in automatically monitoring data, *depthinfo* table describes monitoring depth in the site and *monitoringitems* table describes the monitoring items such as soil moisture content and/or other properties at the certain depth of the site. By referred to a unique ID number, clear semantic

relationships among reference tables can be built such as “site with site name site74 recorded soil moisture content at depth 20cm”. In contrast, data tables are where the collected data are stored. For example, in the automatically monitoring data, table *Monitortime* stores monitoring time while table *MonitorData* stores monitoring data and they are linked through a unique ID *MonitoringID*. The monitoring time is separated from monitoring data because in the auto monitoring site, the same depth has multiple monitoring items at the same time. Using 1: ∞ relation in *MonitoringID* between table *Monitortime* and *MonitorData* (Figure 2-3B) can retrieve multiple data at same depth. At the same time, this will also provide flexibility when adding new monitoring item at the same depth. The new monitoring item is only a record (or row) in the table *MonitoringItems*, which can be referred by itemID and then be referred to in the table *MonitorData* without to alter the table structure. On the contrary, in manually collected TDR and Tension data and redox data, monitoring data and monitoring time are in the same table since only one item is monitored.

Data tables are related to reference tables through a unique ID. For example, in the automatically monitoring data, the *AutoDepthID* links table *AutoDepthInfo* and *MonitorTime*. *AutoDepthID* is unique in table *AutoDepthInfo* as indicated by “1” in the connection line while in table *MonitorTime* the same *AutoDepthID* repeats in multiple records as indicated by “∞” in the connection line. This allows the data table on the “∞” side of the relationship to store time series records at the same depth as indentified by *AutoDepthID* . If only one item is monitored at the same depth, then the monitoring time and monitoring data will be in the same table, which is the case in TDR data for example. If multiple items are monitored at the same depth, then the monitoring time and monitoring data are in separated tables and monitoring data table contains the ID number referred to the monitoring items table, which is case in automatically monitoring

data for example. This design eliminates redundant record in the reference table and enforces referential relationship between reference table and data table.

## **Shale Hills GPR Image System (GPRIS)**

### **Background**

Since 2004, GPR surveys have been conducted to investigate subsurface features and effect of water distribution on GPR signals. Large amount of data were collected, in which some of data showed promising results and some of data were still hard to explain and did not showed the results as we expected. This may be due to 1) physical and chemical properties of the material through which GPR pass since the electromagnetic wave is sensitive to surrounding media 2) inappropriate operation or data processing which cause information loss 3) lack of other information or knowledge to interpret radar image since GPR does not directly measure the property of interest. However, the data itself provide valuable information. GPR data acquisition and processing are expensive. Lack of a proper data management may lead to acquisition of redundant data and consequently waste time and money.

In this study we developed a tool to manage GPR image data. This tool will provide previous work that had been covered and make it a bottom line for the future work. The tool also provide location of potential target that needs further detailed work by examine the data.

### **Function and GUI design**

Shale Hills GPR image system was developed in Visual Basic 2008 with ESRI MapObjects being used to provide the links to the spatial GPR survey data. Data access is controlled through the spatial interface using shape files. Figure 2-4 outlines the interfaces and functions.

The main interface provide five functions to zoom in layers, return to original size of layers, pan the layers, open or close layers and query GPR survey according to three categories mentioned in the introduction (Figure 2-5A). SiteInfo interface is same for three GPR survey categories and provides three functions to get the basic information about survey such as when and how the GPR survey was conducted, get the layout of the survey(usually it is JPEG file that document the survey layout) and display the radargram (Figure 2-5B). However, the interface provided by radargram display is different for three GPR survey categories.

In the transect survey, only 2D view, zoom in/out and opening report are provided (Figure 2-6A). The report is a word or pdf file that gives more detail results of the survey. In the grid survey interface, 3D view of radargram is added (Figure 2-6B). In the infiltration survey, radar display includes time-lapse view of radargram and Sigmaplot view is provided if the infiltration survey was combined with real time soil moisture monitoring. Sigmaplot view will provide soil moisture dynamics before, during and after infiltration. In addition, some slides are also provided to animate the time- lapse GPR signal change (Figure 2-6C).

### **Data organization and structure**

The survey data are organized using hierarchical folders with data files in it and indexed text files. Figure 2-7 show data structure for storing 3 types of GPR survey. In the application program folder, there are two folders. One is map folder, which store the shape files of catchment and GPR survey data. Other is data folder, which store three types of the GPR survey data. For the grid survey, the folder is name as abbreviation G plus the site ID with underline delimiter. For the infiltration survey, the folder is name as abbreviation I plus the site ID with underline delimiter. For the transect survey, the folder is name as abbreviation T plus the site ID and the year the survey was conducted with underline delimiter.

Each type of GPR survey contains a text file named as BasicInfo.txt, a image file named as Layout.jpeg and several survey name folders with name format as m\_d\_yyyy, which is the date when the GPR surveys were conducted. The BasicInfo.txt file stores the date when GPR surveys were conducted and a brief description how the survey was conducted. Figure 2-8 show an example of BasicInfo.txt. Date was inserted between two marker '#EVENT#' and '#ENDEVENT#' and the description started just below the date and end with marker '#END#'. The markers always start with pound sign. The program will read the information and display to the user.

However, the content in the survey name folder with name format m\_d\_yyyy is different for different type of survey. For the grid survey and transect survey, only the radar folder and report folder are in the survey name folder. But for infiltration survey, survey name folder contains a folder named as ppt and a folder named as sigma and another text file named as infiltration.txt. Figure 2-9 show an example of infiltration.txt, which described the time information and infiltration information separated by several markers. Note ordinal number between '#time lapse#' and '#End time lapse#' indicate sequence GPR survey was conducted and comments after colon indicate exact time after infiltration. This ordinal number will be used to index the image file in radar folder.

## References

- Graham, C.B., and H.S. Lin. 2011. Controls and frequency of preferential flow occurrence: A 175-event analysis. *Vadose Zone Journal* 10:816–831
- Lin, H.S. 2006. Temporal stability of soil moisture spatial pattern and subsurface preferential flow pathways in the Shale Hills Catchment. *Vadose Zone Journal* 5:317-340.

- Lin, H.S., W. Kogelmann, C. Walker, and M.A. Bruns. 2006b. Soil moisture patterns in a forested catchment: A hydrogeological perspective. *Geoderma* 131:345-368.
- Lin, H. and Zhou X. 2008. Evidence of subsurface preferential flow using soil hydrologic monitoring in the Shale Hills catchment. *European J. Soil Sci.* 59, 34-49.
- Zhang, J. H.S. Lin, and J. Doolittle. 2010. Subsurface Lateral Flow as Revealed by Combined Ground Penetrating Radar and Real-Time Soil Moisture Monitoring. *Hydrological Processes* (in revision).
- Zhang, J. H.S. Lin, and J. Doolittle. 2011. Seasonal GPR signal changes in two soil and hillslopes. *Geoderma* (in review).
- Zhang, J. H.S. Lin. 2011. Subsurface lateral flow in the shale hills catchment as revealed by real-time soil moisture monitoring. *Journal of hydrology*. (in review)

Table 2- 1 List of field name and descriptions relations for Shale Hills Time Series Database

Field name	Data Type	Description
<i>Table SiteInfo</i>		
SiteID(PK)	Auto Increment Number	Unique number to identify monitoring site
SiteName	text	Description name for monitoring site
SiteType	text	Description of site category only four type Auto, TDR, Tesion, Redox
Soil Taxonomy	text	Description of soil series name in the site
Landscape	text	Description of position in catchment such as rigdge, valley
<i>Table AutoDeptInfo</i>		
AutoDepthID(PK)	Auto Increment Number	Unique number to identify depth
SiteID(FK)	number (long)	Number to indentify the site to which the depth belongs
Depth	number (float)	Number to describe monitoring depth
DepthUnit	text	Unit to describe monitoring depth
<i>Table MonitoringTime</i>		
MornitorID(PK)	Auto Increment Number	Unique number to indentify time series records
AutoDepthID(FK)	number (long)	Number to indentify the depth which time series monitoring are taken
RecordDate	date	Date that autodata are measured
RecordTime	time	Time that autodata are measured
<i>Table MonitorData</i>		
DataID(PK)	Auto Increment Number	Unique number to indentify Data value records
MornitorID(FK)	number(long)	Number to indentify time series records
ItemID(FK)	number(long)	Number to indentify monitoring item
Data Value	number(float)	Data value for the monitoring items

Table 2-1 (continued)

Field name	Data Type	Description
<i>Table MonitorItem</i>		
<b>ItemID(PK)</b>	Auto Increment Number	Unique number to indentify monitoring items
ItemName	text	Brief Name for monitoring items such as SMC, SWP
ItemDescription	text	Description of monitoring items e.g. SMC is soil moisture content
ItemUnit	text	Unit to describe monitoring item
<i>Table TDRDeptInfo</i>		
<b>TDRDepthID(PK)</b>	Auto Increment Number	Unique number to identify depth that TDR is measured
SiteID(FK)	number (long)	Number to indentify the TDR site to which the depth belongs
Depth	number (float)	Number to describe TDR measured depth
DepthUnit	text	Unit to t TDR measured depth
<i>Table TDRData</i>		
<b>TDRID(PK)</b>	Auto Increment Number	Unique number to indentify TDR Data value records
TDRDepthID(FK)	number (long)	Number to indentify the depth which TDR data is measured
RecordDate	date	Date that TDR are measured
TDRData	number (float)	Data value for TDR measurement
<i>Table TensionDeptInfo</i>		
<b>TensionDepthID(PK)</b>	Auto Increment Number	Unique number to identify depth that Tension is measured
SiteID(FK)	number (long)	Number to indentify the Tension site to which the depth belongs
Depth	number (float)	Number to describe Tension measured depth
DepthUnit	text	Unit to Tension measured depth
<i>Table TensionData</i>		
<b>TensionID(PK)</b>	Auto Increment Number	Unique number to indentify Tension Data value records

Table 2-1 (continued)

Field name	Data Type	Description
TensionDepthID(FK)	number (long)	Number to indentify the depth which Tension data is measured
RecordDate	date	Date that Tension are measured
TensionData	number (float)	Data value for Tension measurement
<i>Table RedoxDeptInfo</i>		
<b>RedoxDepthID(PK)</b>	Auto Increment Number	Unique number to identify depth that Redox is measured
SiteID(FK)	number (long)	Number to indentify the Redox site to which the depth belongs
Depth	number (float)	Number to describe Redox measured depth
DepthUnit	text	Unit to Redox measured depth
<i>Table RedoxData</i>		
<b>RedoxID(PK)</b>	Auto Increment Number	Unique number to indentify Redox Data value records
RedoxDepthID(FK)	number (long)	Number to indentify the depth which Redox data is measured
RecordDate	date	Date that Redox are measured
RecordTime	time	Time that Redox are measured
RawRedoxData	time	Data value for Redox measurement
<i>Table RedoxCorrection</i>		
<b>CorrectionID(PK)</b>	Auto Increment Number	Unique number to indentify CorrectionFactor
RedoxDepthID(FK)	number (long)	Number to indentify the depth which Redox data is measured
CorrectionFactor	number (float)	Number to correct Redox raw data

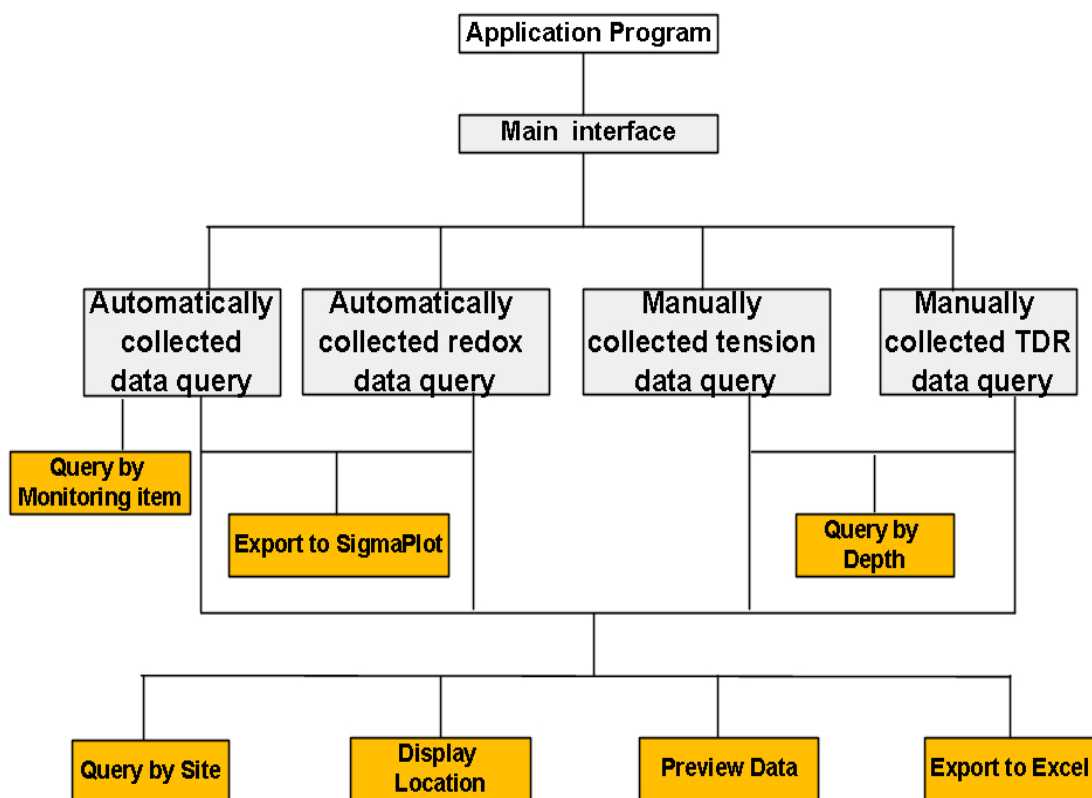
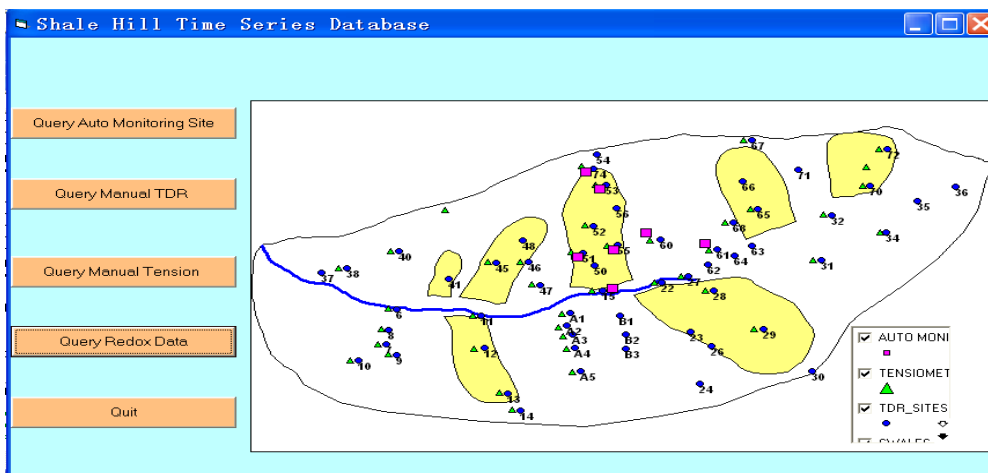
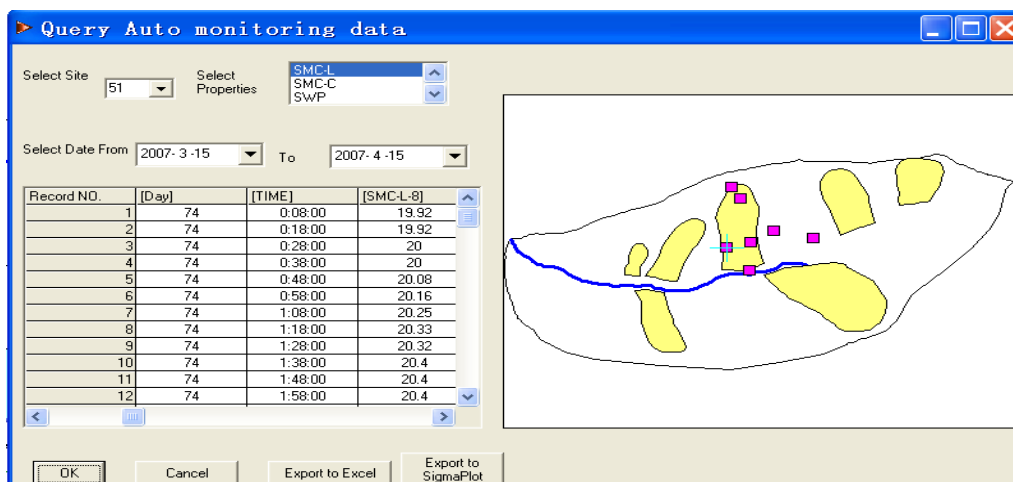


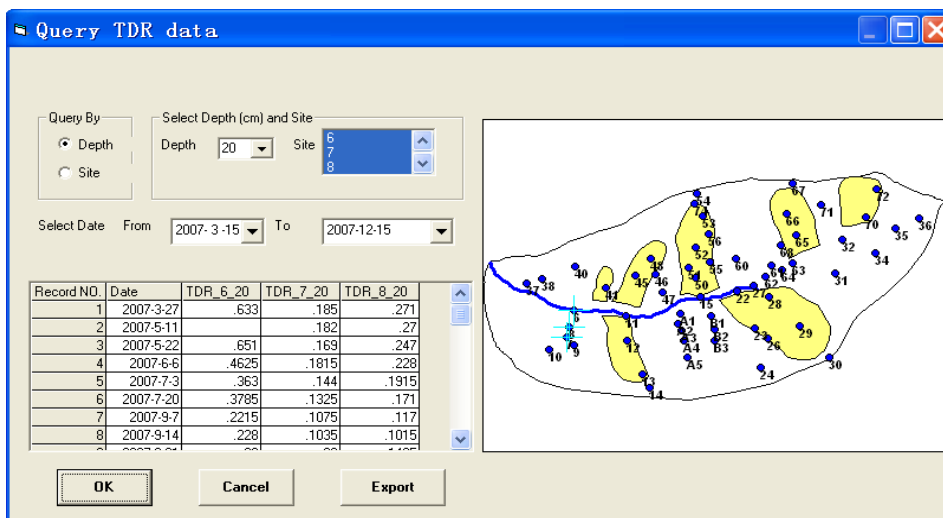
Figure 2- 1: Outline of SHTSD application program interfaces (gray box) and functions (orange box)



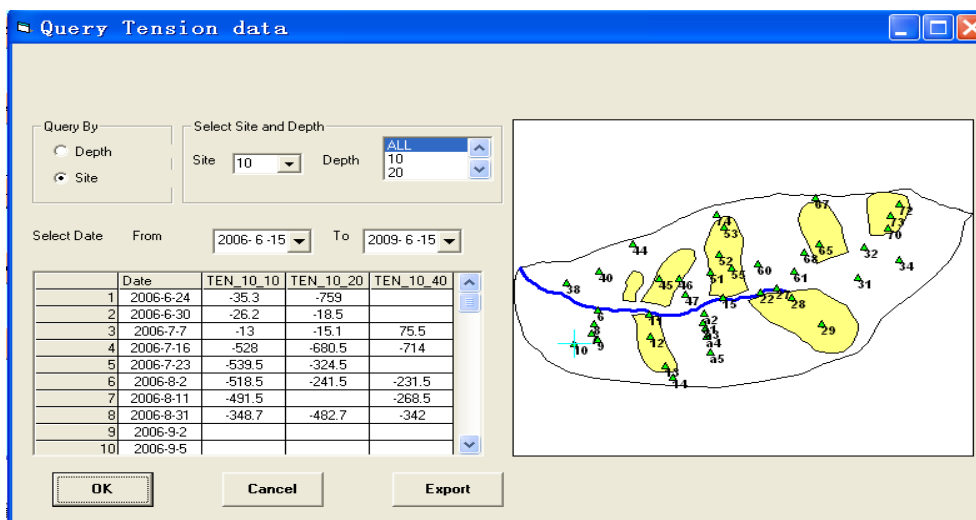
A



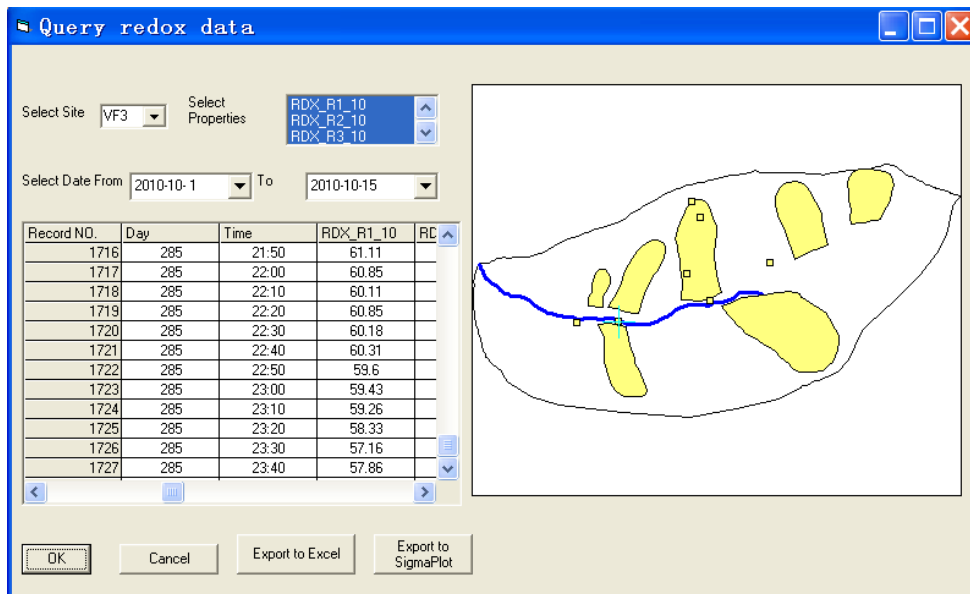
B



C

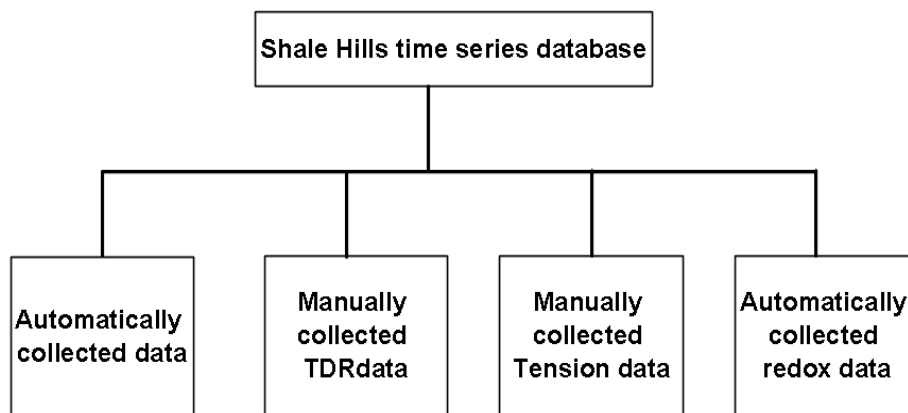


D

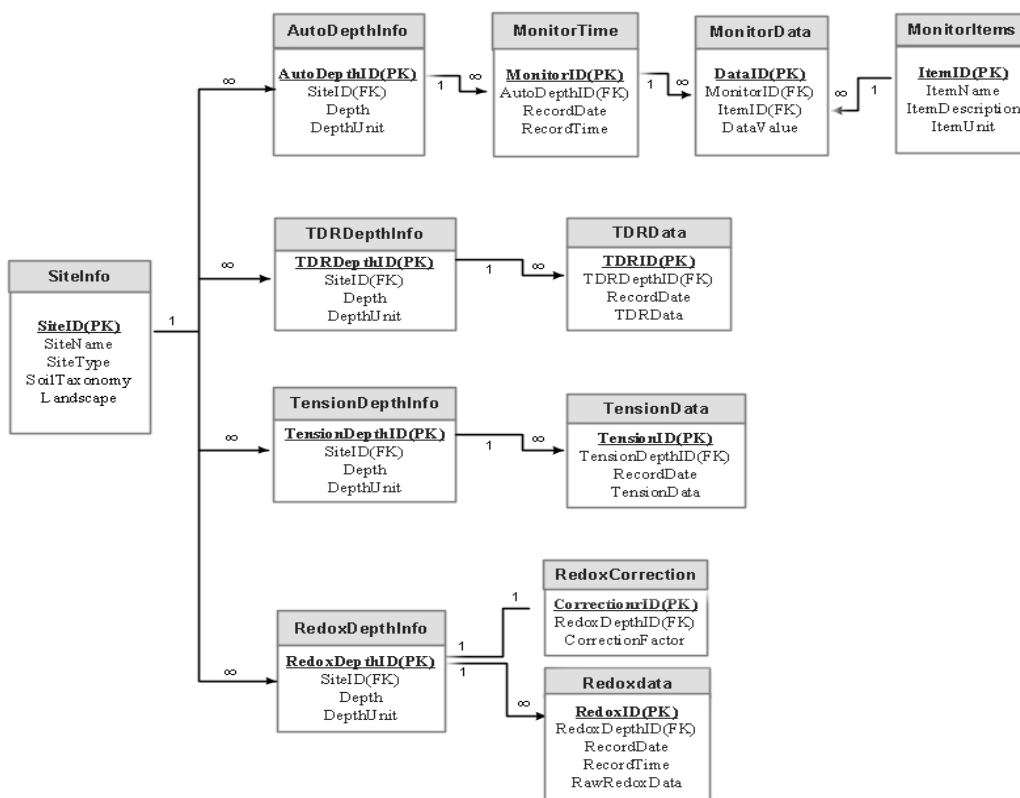


E

Figure 2- 2: Demonstration of interfaces for SHTSD application program. The cyan crosshair indicates the location of selected sites A. Main interface; B. Interface of Query auto monitoring site; C. Interface of Query manually collected TDR; D. Interface Query manually collected Tension; E. Interface of Query redox data



A



B

Figure 2-3: A. Outline of Shale Hills time series database structure. B. Table relationships.

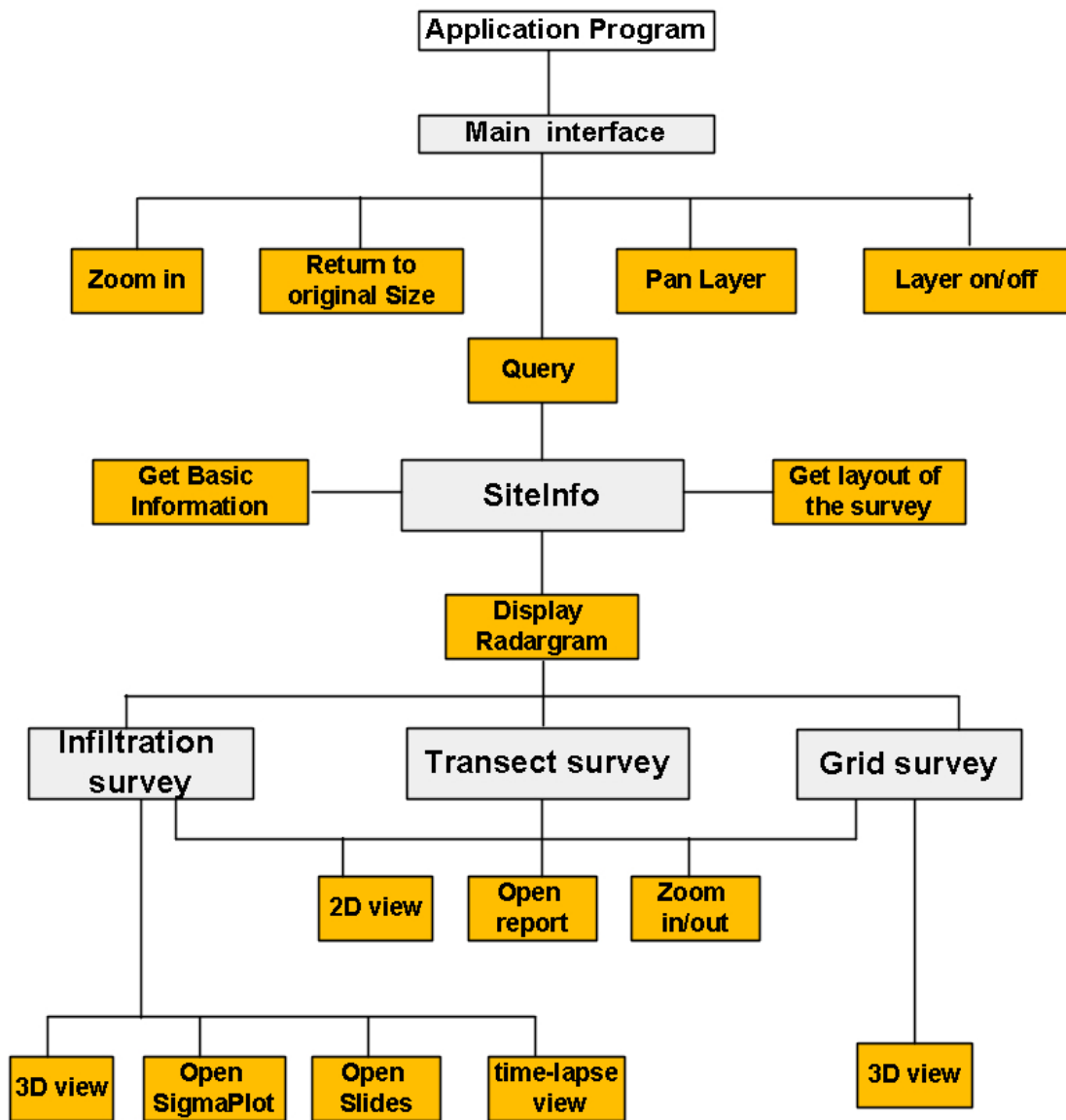
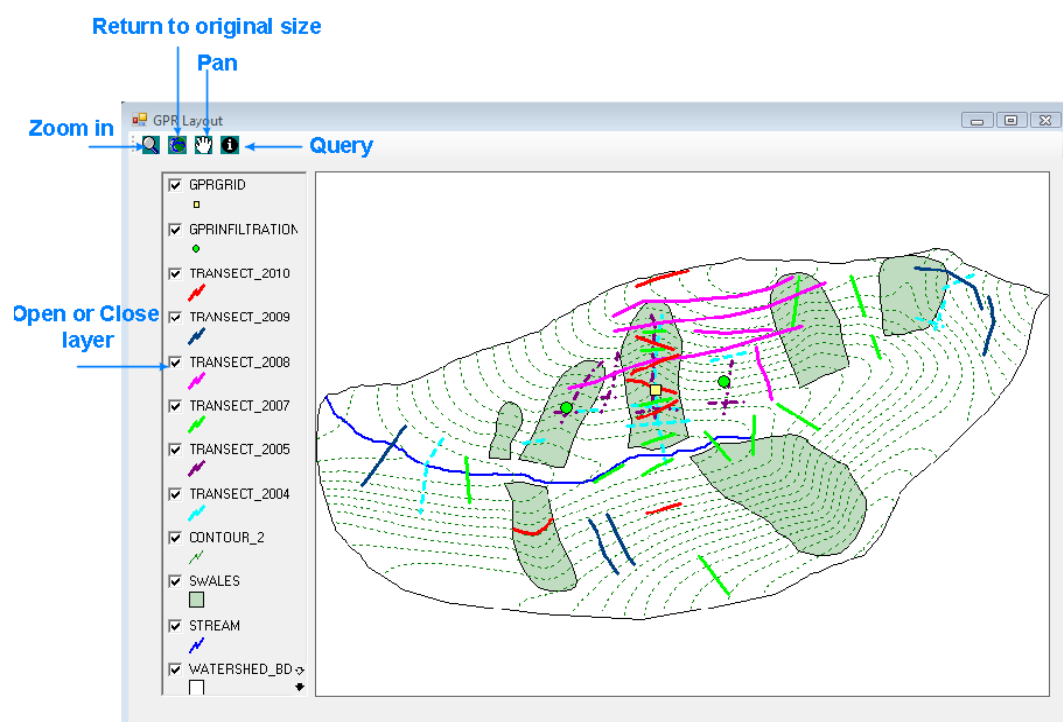
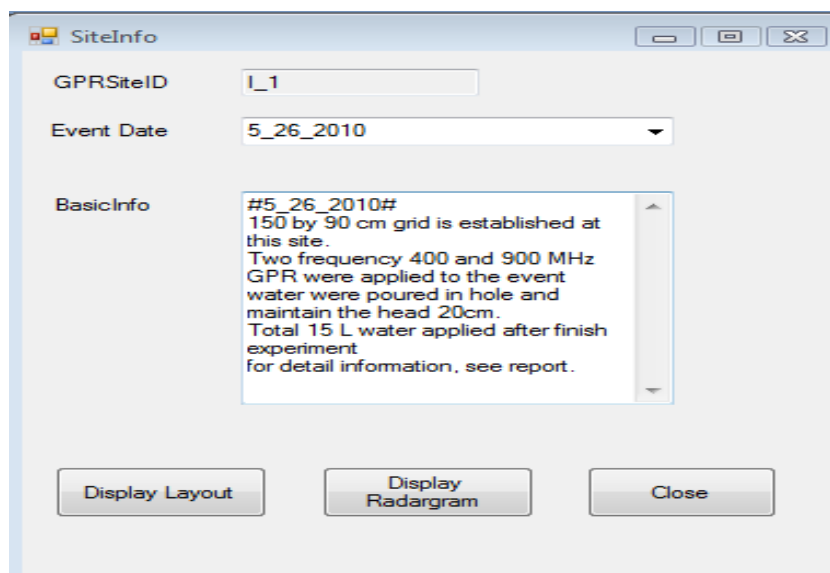


Figure 2-4: Outlines of interfaces (gray box) and functions (orange box) in GPRimagesys

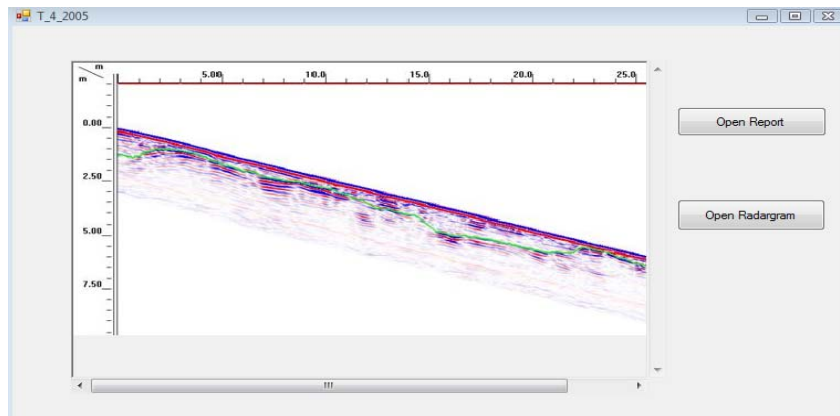


A

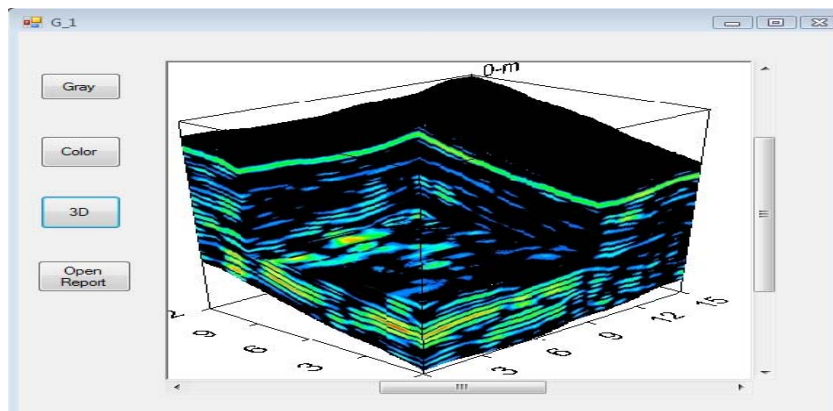


B)

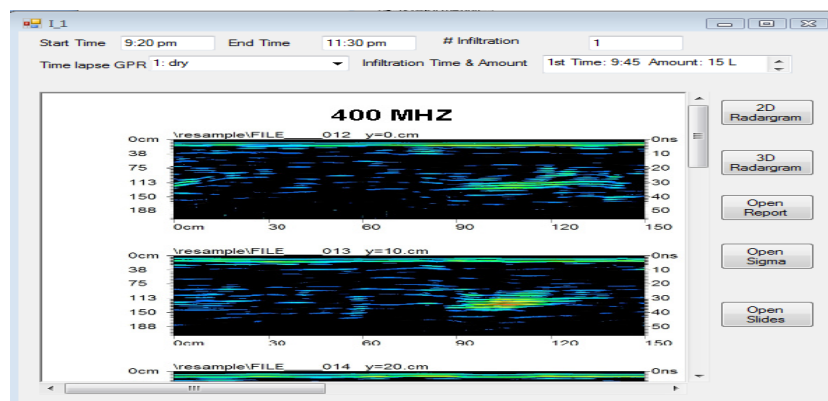
Figure 2-5: A. Main interface with five functions labeled; B. Site info interface with three functions to 1) get the basic information, 2) get the layout of the survey, and 3) display the radargram.



A



B



C

Figure 2-6 : A. Radargram display in transect survey;  
 B. Radargram display in grid survey;  
 C. Radargram display in infiltration survey

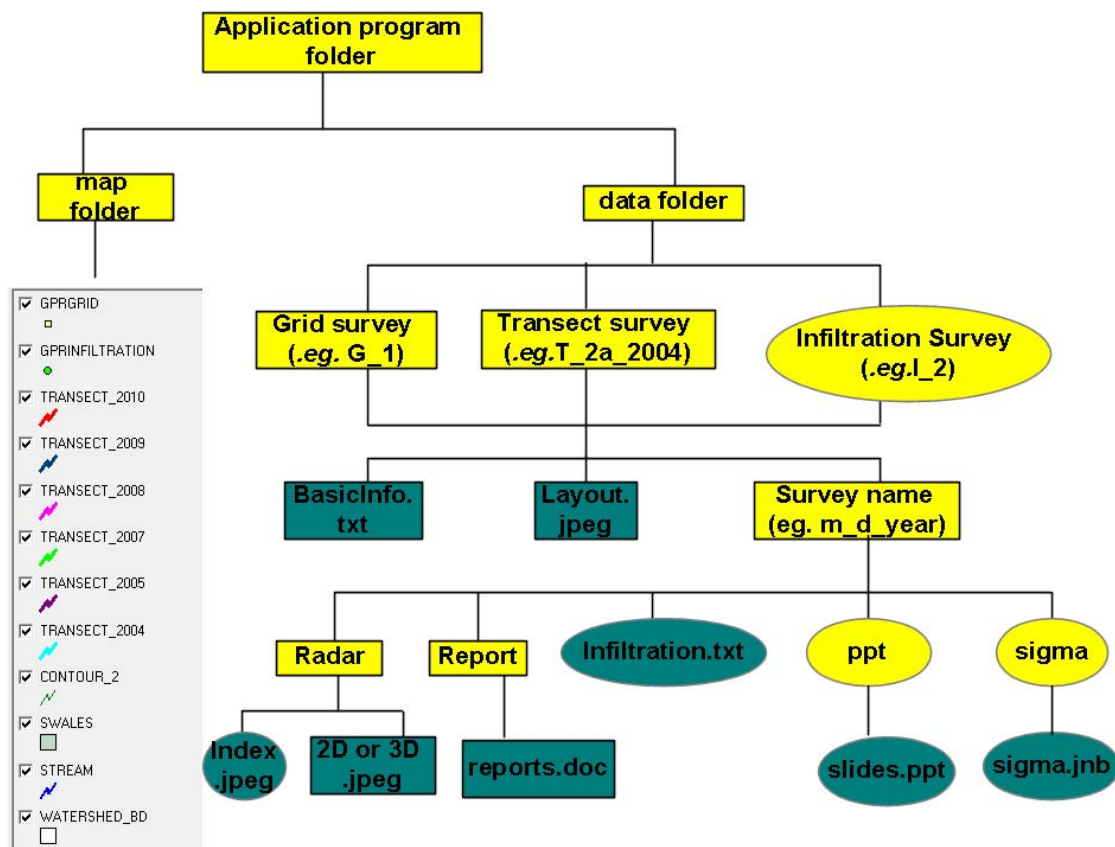


Figure 2-7 : Data structure in GPRimagesys. At the left legend under map folder, Yellow square shape file indicate location of grid survey, Green dot shape file indicate location of infiltration survey and line shape file with name starting as transect indicate transect survey line. At the right under data folder, yellow color indicates the folder and dark green color indicate file (such as word file, text file and image file). Ellipse shape indicates folders and files only in the infiltration survey and rectangular shape indicates files and folders in the three type of survey (Grid survey, transect survey and infiltration survey). See details in the text.

```

1 #EVENT# → Marker to start input date
2 4_30_2008
3 11_19_2009
4 5_26_2010
5 #ENDEVENT# → Marker to end input date
6
7 #4_30_2008# → Marker to describe how survey was conducted
8 A 3 m transect was established right above an existed soil pit.
9 9 ECH20-TE probes were installed at different depth of the soil pit
10 20 liter water was slowly poured at infiltration point and pouring process lasted 2 minutes.
11 for detail information,see report.
12 #11_19_2009#
13 A 150 by 90 cm grid is established along the slope near site 45 at shale hill catchment.
14 A hole with diameter 8cm and depth 20cm existed at right side of the grid.
15 Water was injected in the hole and the constant head 20cm was maintained during the experiment.
16 #5_26_2010#
17 150 by 90 cm grid is established at this site.
18 Two frequency 400 and 900 MHz GPR were applied to the event
19 water were poured in hole and maintain the head 20cm.
20 Total 15 L water applied after finish experiment
21 for detail information, see report.
22 #END# → Marker to end description

```

Figure 2-8: Illustration of BasicInfo.txt, which stores information about when, where and how GPR surveys were conducted. Markers start with pound sign and description will be inserted between markers

```

1 #start time#
2 11:00am
3 #End start time#
4
5 #end time#
6 17:00 pm
7 #End end time#
8
9 #infiltration#
10 3
11 #End infiltration#
12
13 #infiltration time#
14 Time: 11:20 am Amount: 17 L
15 Time: 12:00 pm Amount: 17 L
16 Time: 14:22 pm Amount: 17 L
17 #End infiltration time#
18
19 #time lapse#
20 1: dry
21 2: 0 min after 1st infiltration
22 3: 10 min after 1st infiltration
23 4: 20 min after 1st infiltration
24 5: 30 min after 1st infiltration
25 6: 0 min after 2nd infiltration
26 7: 10 min after 2nd infiltration
27 8: 20 min after 2nd infiltration
28 9: 30 min after 2nd infiltration
29 10: 70 min after 2nd infiltration
30 11: 10 min after 3rd infiltration
31 12: 20 min after 3rd infiltration
32 13: 130 min after 3rd infiltration
33 14: Time lapse of 70cm line
34 15: Time lapse of 60cm line
35 16: Difference with dry (70cm line)
36 17: Difference with dry (60cm line)
37 #End time lapse#

```

Figure 2-9 : Illustration of Infiltration.txt, which stores time information and infiltration information about GPR surveys. Markers start with pound sign and description will be inserted between markers. Note ordinal number between ' #time lapse#' and '#End time lapse#' indicate sequence GPR survey was conducted and comments after colon indicate exact time after infiltration. This ordinal number will be used to index the image file in radar folder

## Chapter3

### **Subsurface Lateral Flow in the Shale Hills Catchment as Revealed by Real-Time Soil Moisture Monitoring**

#### **Abstract**

Subsurface lateral flow (SLF) has been observed to contribute substantially to hillslope and catchment runoff. Understanding the occurrence and intensity of SLF is therefore fundamental to conceptualizing subsurface flow and transport in catchment hydrology. In this study, we monitored real-time soil moisture dynamic at different depths and locations along a concave hillslope to investigate the timing and frequency of SLF. By comparing the storage increase at each horizon and total storage increase at each site with rainfall amount, we showed the direct evidence of SLF. Results indicated SLF was ubiquitous at all the monitoring sites and 52% of the 97 rainfall events produced SLF. However, individual monitoring site showed spatial and temporal variation in the occurrence of SLF, which was related to soil type, hillslope location, rainfall, and initial soil moisture. The results also clearly showed a rainfall threshold to initiate the SLF and the threshold value increased from 1.1-2.3 mm from wet to dry season. Although subsurface lateral flow occurred for each site, 9 out of 97 rainfall events showed the connectivity from hilltop to valley floor. In the wet condition, only 1.1~2.3 mm rain can connect SLF from hilltop to valley floor while in dry condition, 14.6 mm rain is needed to deliver water from hilltop to valley floor. In addition, we found that the layers where SLF most likely to occur also varied among different hillslope sites that had different soil series. SLF in shallow Weikert soil occurred in the R horizon while in the deep soil such as Rushtown, SLF frequently occurred in Bw and C horizon. This study enhanced the understanding of mechanism, actual location and potential flow pathway of SLF in a forested catchment and can improve process-based hydrological modeling.

## Introduction

Rainfall-induced subsurface water movement at the hillslope scale is an important process that contributes substantially to runoff (Hewlett and Hibbert, 1965; Whipkey, 1965; Weyman, 1973, Bonell, 1998, Kienzler and Naef, 2008). The occurrence and intensity of subsurface lateral flow (SLF) is affected by a number of factors, such as soil types, topography, precipitation characteristics, and initial soil moisture condition.

Soil properties such as soil macropore, soil layering, and soil depth are essential to understand flow through soils in the landscape scale. For example, Noguchi *et al.*, (1999) found individual macropores that make up preferential flow are typically short, but they can be connected through various mechanisms over relatively long hillslope distances. Brown *et al.* (1999) found rapid delivery of water through O-horizon to stream during summer rainstorms through tracer experiment. By using crest piezometers along slope, while Todd *et al.* (2000) identified the formation of perched water table at the clay rich B horizon that led to saturated flow downslope through more permeable upper A horizon.

Topography has long been known as important control of flow direction. However, most of past research focused on surface topography, while more recent studies have indicated that subsurface topography (such as bedrock topography) was distinctly different from surface topography and that the bedrock topography has a considerable influence on local hydrological gradients and therefore may dominate subsurface flow directions. For instance, Freer *et al.* (1997) reported that total trench flow including macropore flow and matrix flow was correlated to contributing area of bedrock topography instead of surface topography in Panola mountain research watershed Buttle and McDonald (2002) found that a saturated layer with thin soil may quickly develop above the lithic bedrock on forested slopes on the Canadian Shield. Haga *et al.* (2005) demonstrated that saturated subsurface flow above soil–bedrock interface was dominant

subsurface runoff in a small catchment in Mizugaki research watershed.. Tromp-van Meerveld and McDennell (2006) proposed the fill and spill hypothesis to explain the effect of bedrock topography on the hillslope-scale connectivity of subsurface saturated areas.

Soil moisture plays an important role in the initiation and connectivity of subsurface flow. Newman et al (1998) found that when soils were at or near saturation (greater than ~33% volumetric water content), very large volume of SLF can be produced. Grayson et al. (1997) studied the effect of temporal variation in soil moisture on the spatial patterns of soil moisture. In their study, two spatial pattern of soil moisture were proposed. One was the lateral flow-dominated spatial pattern and the other was vertical flow-dominated spatial pattern. They suggested that the transition between two patterns was likely to be in the range of relative soil saturation from 0.6 to 0.8. Study by McNamara et al. (2005) indicated that soil moisture status was related to the hillslope hydraulic connectivity: Low rates of water input to the soil during the winter allow dry soil regions to persist at the soil–bedrock interface, which act as barriers to lateral flow. Once the dry-soil flow barriers are wetted, whole-slope hydraulic connectivity is established, then lateral flow occurs, and upland soils are in direct connection with the near-stream soil moisture.

An important recent advancement is the recognition that the relationship between threshold value and hydraulic connectivity is a necessary condition for the initiation of SLF. Sidle et al. (2000) found that lateral preferential flow occurs only after the hydrologic threshold is reached and subsurface pathways are connected. They proposed a conceptual network model with a series of nodes that link the preferential flow pathway. Three levels of node were proposed according to their easiness of switch on (essentially not switch on, require moderate wetness to switch on, require most wetness to switch on). Tromp-van Meerveld and McDennell (2006) explicitly documented a threshold relationship between subsurface lateral flow initiation and

rainfall based on analysis of 147 rainstorms. Later Lehmann et al. (2007) applied the percolation theory to demonstrate such threshold behavior.

Although SLF is now recognized as a widely observed phenomenon in natural hillslopes, particularly in steep catchments (Markus and MacDonnell, 2004), there remain questions regarding when and where SLF occurs and how it is related to different soil series and landscape positions in a catchment (Lin and Zhou, 2008). In this paper, real-time soil moisture monitoring data along a concave hillslope were used to analyze SLF occurrence in the Shale Hills catchment during 97 rainfall events between 2007 and 2009. This large number of rainstorms allows the exploration of hillslope behavior and the spatial-temporal patterns of SLF. The specific questions we wish to answer were: (1) how often does SLF occur at different hillslope locations and what may be its spatial pattern, (2) how rainfall and seasonal soil moisture change will affect the occurrence of SLF in this hillslope. In other words, is there threshold involved in initiating SLF and making hydrologic connectivity happen from the hilltop to valley floor and (3) are there any “active” layers in this hillslope that would favor the formation of preferential pathways to deliver water downslope?

## **Material and Methods**

### **Study area and soil moisture monitoring sites**

The soil moisture monitoring stations were installed on a hillslope in the Shale Hills Critical Zone Observatory, located in central Pennsylvania. It is V-shaped catchment with area 7.9 ha and characteristic of the low-lying shale hills of the Ridge-and-Valley Physiographic Province in the eastern United States. The soils were formed from shale colluvium or residuum

and a total of five soil series (Weikert, Berks, Rushtown, Blairton, and Ernest series) were identified and are described in the following:

**1** the Weikert series (loamy-skeletal, mixed, active, mesic Lithic Dystrudepts, according to the US Soil Taxonomy) dominates the catchment (78% of the area), which is a thin soil in hilltops or on convex hillslopes, with depth to fractured shale bedrock less than 0.5 m (mostly < 0.3 m);

**2** the Rushtown series (loamy-skeletal over fragmental, mixed, mesic Typic Dystrachrepts) is mostly located in the centre of swales and a large area at the back of the catchment, with > 1 m depth to bedrock (many > 2–3 m);

**3** the Berks series (loamy-skeletal, mixed, active, mesic Typic Dystrudepts) is largely distributed along the slope transitional zones between the shallow Weikert and the deep Rushtown, with 0.5–1 m depth to bedrock

**4** the Ernest series (fine-loamy, mixed, superactive, mesic Aquic Fragiudults) has many (5–40%) redox features and a fragipan-like dense layer starting at 0.3–0.5 m depth;

**5** the Blairton series (fine-loamy, mixed, active, mesic Aquic Hapludults) has an argillic horizon at 0.2–0.8 m depth and few (2–5%) redox features starting at 0.8–1.1 m depth.

Five soil moisture monitoring sites were established along a concave hillslope, covering various hillslope positions and soil series (Figure 3-1). These sites include upper hillslope site 74 and 53, middle hillslope site 51 and 55 and bottom hillslope site 15, which was close to the stream. At each site, a soil pit (~1 m wide by ~3 m long and ~2 m deep) was excavated at for the installation of soil moisture sensors horizontally by generic horizons and their interfaces, based on the in situ observations and laboratory analysis of soil properties. All sites include soil moisture sensors facing upslope direction. However, for the sites 53, 55 and 51, except center sensors that facing upslope direction, there are additional soil moisture sensors that are facing left wall and/ or right wall of soil pit, which were considered as independent sites in this study.

Consequently, the 5 soil moisture monitoring sites can be group into 9 monitoring stations at different location of hillslope, which include 4 upslope stations (site 74 and site 53right, left and center), 4 middle slope stations (site 51 center and left, 55 center and right) and 1 bottom slope stations (site 15) Table 3-1 summarized the position of sensors and basic information and location of sites. A further description of the sites and sensors can be found in Lin and Zhou (2008).

The temporal dynamics of soil moisture in each site were recorded with 10 minutes interval using EC-5 probes (Decagon Devices, Inc., Pullman, WA), which were connected to CR-10X datalogger (Campbell Scientific Inc., Logan, UT). EC-5 probes have an accuracy of 3% without calibration, which was the case in this study. Rainfall was measured also with ten minutes interval by a weather station at the top of hillslope.

In addition, a V-notch weir equipped with a continuous water stage recorder was used to monitor stream discharge at the outlet of the catchment. Stream stage data were collected every 10 minutes with a CR-10X data logger.

## **Data analysis**

### **Occurrence of subsurface lateral flow**

Water balance was applied to each monitoring location as follows:

$$\Delta S = Q_{in} + P - E - D - Q_{out} , \quad (1)$$

where  $\Delta S$  (mm) is total storage increase in a sensor location,  $P$  (mm) is rainfall amount,  $E$  (mm) is evapotranspiration,  $D$  is deep drainage below the depth that the deepest soil sensor was installed in this study,  $Q_{in}$  (mm) is subsurface lateral inflow entering into the sensor location, and  $Q_{out}$  (mm) is subsurface lateral outflow leaving the sensor location.

The total storage increase can be expressed as the summation of storage increase in each horizon as

$$\Delta S = \sum_{i=1}^n \Delta S_i \quad (2)$$

Where  $i$  indicates the soil horizon index,  $n$  is the total number of soil horizons in a particular monitoring site, and  $\Delta S_i$  is the storage increase in soil horizon  $i$ . The storage increase in soil horizon  $i$  can be calculated as

$$\Delta S_i = (\theta_{iE} - \theta_{iS}) \times d_i , \quad (3)$$

Where  $\theta_{iE}$  is the soil moisture content in the horizon  $i$  at the end of the rainfall event,  $\theta_{iS}$  is the soil moisture content in the horizon  $i$  at the beginning of the rainfall event, and  $d_i$  is the thickness of the horizon  $i$ .

Let  $L = E + D + Q_{out}$ , indicating the total loss of soil moisture at a sensor location, and then rearrange Eq. [1], the total storage increase at a given location can be expressed as

$$\Delta S + L = Q_{in} + P . \quad (4)$$

Now considering a rainfall event occurred in a sensor location, there are two possibilities of the difference between  $\Delta S$  and  $P$ :

1)  $\Delta S < P$ , which indicates that the rainfall itself can presumably supply enough water to increase the soil moisture storage. In this case, it is hard to tell whether the lateral inflow  $Q_{in}$  occurred or not unless detail information about  $Q_{in}$  and  $L$  are known; and

2)  $\Delta S \geq P$ , which indicates that the rainfall itself cannot provide enough water to meet the demand of the soil moisture storage increase. In this case, lateral inflow  $Q_{in}$  must have occurred to supplement the water supply to the soil moisture, in addition to the loss of water  $L$ , so that  $Q_{in} \geq L$ .

In this study, we define the occurrence of subsurface lateral flow (SLF) when the  $\Delta S$  is greater than the rainfall amount during a precipitation event. It should be noted the analysis mentioned above only provides the evidence of lateral inflow occurrence at a site, but does not provide information about lateral outflow. However, if we combine inflow information for all the sites along the hillslope, a potential outflow path may be delineated. It also should be noted that

even if  $\Delta S < P$ , SLF may still occur as long as  $0 < Q_{in} < L$ . However, in this study, we cannot determine this with the information we have. Thus, the reported SLF occurrence in this study could be well underestimated. However, the focus of this study was to provide direct evidence of SLF in the Shale Hills CZO and to investigate the main controls of SF occurrence based on real-time soil moisture monitoring.

Based on the soil moisture storage increase in each soil horizon  $\Delta S_i$ , we distinguished two scenarios of SLF occurrence in this study: 1) a strong SLF occurrence when  $\Delta S_i > P$  and  $\Delta S > P$ , and 2) weak SLF occurrence when  $\Delta S_i < P$  but  $\Delta S > P$ . Figure 3-2 gives an example of each of these two scenarios of SLF occurrence.

#### **Data sets**

In this study, a rainfall event used in analysis is identified based on separation time (the time between two distinct rainfall events without any rain in between) and the total rainfall amount during separation time. Three years (1/1/2007-12/31/2009) of rainfall and soil moisture data were used in the analysis. However, a subset of data was selected according to following criteria:

1) The precipitation separation time was selected as 240 minutes and total rainfall amount was greater than 1 mm. This separation time was selected so that the duration of rainfall event was close to the lag time (the time between the onset of a precipitation and the response time of a soil moisture sensor). This was because if separation time was too small, the duration of the rainfall event would be small, which could not capture the response of the sensors especially in the subsurface horizon; but if the separation time was too long, the duration of the rainfall event would be large, which might miss out the transient change of soil moisture.. In this study, we determined the separation time by comparing the mean rainfall duration under different separation time with mean lag time for all sites and all depth. Lin and Zhou (2008) investigated the vertical preferential flow at the same hillslope using real time soil moisture data from

September 23, 2006 to January 1, 2007. In their analysis, the mean lag time for the all the monitoring sites and all depths at dry period and wet period were 512 and 418 minutes respectively. In this study, we averaged these two values and the 465 minutes was selected as mean lag time. we compared duration of precipitation under different separation times using the 3-year actual rainfall data, and the results indicated that when separation time is 4 hours (240 min), duration time of precipitation was close to the lag time 465 min. ( blue dash line in Figure 3-3).

2) In each of the three years, soil moisture data and rainfall data (all 10-minute interval) were selected from March 1 to November 1 to avoid frozen conditions over the winter when soil moisture readings were questionable as well as to avoid the effect of snow on the precipitation data. According to the seasons and initial soil moisture condition from our previous studies, we grouped the monitoring periods into wet period (March 1 to April 30), transition period (May 1 to June 30), and dry period (July 1 to October 31).

3) Soil moisture and rainfall data were available for all the monitoring sites to ensure the comparability across the entire hillslope. Sometime, because of power problems, we lost some data in some sites. Thus, if one site did not have data during a rainfall event, while other sites had, this rainfall event was excluded from the analysis. Consequently, a total of 97 rainfall events were used in this study.

## **Results**

### **Spatial and temporal occurrence of subsurface lateral flow**

Analysis of rainfall and storage increment at each site indicated that about 53% of the total rainfall event produced SLF, in which about 42% of wet rainfall events produce SLF, about

52% of transition rainfall events produce SLF and about 76% of dry rainfall events produce SLF (Table 3-2). The results indicated increasing trend of occurrence of SLF with period from wet to dry. However, the total number of occurrence of SLF was different for each site (Figure 3-4.). This number can roughly be grouped into 3 types. Site 74 and 53 L has relative small number of occurrence, Site 53 R, 53 C, 51L and 15 has relative high number of occurrence and 51C, 55 C and 55R is in between during 97 rainfall events. In addition, the occurrence of SLF also showed seasonality. Figure 3-5 showed the number of occurrence of SLF with seasonal change at each site. Site 74, 53C and 53L showed an increase trend as period from wet to dry. Site 53R, 51C, 55C and 15 showed a decrease trend as period from wet to dry.

#### **Effect of rainfall and seasonal soil moisture change on subsurface lateral flow**

Figure 3-6a showed the relationship between rainfall and total storage increment of occurred SLF for each site at different period. It was obvious that each site had different rainfall value to initiate SLF. In each period, if we choose the minimum rainfall (indicated by the purple dash line) as threshold value to initiate the SLF, we found this value showed an increased trend from wet to dry. Note this value just mean that if rainfall is beyond the value, SLF occurred at least in one site in the hillslope but did not mean SLF occurred in the all site along hillslope. In addition, there was another threshold rainfall value that can increase the storage increment to a significant level. However, this threshold did not show an increase trend from wet to dry.

Figure 3-6b showed the relationship between corresponding initial soil moisture and total storage increment of occurred SLF for each site at different period. However, there was not a clear threshold relationship between initial soil moisture and storage increment as Figure 3-6a showed. Table 3-3 summarized the statistic of SLF occurred at each site. The table indicated that as initial soil moisture became dry, rainfall will increase to initiate the SLF.

### **Effect of soil horizon on subsurface lateral flow occurrence**

Figure 3-7 showed storage increment at different horizons in each site to rainfall event. Red dash line indicated  $\Delta S_i = P$ . Storage increment above this line indicated  $\Delta S_i > P$ , which was the strong occurrence of SLF according to our definition and implied the strong occurrence of subsurface flow at this horizon. By examine the horizon above the red dash line, the ‘active layers’ that the SLF occurred can be identified, which were layers that subsurface water will preferentially choose to move through since the layers had significant entering water than the other layers. It should be noted that subsurface water can still move through other layers. However, the active layers play an important role in lateral delivery of water. Table 3-4 summarized the active layers at each site that the strong SLF most occurred. The general trend is that the depth of active layer goes deep as from upslope to the valley floor. For the upslope site 74, the R horizon at about 30cm is the active layer. For the upslope site 53 and the middle slope site 51 and 55, the C horizons at about 100cm are the active layer. While for the valley floor site 15 the Bt horizon at about 50cm and C horizons at about 100cm are the active layer.

### **Connectivity from upslope to downslope**

Although subsurface lateral flow occurred for each site, its contribution to stream runoff is through the hydraulic connectivity from hilltop to hill bottom. Using occurrence of SLF at valley floor site 15 as indicator of connectivity, the results indicate there are 9 out of 97 rainfall events showed the connectivity from hilltop to hill bottom (Figure 3-4). However, most of these connectivity events occurred during wet and transition period. There is only one event during dry period that indicate the SLF is connected (Table 3-3). Although there were more occurrence of SLF in the dry period than other periods (Table 3-2), these SLF are ‘local’ connected and cannot deliver water to the value floor thus cannot contribute to the runoff. Figure 3-8 used response of soil moisture sensors along hillslope during a rainfall event to demonstrate this situation. Rainfall

in this event is about 5.5 mm, and SLF occurred in upslope site 74 and 53C, middle slope site 51L according to our definition. However, the soil moisture sensors in valley floor show little response, indicate the SLF occurred in upslope cannot connect to the valley floor. On the contrary, Figure 3-9 demonstrated an example of connected SLF at same site along hillslope. In this example, although hill top site 74 did not show the occurrence of SLF, hilltop site 53center, middle slope site 51 left and valley floor site both show the weak occurrence of SLF (total storage exceeds the rainfall amount). Note that the response of A horizon in site 15 show very little change while Bt-2C and 2C horizon showed a great change. This clearly showed the connected SLF from upslope contributed the soil water increase at the valley floor.

Table 3-5 summarized rainfall and initial soil moisture for all the connectivity events at each site. In the wet condition, only 1.1~ 2.3 mm rain can connect SLF from hilltop to hill bottom. However, in dry condition, 14.6 mm rain is needed to deliver water from hilltop to valley floor.

## **Discussion**

### **Ubiquitous subsurface lateral flow**

Our analysis of the 97 rainfall events in this study showed a clear evidence of occurrence of SLF for each monitoring site. However, for the same rainfall event, the spatial occurrence of SLF is different and even for the same site, the occurrence of SLF showed a temporal change. The spatial occurrence of SLF is related to soil series, landscape location and sensor facing. For example, in the shallow Weikert soil at upslope site 74, because of planar slope and close to the hilltop, the contributing area to this site is small indicating less upslope lateral flow will supplement this site. In addition, shallow depth indicates the total storage increment will be limited, which caused the less occurrence of SLF compare to other site according to our definition

SLF. On the contrary, the valley floor site 15 had higher number occurrence of SLF, which was attribute to large contributing area and deep soil depth in this site. However, in the deep Rushtown soil at site 53L, the less occurrence of SLF to may be due to the sensor facing, because the other facing sensor at same location has detect more SLF. The temporal occurrence of SLF may be related to the rainfall, initial soil moisture and connectivity for hilltop to hill bottom. Results in previous section indicated rainfall needs to increase in dry condition to initiate SLF and only when SLF connectivity exists, the occurrence of SLF at upslope can deliver water to middle slope and then to valley floor. For site 15, although more SLF occurred at upslope and middle slope, these SLF were not connected thus reduce the occurrence of SLF at site 15. This also explained decrease occurrence of SLF in middle slope site 51L, 51C, 55C, 55R. It should be noted that we only chose the rainfall events that all sites had soil moisture data. The actual occurrence of SLF should be higher.

### **Pathway and connectivity along the hillslope**

Soil horization has significant impacts on occurrence of SLF because significant changes in texture or density across the boundary of two adjacent layers could noticeably alter water distribution. The results provide information about the potential soil horizons that water will enter in at each site. By linking this information and soil information along the hillslope, a potential lateral flow pathway can be delineated. According to the results in table 3-4, three conceptual pathways are delineated in figure 3-10. The first pathway is water lateral movement along Bw and C interface to recharged Bw horizon located in downslope site (blue dot-dash line in figure 3-10). In table 4, almost all Bw horizons (except for 51C) in upslope site 53 and middle slope sites 51 and 55 detected SLF. Several moisture sensors installed at Bw-C interface (53R and 55R) provide direct evidence that water moving

along the interface. The second pathway is water moving through the fracture of bedrock and directly recharging deep C horizon in downslope site (blue solid line in figure 10). This is obvious especially in the upslope site 53. The upslope of this site was dominated by shallow Weikert soil with depth between 30 -50 cm. The detection of SLF in deep C horizon (about 1m) in this site is most likely to be water in the fracture of bedrock moving laterally under slope gradient and supplementing storage increase in deep soil horizon downslope. In addition, detection of SLF in C horizon was also observed in middle slope site and valley floor site (Table 3-4). The third pathway is lateral water movement along Bt-C interface (blue dotted line in figure 3-10). Compare to the other findings that lateral flow occurred when water table was perched at soil-bedrock interface (Tromp-van Meerveld and McDennell, 2006) or impermeable layer (Todd et al. 2000), the data in this hillslope reveal another mechanism that deliver water downslope.

#### **Implication for hydrologic modeling**

Connectivity of local SLF from hilltop to the valley floor indicated existence of subsurface flow network. Soil moisture at certain hillslope location may function as important “nodes” and the soil horizon may function as “path” in subsurface flow network. Such flow network was strongly influenced by soil properties such as soil series, soil depth, permeability, and soil location in hillslope. In certain conditions, such as high soil moisture content, strong and/ or long duration rainfall, the “nodes” may be activated and deliver water downslope through the “path”. This implied that different soil series and their detailed spatial distributions in the hillslope or catchment were needed in the model to improve prediction of SLF. In our example, SLF in shallow Weikert soil occurred in the R horizon while in the deep soils such as Rushtown, SLF frequently occurred in Bw and C horizon, which indicate that water may infiltrate into bedrock fractures below shallow Weikert soils and move laterally to supplement the deep horizon

of downslope soils. This suggested that incorporation detailed soil information into the model will enhance the understanding water flow mechanism and help determine the actual location of SLF. Another advantage will be correctly predicting flow pathways in the model. The identified “active” layer in the study showed a potential flow pathway to deliver water from hilltop to the valley floor. Incorporating this information into the model will not only accurately predict subsurface flow direction but transport of solutes driven by water flow.

### **Conclusions**

Our analysis of the real –time soil moisture based on 97 rainfall events over 3 years indicated that SLF was ubiquitous along the hillslope studied and 52% of rainfall events produced SLF at one or more monitoring sites. However, the occurrence of SLF varied from each individual monitoring site and showed the threshold value to the rainfall amount. which was related to soil series, hillslope location, rainfall, and initial soil moisture.

By comparing the storage increment in each soil horizon with rainfall, we identified the layers where water tended to preferentially move through (these layers are R horizon in the shallow Weikert soil at hilltop, Bw and C horizon in the deep Rushtown soil and Berks soil at middle slope and Bt and C horizon in the deep Ernest soil at valley floor.). By linking this information and soil information along the hillslope, a potential pathway can be delineated. That is water may infiltrate into bedrock fracture below shallow Weikert soil and move laterally to supplement the deep horizon of downslope soil.

Although locally occurring SLF is common in the studied hillslope, there were only 9 events that indicated connection of the locally occurred SLF. Results indicated that eight connecting events occurred during the wet and transition period with small rainfall (1.1~2.3 mm),

one event occurred under the dry condition with large rainfall (14.6mm). Our results indicate that small rainfall (1.1~2.3 mm) can connect subsurface lateral flow from hilltop to valley floor during the wet period, while large 14.6 mm rainfall are needed to build the connection from hilltop to valley floor under the dry condition. The results about connectivity also explained the less contribution of SLF to the valley floor during dry period although more occurrence of SLF in dry condition. Analyses of real-time soil moisture in this study provide valuable information on spatio-temporal occurrence of SLF and potential subsurface flow direction in the Shale Hills Critical Zone Observatory. The results indicated the existence of subsurface flow network, which is influenced by soil properties (such as soil series, soil depth, permeability, and soil location) that control the connection of locally occurred SLF. This suggests that incorporation detailed soil information into the model will improve accuracy and realistic of prediction. The methodology illustrated in this study is beneficial in enhancing the understanding of subsurface flow processes and modeling of landscape hydrology at the hillslope and catchment scales.

## References

- Bonell, M. 1998. Selected challenges in outflow generation research in forests from the hillslope to headwater drainage basin scale, *Journal of the American Water Resources Association* 34, 765–785.
- Buttle, J.M., and D.J. McDonald. 2002. Coupled vertical and lateral preferential flow on a forested slope. *Water Resour. Res.* 38: 1060, doi:10.1029/2001WR000773.
- Freer, J., McDonnell, J. J., Beven, K. J., Brammer, D., Burns, D., Hooper, R. P., and Kendall, C. 1997. Topographic controls on subsurface storm flow at the hillslope scale for two hydrologically distinct small catchments, *Hydrol. Processes*, 11: 1347–1352.

- Grayson, R.B., Western AW, Chiew FHS, Blöschl G. 1997. Preferred states in spatial soil moisture patterns: local and nonlocal controls. *Water Resources Research* 33: 2897–2908.
- Haga, H., Y. Matsumoto, J. Matsutani, M. Fujita, K. Nishida, and Y. Sakamoto. 2005. Flow paths, rainfall properties, and antecedent soil moisture controlling lags to peak discharge in a granitic unchanneled catchment. *Water Resour. Res.*, 41: W12410, doi:10.1029/2005WR004236.
- Hewlett, J. D., and A. R. Hibbert. 1965. Factors affecting the response of small watersheds to precipitation in humid areas, Paper Presented at International Symposium on Forest Hydrology, Pa. State Univ., University Park.
- Lin, H. 2006. Temporal Stability of Soil Moisture Spatial Pattern and Subsurface Preferential Flow Pathways in the Shale Hills Catchment. *Vadose Zone Journal*.5:317-340.
- Lin, H. and Zhou X. 2008. Evidence of subsurface preferential flow using soil hydrologic monitoring in the Shale Hills catchment. *European J. Soil Sci.* 59:34-49.
- McNamara, J. P., D. C. Mark Seyfried and Shiva Achet (2005). "Soil moisture states, lateral flow, and streamflow generation in a semi-arid, snowmelt-driven catchment." *Hydrological Process.*: 4023–4038.
- Newman, B.D., Campbell, A.R., Wilcox, B.P. 1998. Lateral subsurface flow pathways in a semiarid ponderosa pine hillslope. *Water Resources Research* 34: 3485–3496.
- Noguchi S, Tsuboyama Y, Sidle RC, Hosoda I. 1999. Morphological characteristics of macropores and the distribution of preferential flow pathways in a forested slope segment. *Soil Sci. Soc. Am. J.* 63: 1413–1423.
- Todd, M.S., Jeff, P.R., George M.H. 2000. Shallow subsurface storm flow in a forested headwater catchment: Observations and modeling using a modified Topmodel. *Water Resources Research* 36(9), 2575–2586.

- Sidle, R., S. Noguchi, Y. Tsuboyama, and K. Laursen. 2001. A conceptual model of preferential flow systems in forested hillslopes: evidence of self-organization. *Hydrological Processes* 15, 1675–1692.
- Tromp-van Meerveld, H. J. and McDonnell, J. J. 2006. Threshold relations in subsurface stormflow 1. A 147 storm analysis of the Panola hillslope, *Water Resources Research* 42, W02410, doi:10.1029/2004WR003778.
- Weiler and McDonnell. 2004. Virtual experiments: a new approach for improving process conceptualization in hillslope hydrology. *J. Hydrol.* 285, 3-18.
- Weyman, D. R. 1973. Measurements of the downslope flow of water in a soil. *J. Hydrol.* 20, 267–288.
- Whipkey, R. Z. 1965. Subsurface stormflow from forested slopes. *Bull. Int. Assoc. Sci. Hydrol.* 10, 74–85.

Table 3-1: Soil and landscape features at 9 monitoring stations

Hillslope position	Site number (and orientation)	Landform (sensor installation orientation)	Slope/%	Soil series	Soil horizon	Sensor installation depth/cm	Depth to bedrock/cm	Rock fragment/%	Soil texture
Upslope	74	Nearly planar slope(facing upslope direction)	23.8	Weikert	Oe-A	5	22	0	Silt loam
					A	8			
					A-CR	10			
					CR	17			
Upslope	53(left)	Swale (facing left sideslope)	38.4	Rushtown	Oe-A	5	>150	5	Silt loam
					A	10			
					Bw2	40			
					BC-C	97			
	53(center)	Swale( facing upslope direction)	Rushtown		A	10	>150	5	Silt loam
					Bw1	22			
					Bw2	44			
					Bw3	73			
	53(right)	Swale( facing rightslope )	Berks		Oe-A	5	>110	0	Silt loam
					A	10			
					Bw2	40			
					BW3-C	88			
Middle slope	51(left)	Swale( facing leftslope )	13.1	Rushtown	A	8	>300	5	Silt loam
					Bw1	18			
					Bw3	39			
					C1-C2	115			
	51(center)	Swale( facing upslope direction)	Rushtown		Oe-A	5	>300	5	Silt loam
					A	8			
					A-Bw1	12			
					Bw1	15			
					Bw2	22			
					Bw3	40			
					BC	68			
					BC-C1	92			
C1	122								
Middle slope	55(center)	Swale( facing upslope direction)	27.9	Berks	Bw1	14	>150	2	Silt loam
					Bw2	41			
					Bw3	86			
					BW3-C	90			
	55(right)	Swale( facing rightslope)	Berks		Oe-A	5	>150	0	Silt loam
					A	7			
					Bw3-C1	84			
					C2	141			
Valley floor	15	Valley floor (facing the upstream direction)	6.6	Ernest	A	13	> 300	0	Silt loam
					AE-Bw	20			
					Bt	41			
					Bt-2C	52			
					2C	72			
					2C-3C	85			
					4C	109			

Table 3-2 : Statistics of the 97 rainfall events selected from 1/1/2007 to 12/31/2009 and SLF occurrence. Wet period is defined from March 1 to April 30, transition period is from May 1 to June 30, and dry period is from July 1 to October 31

Period	Number of event	Average rainfall (mm)	Max rainfall (mm)	Min rainfall (mm)	Max rain intensity (mm/10 min)	Number of SLF occurrence SLF	Number of strong SLF occurrence	Number of event with weak SLF occurrence
Wet	45	7.7	21.3	1.1	7.3	20	12	8
Transition	31	8.3	35.9	1	14.1	15	11	4
Dry	21	8.7	48.4	1.1	8.8	18	7	11
<b>Total</b>	<b>97</b>	<b>8.1</b>	<b>48.4</b>	<b>1</b>	<b>14.1</b>	<b>53</b>	<b>30</b>	<b>23</b>

Table 3-3: Statistics of SLF occurrence at each monitoring site from 2007-2009. ISM is the initial soil moisture (% by volume) and ds is the total storage increase during each rainfall event

	Site	74	53-Right	53-Center	53-Left	51-Left	51-Center	55-Center	55-Right	15	All (Mean)
<i>Wet Period</i>											
Number of occurrence		0	6	1	0	5	3	3	3	4	2.8
Min rainfall (mm)		0	2.1	2.8	0	2.8	2.9	2.9	2.9	1.1	2.5
Max rainfall (mm)		0	20.2	2.8	0	20.2	20.2	21.3	20.2	3.0	15.4
Average rainfall (mm)		0	9.1	2.8	0	8.5	9.4	14.8	13.0	2.2	8.5
Min ISM (%)		0	16.9	13.3	0	18.4	17.8	19.4	21.2	38.7	20.8
Max ISM (%)		0	19.7	13.3	0	21.0	19.8	22.4	23.0	39.2	22.6
Average ISM (%)		0	18.6	13.3	0	19.7	18.9	21.0	22.3	38.9	21.8
Min Total dS (mm)		0	4.8	4.6	0	3.3	3.3	3.0	5.1	3.6	4.0
Max total dS (mm)		0	32.7	4.6	0	37.0	29.3	28.8	33.3	18.1	26.3
Average total dS (mm)		0	13.9	4.6	0	15.8	15.0	18.8	18.9	8.3	13.6
<i>Transition Period</i>											
Number of occurrence		2	2	4	2	1	2	2	4	4	2.6
Min rainfall (mm)		3.5	6.1	2.6	1.9	30.7	1.9	6.1	2.6	6.1	6.8
Max rainfall (mm)		8.3	8.3	30.7	8.3	30.7	1.9	8.3	35.9	30.7	18.1
Average rainfall (mm)		5.9	7.2	11.2	5.1	30.7	1.9	7.2	19.4	18.9	11.9
Min ISM (%)		13.2	13.2	16.0	16.9	16.1	17.3	15.8	16.5	21.4	16.3

<b>Max ISM (%)</b>	15.7	18.2	21.0	23.7	16.1	20.6	17.8	22.0	33.1	20.9
<b>Average ISM (%)</b>	14.4	15.7	18.3	20.3	16.1	19.0	16.8	18.2	30.0	18.8
<b>Min Total dS (mm)</b>	6.1	8.8	4.4	2.5	43.5	2.0	6.3	2.7	24.4	11.2
<b>Max total dS (mm)</b>	10.4	18.6	101.5	9.2	43.5	2.5	51.5	62.5	36.3	37.3
<b>Average total dS (mm)</b>	8.3	13.7	41.3	5.9	43.5	2.2	28.9	36.2	31.4	23.5
<i>Dry Period</i>										
<b>Number of occurrence</b>	3	2	7	2	3	1	2	0	1	2.3
<b>Min rainfall (mm)</b>	2.3	16.3	4.3	5.5	3.6	13.3	2.3	0	14.6	7.8
<b>Max rainfall (mm)</b>	10.6	48.4	20.7	16.3	16.3	13.3	10.6	0	14.6	18.9
<b>Average rainfall (mm)</b>	6.1	32.4	11.9	10.9	8.5	13.3	7.2	0	14.6	13.1
<b>Min ISM (%)</b>	11.1	11.5	12.4	13.5	11.9	14.2	13.4	0	19.4	13.4
<b>Max ISM (%)</b>	12.8	13.8	16.3	14.8	14.3	14.2	16.3	0	19.4	15.2
<b>Average ISM (%)</b>	12.1	12.6	13.9	14.1	13.1	14.2	14.4	0	19.4	14.2
<b>Min Total dS (mm)</b>	2.8	34.2	13.0	10.1	4.0	13.8	15.0	0	39.8	16.6
<b>Max total dS (mm)</b>	17.3	48.9	30.8	17.0	18.0	13.8	15.8	0	39.8	25.2
<b>Average total dS(mm)</b>	8.7	41.5	20.2	13.6	11.6	13.8	15.4		39.8	20.6

Table 3-4: Statistics of the occurrence of strong subsurface lateral flow during 97 rainfall events from 2007 and 2009.

Site number	Soil series	Soil horizon	Number of occurrence of strong SLF	Frequency of strong SLF occurrence in 97 rainfall event (%)
74	Weikert	R	2	2.06
53(Right)	Berks	Bw2	1	1.03
		Bw3-C	3	3.09
		C	1	1.03
53 (Center)	Rushtown	Bw1	4	4.12
		Bw2	3	3.09
		Bw3	1	1.03
53(Left)	Rushtown	Bw2	1	1.03
		C	1	1.03
51(Left)	Rushtown	Bw3	3	3.09
		C1-C2	2	2.06
51(Center)	Rushtown	C2	1	1.03
55(Center)	Berks	Bw1	2	2.06
		Bw3	2	2.06
55(Right)	Berks	Bw3-C1	4	4.12
		C2	1	1.03
15	Ernest	Bt	1	1.03
		Bt-2C	1	1.03
		2C	2	2.06
		4C	3	3.09

Table 3-5: Statistics of the occurrence of connectivity events. (Connectivity events is the events that SLF occurred at valley floor site 15, which indicate the lateral flow from upslope)

Monitoring Period	Event #	Duration (minute)	Rainfall features		Initial soil moisture (% by volume)									Average
			Rainfall (mm)	Max Intensity (mm/10 min)	15	74	53-Right	53-Center	53-Left	51-Left	51-Center	55-Center	55-Right	
Wet	1	180	1.1	0.2	38.8	18.3	18.1	17.0	22.6	19.1	19.4	20.3	21.9	21.7
	2	340	3	0.3	38.7	18.0	17.9	16.6	22.5	19.0	19.2	20.1	21.7	21.5
	3	290	2.3	0.2	38.7	18.9	18.0	17.6	22.6	19.1	19.3	20.1	21.6	21.8
	4	370	2.2	1	39.2	19.5	19.3	18.1	23.2	19.8	20.0	21.1	22.6	22.6
Transition	5	570	17.4	2.1	33.0	17.4	16.9	16.2	22.0	18.5	18.8	18.9	19.5	20.1
	6	630	6.1	0.3	32.3	19.2	19.1	18.0	22.0	20.6	19.2	18.2	18.3	20.8
	7	160	30.7	14.1	21.4	14.6	13.4	18.6	16.8	16.1	16.8	15.7	16.5	16.7
Dry	8	1360	21.4	1.1	33.1	17.2	17.5	16.0	22.2	19.0	18.9	17.4	17.7	19.9
	9	990	14.6	1.4	19.4	15.9	12.4	14.4	14.9	12.4	12.0	11.9	12.4	14.0

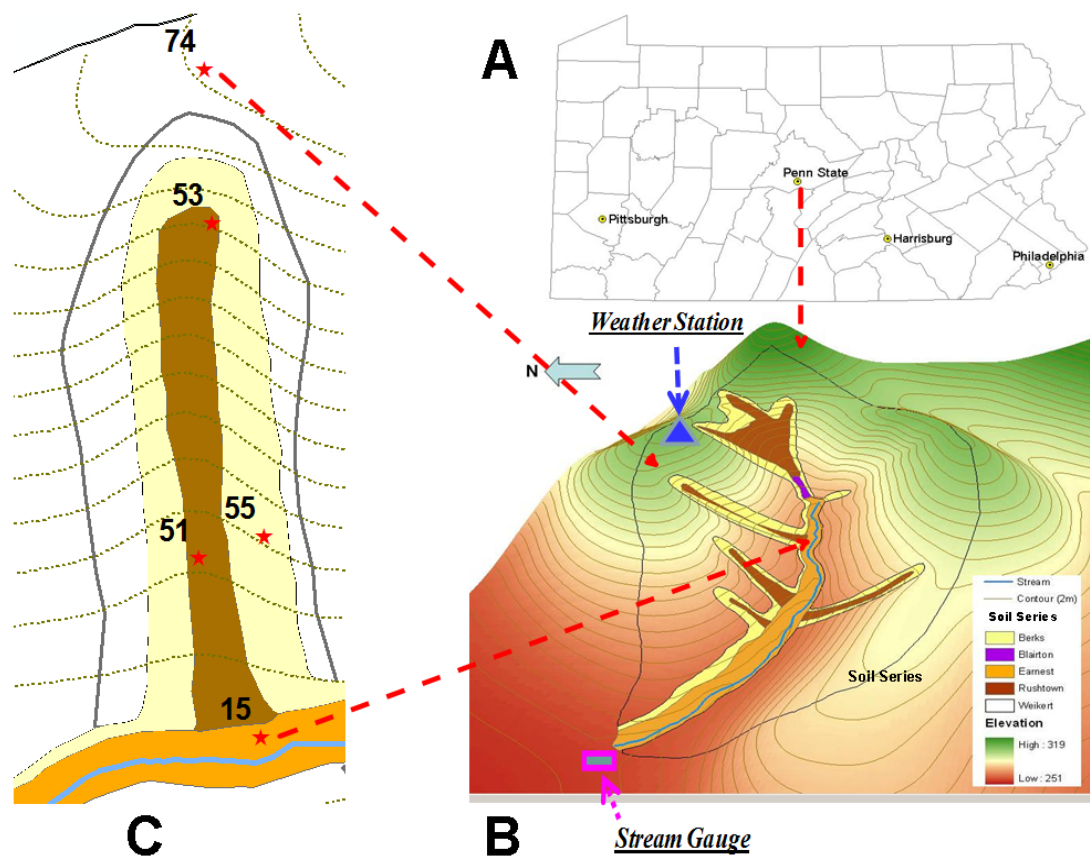


Figure 3-1: Location of the Shale Hills catchment and the study hillslope

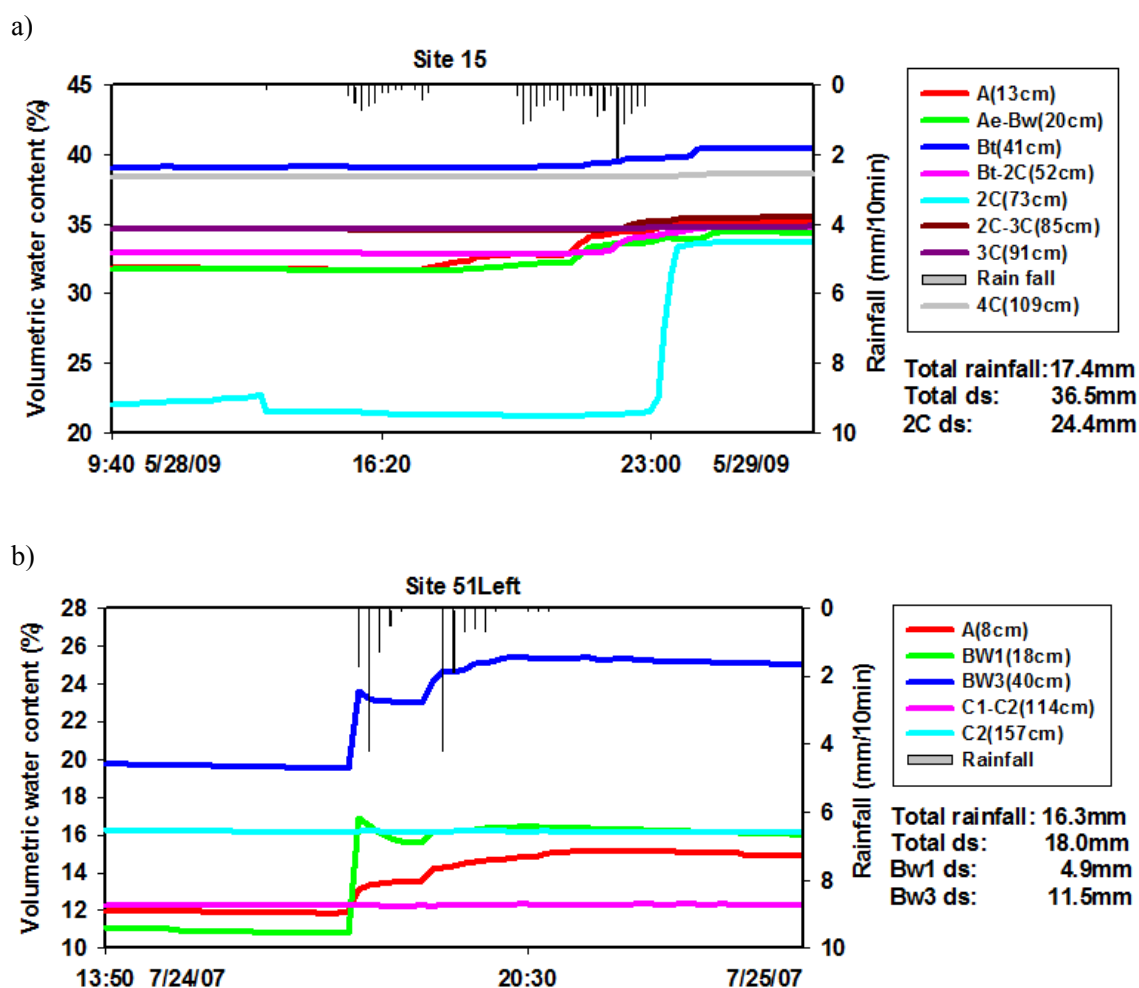


Figure 3-2: (a) An example of strong subsurface lateral flow occurred in site 15. Note the moisture storage increase (ds) in the 2C horizon is greater than the total rainfall amount. (b) An example of weak subsurface flow occurred in site 51left. Note the total profile moisture storage increase (total ds) is greater than the total rainfall amount

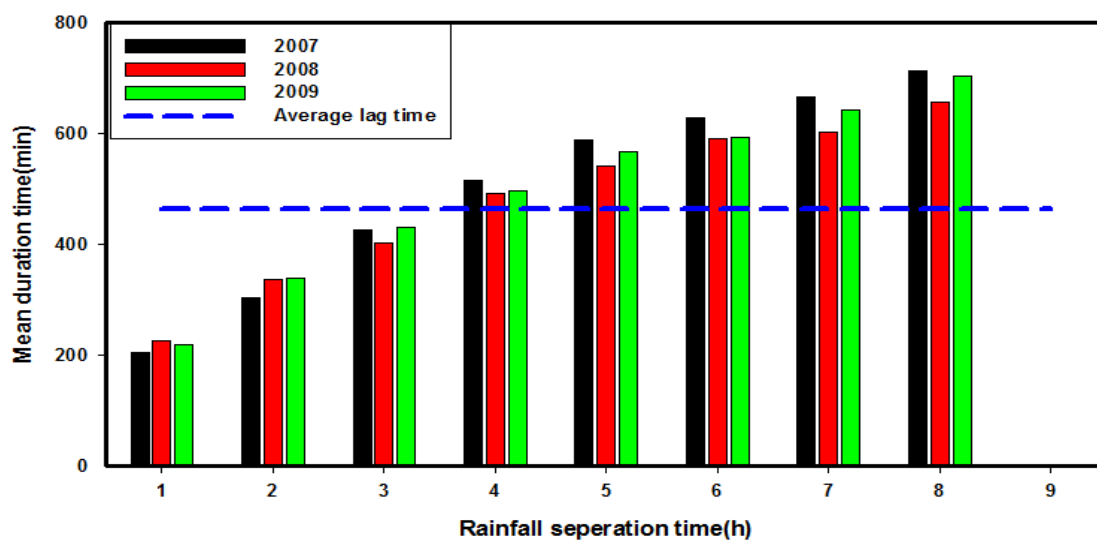


Figure 3-3: Relationship between rainfall separation time and mean rainfall duration . for all the sites and all depths. This value was taken from Lin and Zhou (2008) who analyzed soil moisture data at the same hillslope as this study. When rainfall separation time is 4 hours (240 minutes), the mean rainfall duration is close to the average lag time

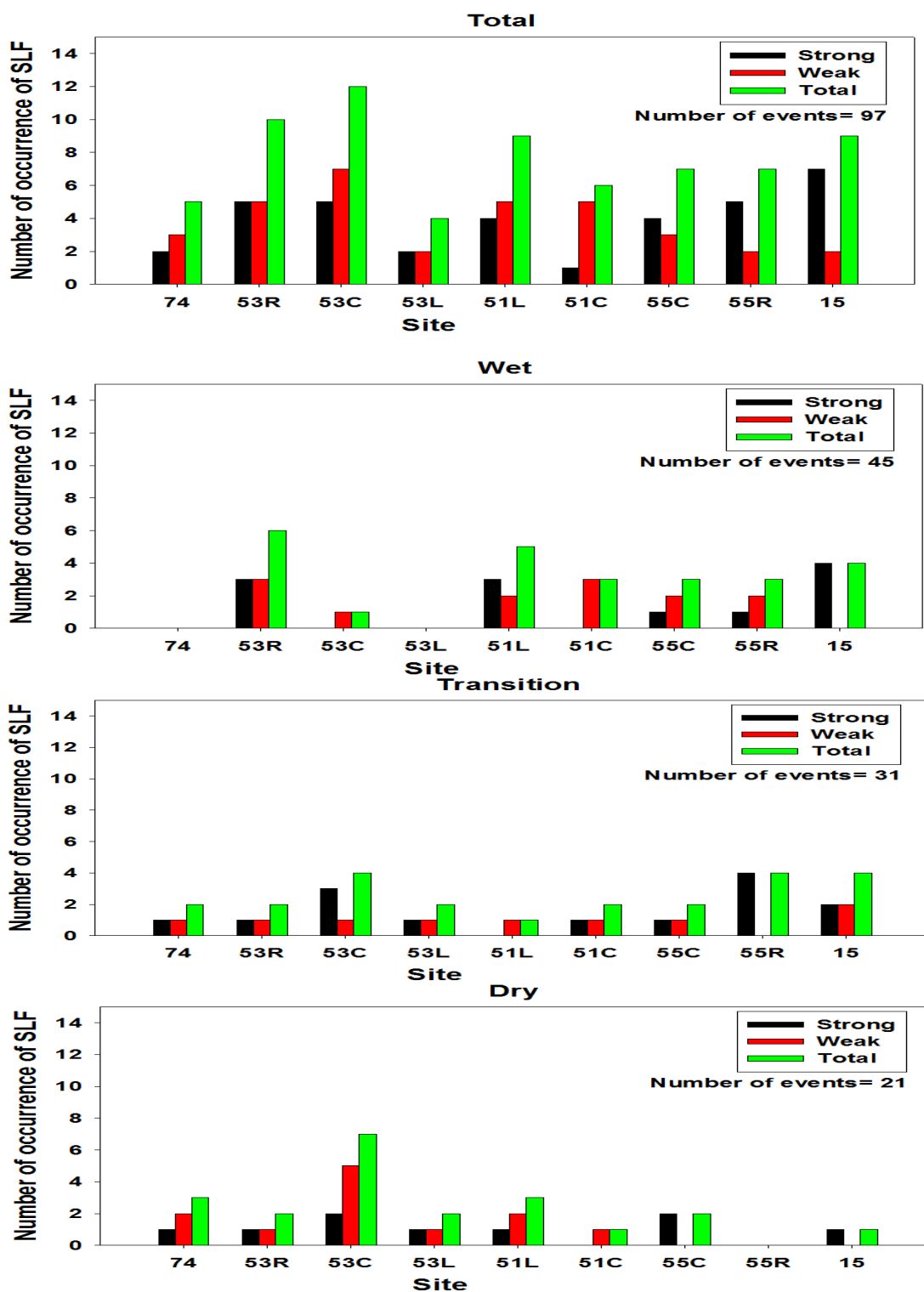


Figure 3-4: Number of occurrence of strong and weak subsurface lateral flow in each of the 9 monitoring sites during wet, transition, and dry periods

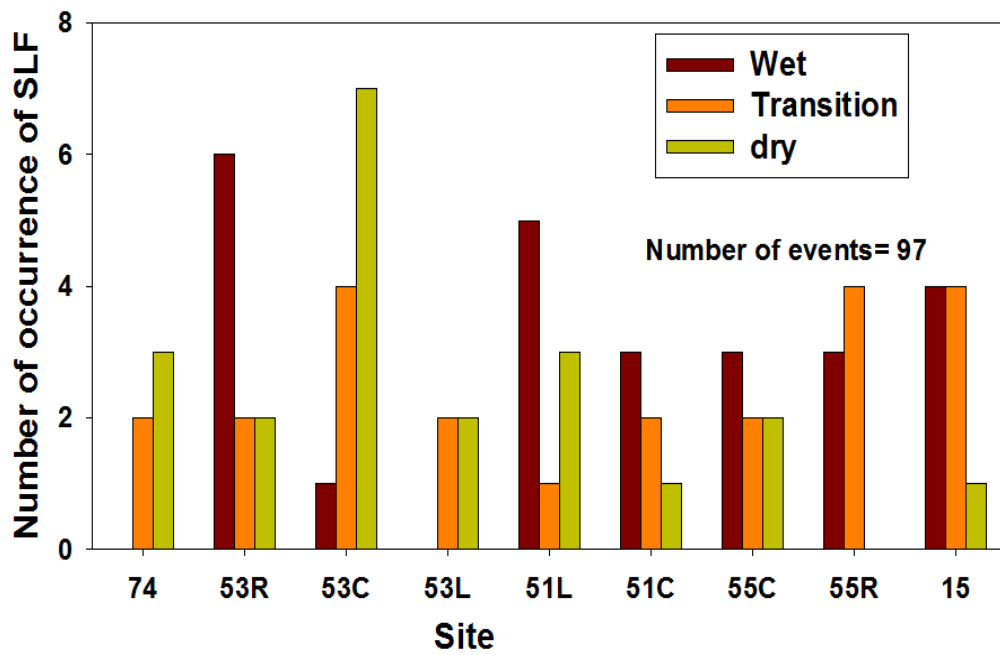


Figure 3-5: Number of occurrence of subsurface lateral flow events at each of the 9 monitoring sites during wet, transition, and dry periods. Blue dash line indicates number of occurrence equal to 1 and the bar below this line indicates number of occurrence is zero

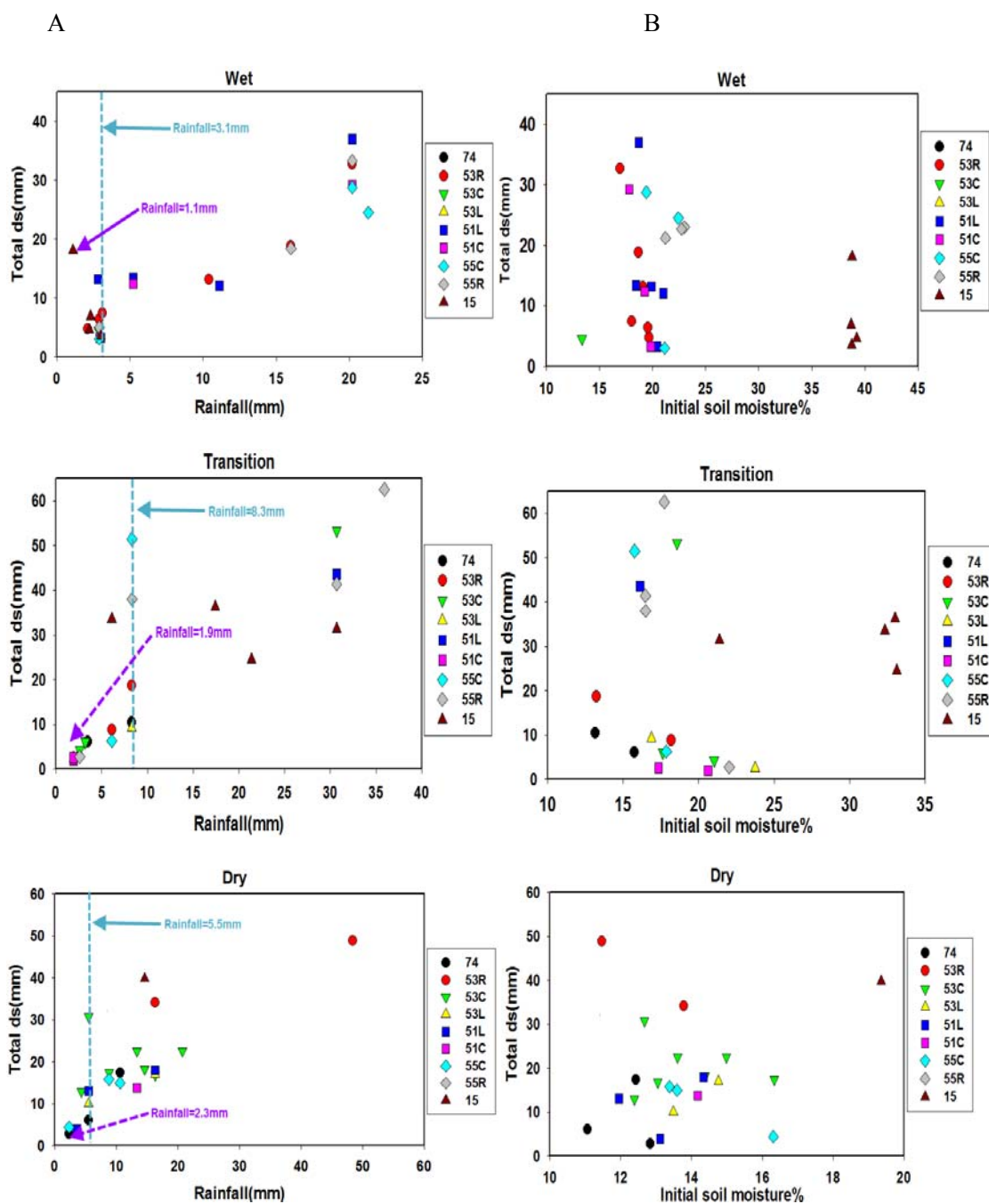


Figure 3-6: A. Relationship between rainfall amount and total storage increase (ds) during subsurface lateral flow (SLF) at each site during different periods. Purple dash line indicates the threshold rainfall to initiate the SLF. Light blue indicate the threshold rainfall to increase storage to a significant amount. B. Relationship between initial soil moisture and total storage increase during SLF at each site during different periods

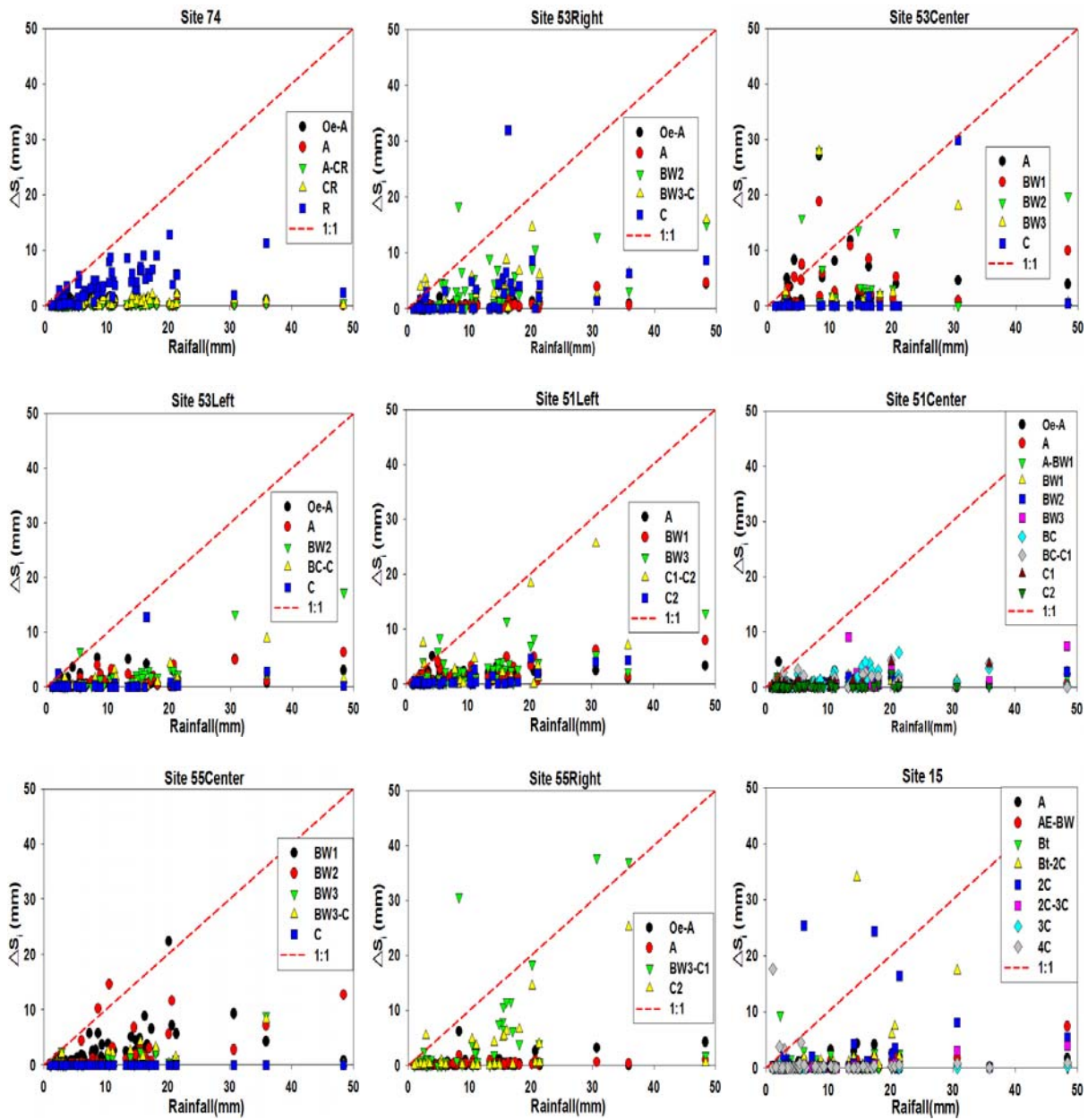


Figure 3-7: Relationship between rainfall amount and storage increase in different horizons at each site during all of the 97 rainfall events. Red dash line indicate  $\Delta S_i=P$ . The symbols above this line indicate the soil horizons that had subsurface lateral flow

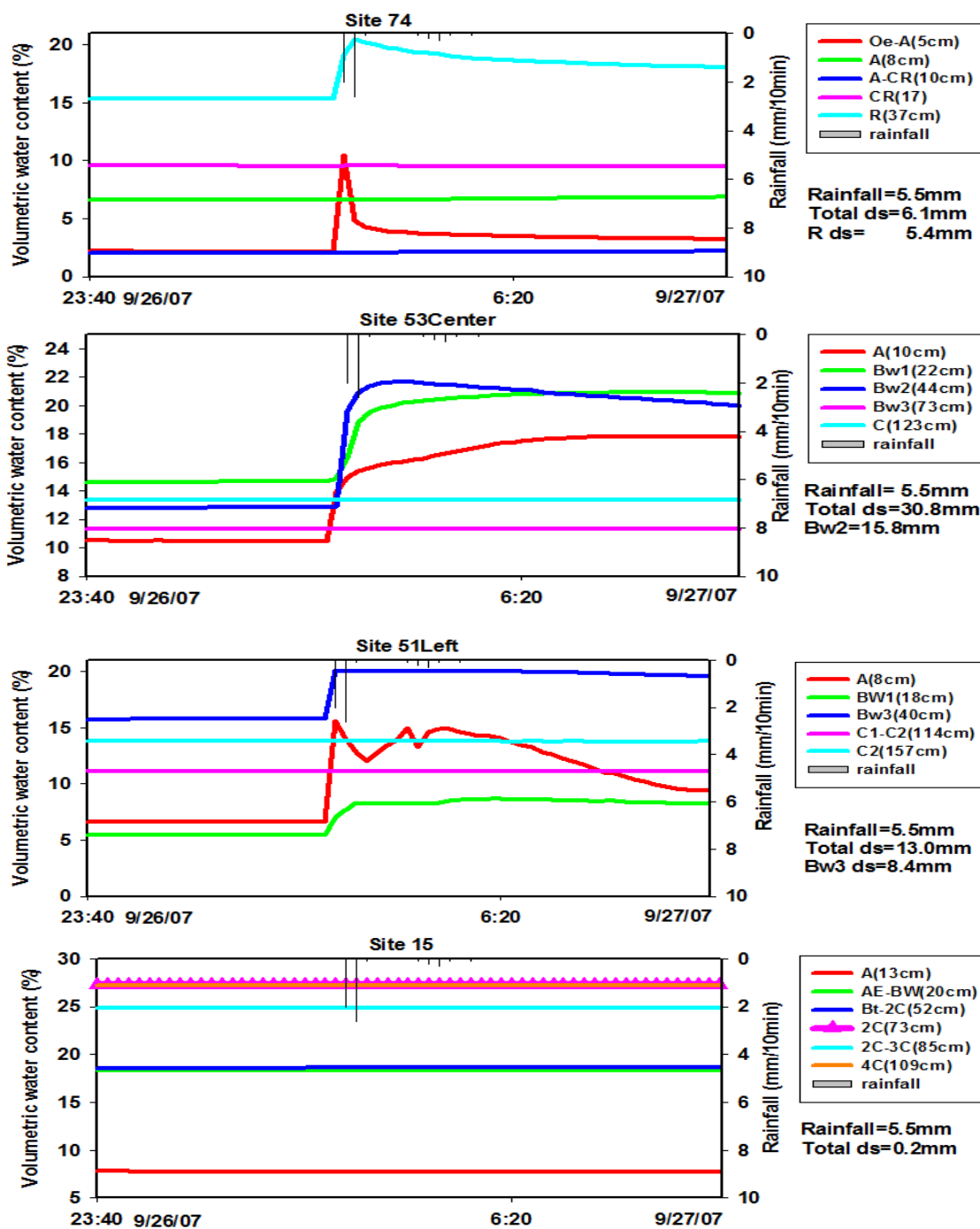


Figure 3-8: Example of the disconnected flow from the hilltop to the valley floor. Total storage at upslope site (74 and 53 center) and middle slope site (51 left) were both above rainfall, indicating occurrence of SLF, while total storage in the valley floor site 15 showed very small increment compared to rainfall, indicating flow path was not connected from upslope to the valley floor

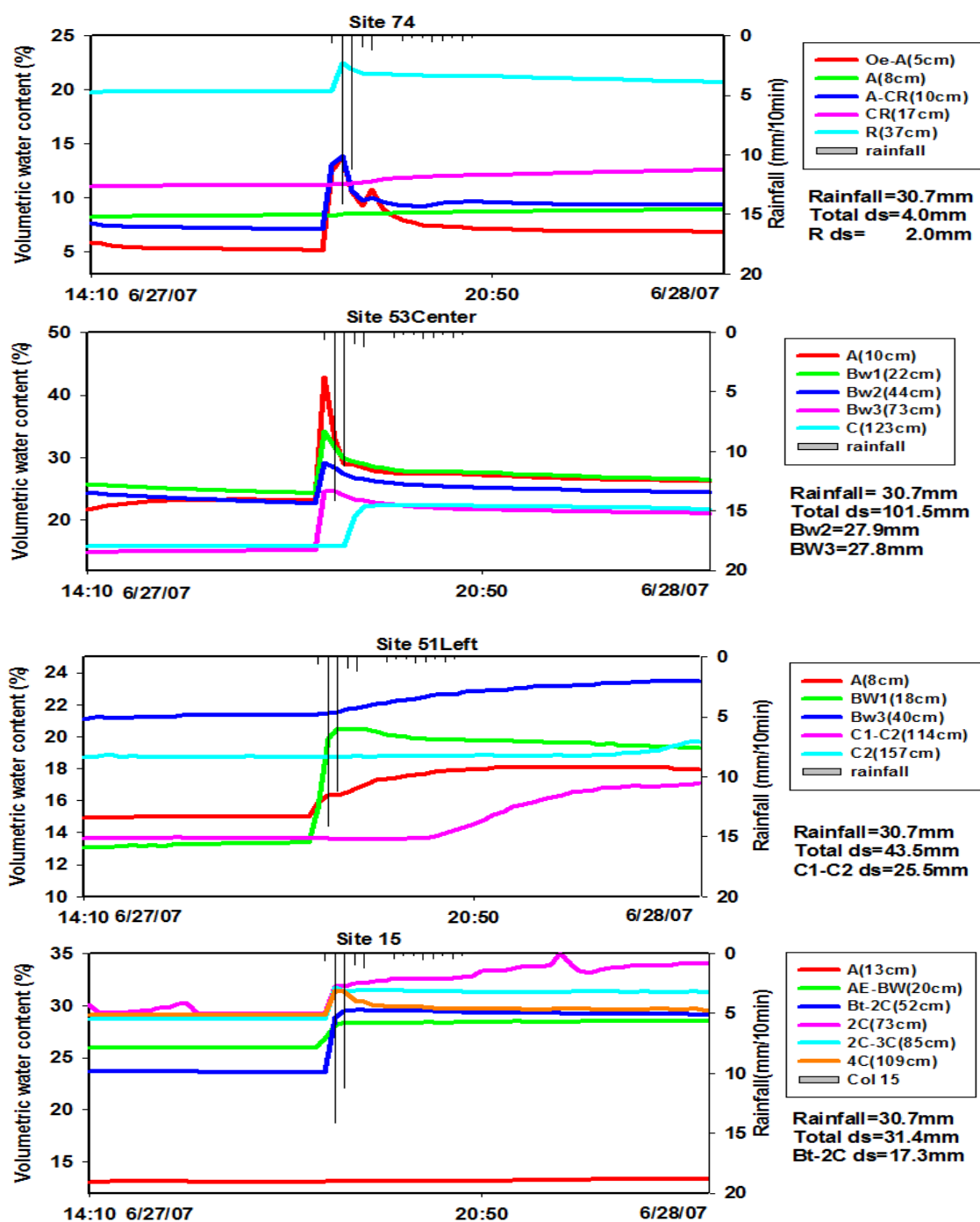


Figure 3-9: Example of the connected flow from the hilltop to the valley floor during a rainfall event. Except for hill top site 74, weak SLF (total storage exceeded the rainfall amount) occurred along the hilltop site 53, middle slope site 51 and valley floor site 15, indicating connected SLF from hilltop to valley floor

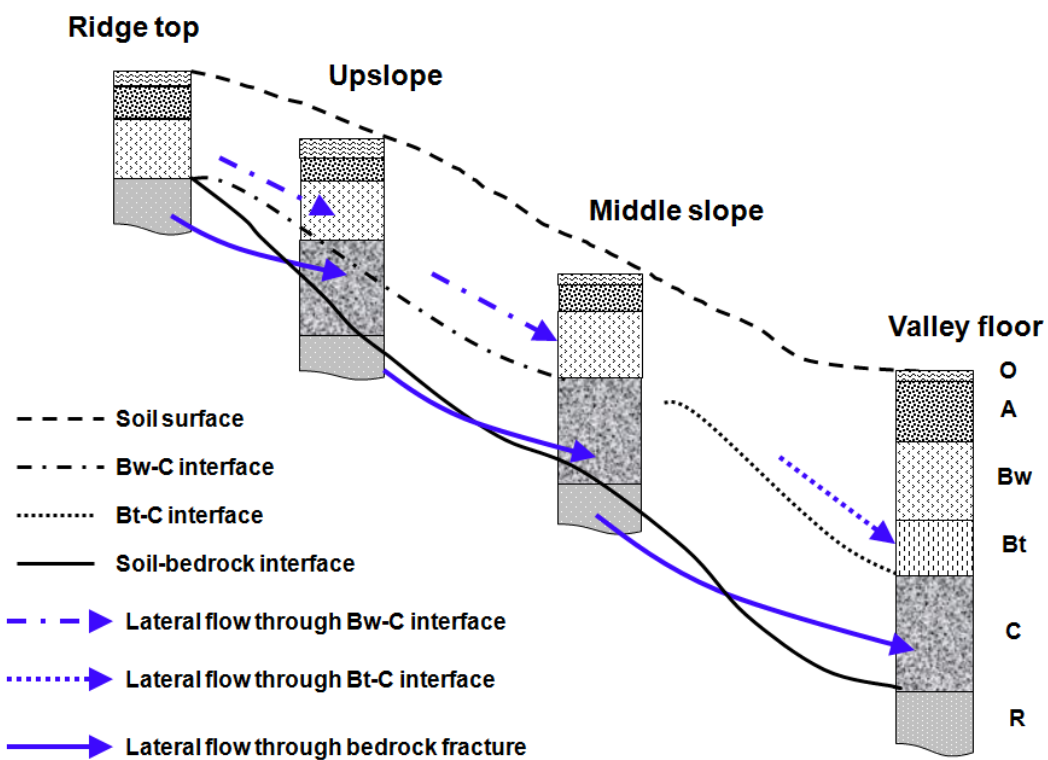


Figure 3-10: A conceptual diagram showing the potential flow pathways along a hillslope in the Shale Hills catchment.

## Chapter 4

### **Hillslope Subsurface Flow Revealed by Time-lapsed Ground Penetrating Radar and Real-Time Soil Moisture Monitoring**

#### **Abstract**

Subsurface lateral flow has been observed to contribute substantially to hillslope and catchment runoff. However, direct observation of the occurrence and distribution of subsurface lateral flow in hillslopes has been difficult because of the complexity of non-uniform flow and the lack of appropriate means to directly observe flow pathways and their dynamic changes. In this study, we explored the combined use of time-lapsed Ground Penetrating Radar (GPR) imaging and real-time soil moisture monitoring to identify subsurface flow pathways in two contrasting soil transects in the Shale Hills Critical Zone Observatory. The real-time soil moisture monitoring showed that subsurface lateral flow occurred in top 20-cm soil after artificial water infiltration into the shallow Weikert soil in a planar hillslope with 30% slope, whereas vertical flow dominated in the deep Rushtown soil located in a concave hillslope (swale) with 15% slope. The time-lapse GPR radargrams revealed the general infiltration wetting front and preferential flow pattern that were significantly different between the two types of soils and hillslopes, which were then confirmed by simulation modeling results. Through comparing simulated radargrams generated from four conceptual flow models with the field observed GPR data, we were able to confirm that subsurface lateral macropore flow was dominant in the shallow Weikert soil, while a combination of vertical macropore flow and lateral matrix flow was dominant in the deep Rushtown soil under the experimental conditions of this study. Time-lapsed GPR is proved as a useful methodology for improved understanding of hydrologic connectivity in the subsurface,

which facilitates the formulation and test of different conceptualizations of subsurface network modeling.

### **Introduction**

Subsurface lateral flow in catchment hillslopes has been observed to contribute substantially to direct runoff (Hewlett and Hibbert, 1965; Whipkey, 1965; Weyman, 1973, Bonell, 1998, Kienzler and Naef, 2008). But understanding where and how the subsurface concentrated flow occurs has been difficult because many factors can induce subsurface lateral flow, such as bedrock topography, soil layering, macropore network, and precipitation threshold (Todd et al., 2000; Sidle et al., 2001; Weiler and McDonnell, 2004; Tromp-van Meerveld and McDonnell, 2006; Lin and Zhou, 2008). In addition, the lack of effective means to directly observe subsurface structure has constrained our understanding of subsurface flow pathways and mechanisms. Traditional methods have largely been destructive or based on interpolation between point-based measurements (e.g., Freer et al, 2004; Sidle, et al 2001). As a result, transient phenomena or spatially-varying occurrence of subsurface preferential flow could not be easily and precisely determined (Lin, 2010).

Ground Penetrating Radar (GPR) has become a popular geophysical tool for detecting subsurface features (Grasmueck, 1996; Gerber, et. al., 2007; Poisson et al., 2009). Its use for monitoring nearly real-time subsurface water flow dynamics, however, has been limited. Application of GPR relies on contrasting electrical impedance of the media being investigated, which is primarily determined by dielectric and conductive properties of the material, its magnetic permeability, and its physical properties (Daniels, 2004). For most of natural soils, water content change is a main factor impacting GPR reflection because the dielectric constant of water is about 80 while that of dry soil is between 3 and 5 (Gish et al., 2002). Such a contrast between water and surrounding drier soils make it possible to track the subsurface water flow through repeated GPR scans after infiltration.

Previous GPR studies on water movement have focused on vertical water flow because in a flat area vertical flow can create more dielectric contrast to the surrounding media than lateral flow and thus cause GPR amplitude to increase more significantly. Trinks et al. (2001) used time-lapsed GPR to study water infiltration in a sand tank and by comparing radargrams before and after infiltration they showed increased reflection below infiltration intake area due to vertical water migration. Freeland and Odhiambo (2006) used reflection patterns from GPR data to identify vertical preferential flow between loess-covered layer and clay layer in a cropland. In their study, some sections of GPR data showed columnar patterns around alluvium sand interface, which was associated with vertical preferential flow path. Truss et al. (2007) used densely sampled and precisely repeated GPR surveys to track vertical water movement in a karstic dissolution hole. Their results showed the process of how ponded water moved downward along the boundary of sand-filled dissolution hole. Saintenoy et al. (2008) also used time-lapsed GPR to monitor water infiltration through a borehole and used the simulated GPR data to explain reflections caused by the wetting front and the formation of saturation zone.

Studies on hillslope lateral flow using GPR have been limited (Ronald et al., 2001; Holden et al., 2004). The challenge may lie in whether lateral flow can create enough contrast that can be detected by GPR. At the hillslope scale, lateral flow may be caused by a number of factors, such as (1) the existence of a relatively impermeable layer of soil or bedrock (Freer, et al., 1997; Gish et al., 2002), (2) soil layering with contracting textures (Zhu and Lin, 2009), (3) connected macropore system under wet condition (Noguchi et al. 1999; Sidle et al, 2001), and (4) soil pipes created by shrinkage and desiccation cracks, animal burrows, and tree roots (Holden et al, 2004; Markus and MacDonnell, 2007) . Ronald et al. (2001) found a restricting soil layers with distinctly different dielectric properties, which impede vertical flow of water and have a significant influence on the lateral flow in the vadose zone. Holden et al. (2004) used GPR in conjunction with tracer to detect soil pipes (with diameter from 15 to 28 cm) and showed that the

method could help establish hydrological connectivity of soil pipes within a complex subsurface drainage network.

The objectives of this study were to (1) investigate the feasibility of using time-lapsed GPR to detect subsurface lateral flow in two contrasting types of soils and hillslopes within a small forested catchment, and (2) test the use of four conceptual models of flow processes in simulating and interpreting observed GPR radargrams. We simultaneously used soil moisture sensors at different depths to monitor real-time soil moisture content change during infiltration experiments and we repeated GPR scans before and after water infiltration to detect flow pathways.

## **Material and methods**

### **Study area and soils**

This study was conducted in the Shale Hills Critical Zone Observatory located in central Pennsylvania (Figure 4-1), which is a small (7.9-ha) forested catchment. We selected two hillslope transects with contrasting soils to compare infiltration processes and subsurface flow pathways (Figure 4-1). The first transect was located in the middle of a concave hillslope (swale), with the soil identified as the Rushtown series (*loamy-skeletal over fragmental, mixed, mesic Typic Dystrachrepts*). These are deep soils with > 2 m depth to bedrock and local slope of about 15%. The second transect was located in the middle of a planner hillslope, with the soil identified as the Weikert series (*loamy-skeletal, mixed, active, mesic Lithic Dystrudepts*). These are shallow soils with depth to bedrock less than 0.5 m and local slope of about 30%, which are expected to facilitate subsurface lateral flow. Table 4-1 lists the basic features of these two soils. Additional details about the soils studied can be found in Lin et al. (2006).

## Instruments

The TerraSIR Subsurface Interface Radar (SIR) System-3000 (Geophysical Survey Systems, Inc., Salem, New Hampshire) with a 400-MHz antenna (30.5 cm by 30.5 cm squared size) was used in this study. The 400-MHz was chosen after our in situ testing with a series of antenna frequencies (ranging from 200 to 900 MHz). The 400-MHz frequency provided the optimal balance of image quality and convenience of operation given the site conditions. All GPR data collected were processed using the GPR-SLICE version 6.0 software (Geophysical Archaeometry Laboratory, Woodland Hills, California). Basic data processing steps included: (1) drift removal of direct current voltage to remove signal drift from zero value; (2) zero time adjustment to find the true ground surface reflection, (3) terrain corrections to reflect topographical change through in situ elevation survey, and (4) image subtractions to obtain differential GPR images highlighting the changes between time-lapse GPR images.

At the same time when we conducted GPR scanning, soil water content was monitored in real time using the ECH<sub>2</sub>O-TE soil moisture probes (Decagon Devices, Inc., Pullman, Washington) at 2-minutes interval, which were connected to a CR1000 datalogger (Campbell Inc., Logan, Utah). An array of probes was used at different depths throughout each infiltration experiment (Figures 4-2 and 4-3). The experimental setup is detailed in the next section. Figure 4-4 shows an example of the general characteristics of the wetting and draining processes recorded at different depths in the Rushtown soil transect. From these real time soil water content change, we calculated the following parameters (Figure 4-4): 1) recharge time ( $\Delta T_r$ ) is the time that it takes for initial soil water content  $\theta_{ini}$  to reach a maximum value  $\theta_{max}$ ; 2) drainage time ( $\Delta T_d$ ) is the time it takes for the maximum water content  $\theta_{max}$  to drain to a flat drainage water content  $\theta_d$  (at the end of soil water monitoring in our case); and 3) recharge flux ( $F_r$ ) and drainage flux ( $F_d$ ) are determined by the soil water content change during these time periods (Figure 4-4).

### **Experimental setup and time-lapse GPR survey**

For the Rushtown soil transect in the swale, a 3-m survey line was established perpendicular to the downslope direction (Figure 4-2). For accurate repeatability of survey locations, GPR were scanned along a fixed rope that was anchored at the starting and ending points of the marked survey line. The distance between the survey line and a soil pit where moisture probes were installed was 30-cm. An infiltration area was located upslope 30-cm away from the GPR traverse line. A total of 20 liters of tap water was slowly and evenly poured onto the ground surface within a square area of about 25 cm by 25 cm in about 4 minutes, during which time period no overland flow occurred. Nine ECH<sub>2</sub>O-TE probes were installed at depths from 10 cm to 90 cm in the soil pit (Figure 4-2), where probes #3 and #4 were installed parallel to probe #2 (as replicates) at a 15-cm interval. The other six probes were installed at the middle of the soil profile at a 10-cm depth interval from 10 to 50 cm and then from 80 to 90 cm depths (Figure 4-2). Radar traverses were recorded on May 1, 2008 (wet season) at the following time sequence: (1) immediately before water infiltration, (2) immediately after pouring water, (3) 15 minutes after pouring water, and (4) 30 minutes after pouring water.

For the Weikert soil transect in the planar hillslope, a 3-m survey line was established along a downslope direction to track the downslope flow (Figure 4-3). Similarly, GPR were scanned along a fixed rope that was anchored at the starting and ending points of the marked survey line. A metallic plate with a diameter of 20-cm was buried at a depth of 22 cm (the top of the plate) and was located at 1.25-m downslope away from the infiltration intake area along the traverse line (Figure 4-3). The metallic plate was rested directly on top of the underlying shale bedrock. Nine ECH<sub>2</sub>O-TE soil moisture probes were installed near the end of the established traverse line (2 m downslope from the infiltration intake area). The probes were installed at depths of 5, 10, and 20 cm to correspond to A, Bw, and C horizons of the soil being investigated (Figure 4-3). Three replicated probes at each depth allowed the improved capture of flow

variability, which could help identify preferential flow. A total of 12 liters of water was slowly and evenly poured onto the soil surface in a square area about 25 cm by 25 cm located at 0.9-m on the traverse line (Figure 4-3). The water pouring lasted about 5 minutes and no overland flow was observed. Radar traverses were recorded on March 20, 2008 (wet season) at the following time sequence: (1) immediately before any water infiltration, (2) immediately after pouring water, (3) 15 minutes after pouring water, and (4) 30 minutes after pouring water.

### **Simulation of GPR radargram using different flow models**

A finite-difference time-domain (FDTD) electromagnetic modeling tool, GprMax 2.0 (Giannopoulos, 2005), was used to simulate the changes in radargram induced by different flow processes, which were compared with real radargrams obtained from the field infiltration experiments. For the simulation of different flow processes, we constructed a 3-m by 1.35-m and 3-m by 1-m domains for indicating the infiltration area and flow dynamics in the Rushtown and the Weikert soil transects, respectively, which were similar to our field GPR layouts (Figures 4-5 and 4-6). The dielectric constant ( $\epsilon$ ) of background soil were set to 13 in all simulations in the Weikert soil, with a corresponding soil water content of  $0.24 \text{ m}^3/\text{m}^3$  using the Topp equation (Topp et al., 1980) to approximate our initial experimental condition:

$$\theta = -5.3 \times 10^{-2} + 2.92 \times 10^{-2} \epsilon - 5.5 \times 10^{-4} \epsilon^2 + 4.3 \times 10^{-6} \epsilon^3 \quad [1]$$

In the Rushtown soil, the dielectric constant  $\epsilon$  of background soil was set to 16, with corresponding soil water content of  $0.29 \text{ m}^3/\text{m}^3$  (slight wetter initial moisture condition than that in the Weikert soil). In all simulations, the source wave was Ricker wavelet (a standard wave for simulation) centered on 400-MHz. Top 0.05 m was considered free space to indicate air-ground interface and the cell size was set to 0.01 m. Thus, computation time step was set to  $\Delta t = l/(c \sqrt{2})$  or 0.02357 ns to keep the numerical stability according to Giannopoulos (2005).

For the velocity of GPR wave in the Rushtown transect, we used the following equation to determine the velocity of wave propagation  $v$ :

$$v = \frac{c}{\sqrt{\varepsilon}}, \quad [2]$$

where  $c$  is wave velocity in free space and  $\varepsilon$  is corresponding dielectric constant. The dielectric constant was estimated using equation [1] in which soil water content were measured by ECH<sub>2</sub>O-TE soil moisture probes. The final velocity used in the Rushtown transect was 0.09 m/ns.

In the Weikert transect, since we knew the depth of buried metal plate, velocity  $v$  was determined based on the travel time to the depth of buried plate using the equation

$$v = \frac{2d}{t}, \quad [3]$$

where  $t$  is two way travel time of the apex of hyperbola recorded in the GPR, and  $d$  is depth of buried plate (22 cm). The final velocity used in this transect was 0.1 m/ns.

To better explain the flow processes and pathways observed under the GPR scans, we used four conceptual models of water flow to simulate GPR radargrams. The four conceptual flow models were (1) vertical matrix flow, (2) vertical macropore flow, (3) lateral matrix flow, and (4) lateral macropore flow (Figures 4-5 and 4-6). Each of these four models is described in the following:

(1) In the vertical matrix model, infiltrating water only moves vertically and no lateral flow occurs. This model assumes that the driving force for water movement is downward hydraulic gradient in the soil matrix. We created saturated zone and wetting zone to show water change after infiltration and to indicate water flow processes by adjusting the depth of saturated

and wetting zones. Figure 4-5A and 4-6A illustrate the model geometry for the Rushtown and the Weikert transects, respectively. The flow processes after infiltration are indicated by the depth and length of saturated and wetting zones. For example, immediately after infiltration was stopped in the Weikert soil, there was a 0.2-m saturation zone and a 0.1-m wetting zone beneath the infiltration intake area (Figure 4-6A). Fifteen minutes later, the saturation zone became wetting zone and the wetting zone was further down to 0.5-m to reflect no additional water coming from the surface. Thirty minutes later, wetting zone reached 0.6-m depth to reflect deep infiltration of water. The dielectric constants for the saturated zone and wetting zone were set to 30 and 20, respectively, for all our simulations. These two dielectric constants corresponded to soil water contents of 0.44 and 0.34  $\text{m}^3/\text{m}^3$ , respectively, according to Eq. 1. These two values are selected to reflect soil water content at saturation and after drainage. Note our approach here is not to precisely simulate water distribution in the soil, rather to conceptually describe the general pattern involved in water movement.

(2) In the vertical macropore model (Figures 4-5B and 4-6B), infiltrating water also moves vertically and no lateral flow occurs. This model assumes that water will not move uniformly but rapidly through “preferential” paths of macropores. We used the small cylinders with a diameter of 0.02-m to indicate locally increased soil water content due to macropores. This size compromises the sampling volume of probe and detecting range of GPR. Our preliminary simulation indicated that if size is below 0.01 m, the reflection of simulated GPR will be small (results not shown). Sakaki et al. (2008) reported that sampling volume of the EC-5 probe was approximately 2 cm (parallel to prongs) by 1 cm (perpendicular to prongs) by 9 cm (longitudinal including sensor head). The ECH<sub>2</sub>O-TE probe has similar size as EC-5 probe except that it has three prongs (instead of two prongs of EC-5 probe). We use dielectric constant of 55 and 20 to indicate maximum water content and water content after drainage, respectively, which was observed in the real time monitoring. The corresponding soil water content was 0.6

and  $0.34 \text{ m}^3/\text{m}^3$ , respectively, according to Eq. 1. Figure 4-5B and 4-6B illustrate the model geometry for such GPR simulations.

(3) In the lateral matrix flow model (Figure 4-6C), infiltrating water moves mainly laterally through top soil layers. This model assumes that top soil layer is more permeable than the soil underneath (which retards vertical flow). With certain slope gradient, lateral flow gradient exists to drive water moving through the top permeable soil layer rapidly. The results of such flow will create clear boundary between permeable and impermeable layers. This conceptual model is similar to vertical matrix model except that water will move laterally due to existence of impermeable layer and downslope gradient. So we adjusted the length of saturated and wetting zones along slope to indicate lateral flow. Figure 4-6C illustrates the model geometry for these GPR simulations.

(4) In the lateral macropore flow model (Figure 4-6D), water moves mainly laterally through macropore system rather than the soil matrix. Because of heterogeneous distribution of macropores, the flow can't create clear boundary between the dry and wet soils. Water moves through connected macropores and creates local saturation instead. So we use the similar concept as vertical macropore model except that water moves laterally. Figure 4-6D illustrates the model geometry for such GPR simulations.

## **Results and discussion**

### **Soil water content changes and GPR radargrams in the Rushtown soil transect**

#### **Soil water content change**

The soil water content responses during and after the infiltration in the Rushtown soil are plotted in Figure 4-4. The #1 probe at 10-cm depth showed a significant spike four minutes after water infiltration, reaching a volumetric soil water content 2.75 times higher than the initial water content. Within two minutes after reaching the maximum value, soil water content dropped fast, and then gradually drained to about  $0.4 \text{ m}^3/\text{m}^3$ . Since this probe was 0.9-m away from the

infiltration area, this obvious quick jump and drop in soil water content indicated a subsurface preferential flow reaching this location, which might have been caused by macrospores along the adjacent tree roots (Figure 4-2B). We in fact visually observed water dripping out of one nearby decayed root channel during the experiment, but most decayed root channels and living roots did not have any water seepage. Other soil moisture probes did not show such a significant response to infiltration, but rather showed a gradual increase in soil water content with a much lower magnitude of increase. This smaller and slower increase may be attributed to vertical and/or lateral matrix flow. Interestingly, three replicate probes at the 20-cm depth showed different response patterns, indicating flow heterogeneity. For example, the probe at the left side (probe #3) showed a small increase in soil water content while probes at the middle and right side (probes #2 and #4) showed a much higher increase. However, probe #2 clearly showed that drainage occurred within two minutes of reaching the highest moisture content, while the other two probes at the same depth showed slow continued increase in soil water content. Note that the probes below 40-cm depth (probes at 50 to 90 cm depths) showed very small responses to the infiltration, implying that little water had percolated deep enough and/or traveled long enough distance to reach the deeper probes during the 30-minute experimental time. Table 4-2 summarizes the general characteristics of the wetting and draining patterns observed with each probe. The general trend is that recharge flux, drainage flux, and percent soil water content increase all decreased with depth. Most water content increase was detected at above 40 cm soil depth, although 1.7-4.5% volumetric water content increase was also detected at 50-90 cm depths. Compared with the total amount of infiltrated water during the experiment (20 L), the soil water content increase at the location 0.9-m away from the infiltrated area was small, which indicated that much of the infiltrated water likely moved down vertically and did not reach the locations where the probes were located.

### **Field GPR radargrams**

The radargrams obtained at different times after water infiltration and their differential images (before and after infiltration) are illustrated in Figure 4-7. Before the infiltration, the radargram showed some non-continuous stripe-like pattern (illustrated in a pink dash line in Figure 4-7A), especially below 12 ns (depth about 0.60 m) of the survey line. These stripes were likely caused by the dense layer as observed in the soil pit (Figure 4-2). The discontinuous pattern of dense layer in wet season when the infiltration experiment was conducted suggests small water content difference between the layer above and below the dense layer, which caused small dielectrical contrast. This was supported by the initial soil water content recorded by the moisture probes (Table 4-2).

The most striking pattern occurred immediately after water infiltration stopped (4 minutes after infiltration started). The radargram showed strong reflections and multiple hyperbolic shapes (see the 2<sup>nd</sup> radargram in Figure 4-7A), which were likely caused by (1) local saturation near the soil surface where topography depression occurred along the survey line (a thin layer of saturated water was observed near the surface at 150 cm of the traverse line) and (2) preferential infiltration leading to point scatters of GPR reflections between dry and wet portions of the soil. This effect was also reported by Truss et al. (2007), who found irregular rock surface and tree roots caused small scale preferential flow leading to multiple hyperbolic scatterings in GPR images. In the Rushtown soil investigated here, abundant tree roots were observed at our infiltration site (Figure 4-2).

After water infiltration stopped for 15 and 30 minutes, the strong reflections decreased and the multi-hyperbolas almost disappeared (see the 3<sup>rd</sup> and 4<sup>th</sup> radargram in Figure 4-7A), suggesting fast drainage. The reduced amplitude indicated the dissipation of water at this location, which decreased the dielectrical contrast of surrounding soil with an irregular water redistribution. At this point, the overall radargram patterns were closer to that before the water infiltration

(Figure 4-7A). However, 15 and 30 minutes after the infiltration, the radar reflection amplitude still showed some increase especially near the dense layer at about 0.60-m depth (Figure 4-7). Two factors may explain the increased signal around the dense layer: (1) vertical movement of infiltrated water – This can be demonstrated by the differential GPR radargrams in Figure 4-7B, in which most of the increased amplitude only occurred around 150-cm location along the survey line while the other areas did not show increased amplitude. In addition, soil moisture probe readings also indicated that much of the infiltrated water moved vertically in this relatively gently sloping transect (15% slope) and a small depression was close the 150-cm location along the survey line; and (2) low permeability of the dense layer, which facilitated water perching and led to an increased dielectrical contrast compared to the soil above it.

Overall, both soil moisture monitoring data and the time-lapsed GPR images show that lateral flow was limited in the deep Rushtown soil transect located in the middle of the swale, instead vertical flow dominated the flow process until water reached the dense layer.

### **Soil water content changes and GPR radargrams in the Weikert soil transect**

#### **Soil water content change**

The soil moisture probes located 1.1-m downslope from the infiltration intake area showed clear responses 10-14 min after the start of the infiltration (Figure 4-8). The top soil generally showed an earlier and higher rise and drop than the deeper soils. For the three replicated probes at 5-cm depth, soil moisture displayed a sharp increase (23-123% increase at the peak compared to the initial moisture content) only 10 min after the start of the infiltration; whereas at 10-cm depth, one probe (#5) responded 10 min after the start of the infiltration and the other two probes (#4 and #6) responded 12 min after, with 78 -199% water content increase. In contrast, the probes at 20-cm depth showed a more graduate and a lower magnitude (4.6-108%) increase in soil moisture content that started 10-12 min after the start of the infiltration, except for one probe

(#7) showing little response throughout the experiment (only 4.6% increase in moisture content compared to its initial state).

The response patterns and the variability among the probes clearly showed the non-uniform nature of the wetting front of the infiltrated water. Table 4-3 summarizes the general characteristics of the wetting and draining at different depths. From Table 4-3, it is obvious that even at the same depth, the wetting and draining fluxes, as well as the maximum water content reached, varied from probe to probe. Nevertheless, the general trend is that the recharge flux, drainage flux, and the percent moisture increase from the initial state to the maximum value all decreased with increasing depth, thus suggesting more active water flow through the top soils than the subsoils.

Judging from the more significant and faster increase in the soil moisture content at the top soils (5 and 10-cm depths), the flow was likely lateral preferential flow through macropore system since the source of water was only added at an upslope area 1.1-m away from the probe locations. In this forested site, there was an organic layer of 5-cm thick underlying by an A horizon with many roots (Table 4-1), which contained more macropores than the subsoil. Interestingly, although the macropore flow was obvious at the top soils, not all probes at 5- and 10-cm depths showed the same spike-like response pattern (Figure 4-8). This not only indicates the heterogeneity of the soil but also suggests the varying connectivity of macropore networks in transmitting water downslope. For example, the probes #1 and #6 displayed a particularly significant sharp response to the water infiltration, indicating possible existence of larger or more connected macropores in the flowpath.

In comparison, the slower and smaller rise and drop in soil water content at 20-cm depth after infiltration may be due to either the dominance of the matrix flow or the less amount of water reached this depth that limited the lateral preferential flow. The water arriving at this depth

where probes were located may be the result of lateral flow from the upslope area and/or vertical flow from the top soils overlying it.

### **Field GPR radargrams**

The time-lapsed radargrams before and after the infiltration in the shallow Weikert soil transect are shown in Figure 4-9, along with the image difference by subtracting the radargrams after the infiltration from that before the infiltration. Before any water was added to the soil, the radar clearly detected the buried metal plate (i.e., apex of the hyperbolic shape in the first radargram in Figure 4-9A). Note the apex was very close to the ground wave, which was due to the shallowly buried plate and the fast velocity of electromagnetic wave. However, compared to the apex, the left and right limbs did not show clear amplitude. The reason may be the heterogeneity of the soil that attenuated the reflection of the GPR signal.

Immediately after water infiltration (see the 2<sup>nd</sup> radargram in Figure 4-9A), the most noticeable change was the strong amplitude at the left limb of the hyperbola, which not only increased in intensity but also extended to the left. Such increased reflections were due to the formation of the saturated zone below the infiltration intake area (indicated by a red arrow in Figure 4-9A), because it took about five minutes to complete the water infiltration before this radargram was recorded. This saturated zone enhanced the dielectric contrast to the surrounding soil and hence increased radar amplitude. The reflections also extended toward left because the position of the saturated zone was located before the buried plate. In addition, multiple overlapped hyperbolas were observed below the buried plate. This pattern may be due to the irregular diffractions caused by heterogeneous wetting front at the interface between the initial drier soil and the wetted soil by infiltrating water. When radar wave encountered these anomalies, part of the wave would be diffracted and the overlapped hyperbola appeared. The difference between such a radargram and the radargram before the infiltration indicates the enhanced reflection at the left limb of the hyperbola (Figure 4-9B). Another noticeable change was the

two-way travel time to the apex of the hyperbola (pink dash line in Figure 4-9A). Before infiltration, the two-way travel time to the apex of the hyperbola was about 4 ns. Immediately after infiltration, this time changed to about 6 ns. This time shift indicated that the increase in water content has decreased the speed of radar electromagnetic wave.

Fifteen minutes after the infiltration, the most change observed (the 3<sup>rd</sup> radargram in Figure 4-9A) was the decrease in amplitude below the infiltration intake and the disappearance of the overlapped hyperbolas at the left limb. The decreased amplitudes suggested that water content below the infiltration intake area has decreased, which indicated that the saturated zone below the infiltration intake area has de-saturated and changed to a wetted zone instead; therefore the dielectric contrast with the surrounding soil decreased. The dissipation of water below the infiltration intake area could be due to either deep percolation into the bedrock (vertical flow) or lateral flow down the slope. From the response of the soil moisture probes downslope (which detected the increase in soil water content in 10-14 min), it could be inferred that lateral flow most likely occurred. This is also supported by the overall shift in downslope direction of radar amplitudes from the left limb to the right limb of the hyperbola (see Figure 4-7B). At this stage, multiple radar reflections were also observed below the buried plate, probably because of non-uniform distribution of water that caused multiple interfaces around the buried plate. In addition, backfilled soil around the buried plate might create irregular boundary among water, air, soil, and the plate in the subsurface. Such multiple reflections were also observed by Zeng et al. (1997) where water filled pipe was buried in the subsurface, and by Liu et al. (2007) where metal rebar used to reinforce concrete existed in air-filled and water-filled gaps between concrete and bedrock in a road construction.

Thirty minutes after the infiltration, multiple reflections still existed around the buried plate, again likely because of the heterogeneous movement of water as explained above. In addition, the radar amplitudes at the left limb of the hyperbola further decreased. This is obvious

when compared with the initial radargram before the infiltration (the 3<sup>rd</sup> radargram in Figure 4-9B). However, the decreased patterns are different from that observed in the Rushtown soil transect. This can be demonstrated by the differential radargrams of the two transects. In the Weikert transect, the differential radargram between 30 min after infiltration and before infiltration (i.e., the 3<sup>rd</sup> radargram in Figure 4-9B) show little difference below the infiltration intake, which indicated the depletion of water below the infiltration intake area. In contrast, the differential radargram in the Rushtown transect (i.e., the 3<sup>rd</sup> radargram in Figure 4-7B) still showed strong amplitudes below the depression when compared with the radargram before infiltration, which indicated the presence of water. This difference further elucidated the contrasting flow processes observed at the two infiltration sites (i.e., two soil types in different hillslopes). In the deep Rushtown soil transect, local surface topographical depression facilitated vertical percolation, while in the shallow Weikert transect, steep slope caused water to move laterally along the slope gradient and thus less water percolated vertically below the infiltration intake area.

#### **Simulated vs. observed GPR radargrams**

To help explain the observed radargrams, we simulated GPR response based on four conceptual flow models mentioned above. In the Rushtown soil transect located in the swale, we first used vertical matrix flow and vertical macropore flow models, with simulated results shown in Figure 4-10B and 4-10C. In the vertical matrix model, four minutes after infiltration, simulated results did show increased amplitude but did not show crisscross pattern observed in the field radargrams. In addition, with time lapse, the simulated results did not show decreased amplitude. The increased amplitude still existed but its position moved to a lower position. This slight difference was due to the position and length of the saturated zone and the wetting zone. Furthermore, at the boundary with the dense layer at about 0.6 m (Figure 4-2), the simulated results also did not show much enhanced amplitude.

In the vertical macropore flow model, simulated radargrams immediately after the infiltration showed multi hyperbolas, which was much closer to the observed radargrams. However, with time lapse, amplitude in simulated radargrams still increased and multi hyperbolas did not disappear. As explained before, the multi-hyperbolas are caused by irregular water distribution through preferential flow. Because of high initial water content, dielectric contrast due to water became small after drainage was completed, which caused the pattern of the observed field radargram to be close to that observed before the infiltration. However, the dense layer restricted the further deep infiltration of water and thus water perched above this layer. To reflect such flow dynamics, we introduced a mixed model by combining the vertical macropore flow and the lateral matrix flow models. Figure 4-10D illustrated the concept of such a mixed model. Immediately after the infiltration, we used the vertical macropore model; 15 min later when water perched above the dense layer, we only introduced a thin wetting zone above the dense layer; and 30 min later, we extended the lateral wetting zone, implying lateral movement of water along the dense layer. Figure 4-10D shows the simulated results from such a mixed model, which is much closer to the field GPR radargram compared to either vertical matrix model or vertical macropore model.

The simulated radargrams for the shallow Weikert transect are illustrated in Figure 4-11 to compare with the field observed radargrams. In the vertical matrix model, immediately after the infiltration, the amplitude at the left limb of hyperbola increased, which matched the field radargram. With water percolated deeper vertically, the radar pattern was similar to the simulated results using the same model for the Rushtown soil transect. The increased amplitude still existed at the left limb with only change in the position of increased amplitude. Because water only moved vertically, the amplitude still increased. However, the field radargrams showed decreased amplitude after infiltration ceased. In addition, the field radargrams also showed multiple reflections below the buried metal plate, which was caused by the heterogeneous distribution of

water content. In general, the simulated results did not show gradually decreased reflection pattern after the infiltration, which was the case in the field observed GPR images. These discrepancies indicate that infiltrating water not only moved vertically but also laterally since vertical flow only changed the depth of the saturated and wetting zones. It was the lateral flow that reduced the water content hence decreased the amplitude of the radargrams.

Similar to the vertical matrix model, the simulated results from the vertical macropore model did not show gradually decreased reflection pattern after the infiltration (Figure 4-11C), which was the case in the field observed radargrams. On the contrary, the reflection increased because of increased water content through macropore preferential pathway. With this vertical macropore model, we also did not see multiple reflections below the buried plate because this model assumed water only moved vertically.

In the lateral matrix flow model, immediately after the infiltration, reflection pattern was similar to the observed radargrams (Figure 4-11D). With time lapse, the simulated radargram showed the decreased amplitude at the left limb and increased amplitude toward the right limb. However, the simulated radargrams also showed the layer-like reflection (see the 3<sup>rd</sup> and 4<sup>th</sup> radargrams in Figure 4-11D), which was caused by the boundary of water moving through the permeable layer. But the field radargrams did not have such reflection, indicating that water did not move homogeneously through the permeable layer. In addition, because of such homogeneous lateral matrix flow, the simulated results did not show multiple reflections as observed in the field records (again, caused by heterogeneous distribution of water content).

In the lateral macropore flow model, the simulated radargrams were the closest to the observed radargrams as compared to the other three conceptual flow models (Figure 4-11E). The amplitude at the left limb decreased with time lapse, multiple overlapped hyperbolas appeared immediately after the infiltration ceased, and stacked reflection was obtained below the buried plate. Hence, this lateral macropore flow model explained reasonably the observed field

radargrams and the real-time soil moisture monitoring data. Nevertheless, there are still some subtle differences between the simulated results and the observed radargrams in Figure 4-11E. This probably has something to do with the high degree of heterogeneity in the subsurface being investigated, while the model simulations were based on homogenous porous media with macropores built in to simulate lateral macropore flow.

### **Summary and Conclusion**

Infiltration experiments conducted in two soil types from contrasting hillslopes revealed different flow processes and patterns. For the deep Rushtown soil series (> 2 m depth to bedrock) in the middle of a swale (with a slope of 15%), even though more water was infiltrated (20 L), the frequency and magnitude of lateral flow was much less obvious (with only one probe at 10-cm depth showed a spike-like soil moisture response after infiltration), indicating that vertical flow was dominated until the flow reached a dense layer. In contrast, in the shallow Weikert soil series (< 0.4 m depth to bedrock) in the middle of a planar hillslope (30% slope), although less water was added (12 L), fast rise and drop of soil water content were observed in upper 20 cm depths, indicating that lateral flow was a dominant mechanism to deliver water downslope.

Based on the real-time soil moisture monitoring and time-lapsed GPR radargrams, four conceptual models were compared to explain the complex and variable subsurface flow patterns. These models were intended to test our hypothesis about dominant flow pathways and processes in natural soils rather than to accurately predict soil moisture distribution after infiltration. The simulated radargrams in the Rushtown transect indicated that vertical matrix flow and vertical macropore flow alone could not explain well the field GPR records; instead, a combination of vertical macropore flow and lateral matrix flow better explained the flow processes that matched with observed soil profile characteristics. The simulated results in the Weikert transect, in comparison, revealed the dominance of lateral macropore flow and its spatial and temporal variability.

This study demonstrated the value of combining real-time soil moisture monitoring, time-lapsed GPR surveys, and GPR simulation modeling to reveal the complex and dynamic subsurface flow processes and their general patterns. Because of the soil heterogeneity and the small dimension of individual macropores, the macropore flow itself could not create enough contrast for clear and direct GPR detection. By using the simulated radargrams in comparison with the actual GPR data, we were able to identify likely flow processes and their effects on the GPR radargrams. Although simulated results would be hard pressed to provide a perfect match to the real-world complex subsurface flow, the overall patterns revealed by the time-lapsed GPR were meaningfully interpreted in this study. The methodology employed in this study permits an improved understanding of hydrologic connectivity in the subsurface and facilitates the formulation and test of different conceptualizations of subsurface network modeling.

### References

- Bonell, M. 1998. Selected challenges in outflow generation research in forests from the hillslope to headwater drainage basin scale, *Journal of the American Water Resources Association* 34, 765–785.
- Birken, R., Versteeg, R. 2000. Use of four-dimensional ground penetrating radar and advanced visualization methods to determine subsurface fluid migration. *Journal of Applied Geophysics* 43, 215–226.
- Daniels, J. J., R. Roberts, Vendl, M. 1995. Ground penetrating radar for the detection of liquid contaminants. *Journal of Applied Geophysics* 33, 195-207.
- Freeland, R. S., Odhiambo, L. O. 2006. Subsurface characterization using textural features extracted from GPR data. *Transactions of American Society of Agricultural and Biological Engineers* 50, 287–293.

- Freer, J., McDonnell, J. J., Beven, K. J., Brammer, D., Burns, D., Hooper, R. P., and Kendall, C. 1997. Topographic controls on subsurface storm flow at the hillslope scale for two hydrologically distinct small catchments, *Hydrological Processes* 11, 1347–1352.
- Freer, J., McDonnell, J. J., Beven, K. J. et. al. 2002. The role of bedrock topography on subsurface storm flow. *Water Resources Research* 38(12), WR000872.
- Giannopoulos, A. 2005. Modelling ground penetrating radar by GprMax. *Constr. Build. Mater.* 19, 755–762.
- Gish T. J., Dualaney W. P., Kung K.- J. S., Daughtry C. S. T., Doolittle J. A., and Miller P. T. 2002. Evaluating use of ground-penetrating radar for identifying subsurface flow. *Soil Sci. Soc. Am. J.* 66, 1620-1629.
- Hewlett, J. D., and A. R. Hibbert. 1965. Factors affecting the response of small watersheds to precipitation in humid areas, Paper Presented at International Symposium on Forest Hydrology, Pa. State Univ. University Park.
- Huisman, J. A., Hubbard, S. S., J. D. Redman, and A. P. Annan. 2003. Measuring Soil Water Content with Ground Penetrating Radar: A Review. *Vadose Zone Journal* 2, 476–491.
- Jérôme Poisson, Michel Chouteau, Michel Aubertin, Daniel Campos., 2009. Geophysical experiments to image the shallow internal structure and the moisture distribution of a mine waste rock pile. *Journal of Applied Geophysics* 67, 179–192.
- Lin, H. 2006. Temporal Stability of Soil Moisture Spatial Pattern and Subsurface Preferential Flow Pathways in the Shale Hills Catchment. *Vadose Zone Journal* 5, 317-340.
- Lin, H.S. 2010. Linking principles of soil formation and flow regimes. *Journal of Hydrology*. (In press)
- Lin, H. and Zhou X., 2008. Evidence of subsurface preferential flow using soil hydrologic monitoring in the Shale Hills catchment. *European J. Soil Sci.* 59, 34-49.

- Liu, L., He, K., Xie, X. 2007. Image enhancement with wave-equation redatuming: application to GPR data collected at public transportation sites. *J. Geophys. Eng.* 4, 139–147.
- Lunta, I.A., S.S. Hubbard, Y. Rubin. 2005. Soil moisture content estimation using ground-penetrating radar reflection data. *J. Hydrol.* 307, 254–269.
- Grasmueck, M., R. W., and Heinrich Horstmeyer. 1996. 3-D ground-penetrating radar applied to fracture imaging in gneiss. *Geophysics* 61(4), 1050-1064.
- Trinks, I., Wachsmuth, D., H. Stümpel. 2001. Monitoring water flow in the unsaturated zone using georadar. *First Break* 19, 679-684.
- Truss S., Grasmueck M., Vega S., and Viggiano D. A. 2007. Imaging rainfall drainage within the Miami oolitic limestone using high-resolution time-lapse ground-penetrating radar. *Water Resources Research* 43 , doi:10.1029/2005WR004395.
- Ronald E. Y., Freeland, R.S., Ammons, J.T. and Leonard, L., L. 2001. Mapping agricultural fields with GPR and EMI to identify offsite movement of agrochemicals. *Journal of Applied Geophysics* 47:,251-259.
- Sakaki, T., Limsuwat, A. Kathleen M., and Tissa H. 2008. Empirical two-point A-mixing model for calibrating the ECH2O EC-5 soil moisture sensor in sands. *Water Resources Research* 44, W00D08, doi:10.1029/2008WR006870.
- Sidle, R., S. Noguchi, Y. Tsuboyama, and K. Laursen. 2001. A conceptual model of preferential flow systems in forested hillslopes: evidence of self-organization. *Hydrological Processes* 15, 1675–1692.
- Saintenoy, A., Schneider, S., Tuchoka, P. 2008. Evaluating ground penetrating radar use for water infiltration monitoring. *Vadose Zone Journal* 7, 208-214.
- Todd, M.S., Jeff, P.R., George M.H. 2000. Shallow subsurface storm flow in a forested headwater catchment: Observations and modeling using a modified Topmodel. *Water Resources Research* 36(9), 2575–2586.

- Tromp-van Meerveld, H. J. and McDonnell, J. J. 2006. Threshold relations in subsurface stormflow 1. A 147 storm analysis of the Panola hillslope, *Water Resources Research* 42, W02410, doi:10.1029/2004WR003778.
- Weiler and McDonnell. 2004. Virtual experiments: a new approach for improving process conceptualization in hillslope hydrology. *J. Hydrol.* 285, 3-18.
- Weyman, D. R. 1973. Measurements of the downslope flow of water in a soil. *J. Hydrol.* 20, 267–288.
- Whipkey, R. Z. 1965. Subsurface stormflow from forested slopes. *Bull. Int. Assoc. Sci. Hydrol.* 10, 74–85.
- Zeng, X., A. McMechan., 1997. GPR characterization of buried tanks and pipes, *Geophysics* 62, 797–806.
- Zhu, Q., and H.S. Lin. 2009. Simulation and validation of concentrated subsurface lateral flow paths in an agricultural landscape. *Hydrology and Earth System Science* 13, 1503-1511.

Table 4-1: Soil profile characteristics of the two soil series investigated in this study.

Horizon	Depth (m)	Clay (%)	Silt (%)	Sand (%)	> 2mm rock fragment # (%)	Bulk density (g cm <sup>-3</sup> )	Pedality ## (structure)	Roots
<b>Weikert Series</b>								
Oe	0-0.05				22	0.425		Very many fine roots throughout
A	0.05-0.12	30.4	56.4	13.2	29	0.960	2 f gr	Very many fine roots throughout
Bw	0.12-0.22	26.3	54.5	19.2	20	1.260	2 f sbk	Common fine roots in cracks
CR	0.22-0.37				90		1 f sbk	Few fine roots in cracks
R	0.37*							
<b>Rushtown Series</b>								
Oe	0-0.05				11	0.425		Very many fine roots throughout
A	0.05-0.11	31.8	53.8	14.4	34	1.807	3 f gr	Very many fine roots throughout
Bw1	0.11-0.17	30.9	51.5	17.6	39	1.204	2 f sbk	Many fine roots throughout
Bw2	0.17-0.26	29.7	53.4	16.9	28	1.292	1 m sbk	Common fine roots throughout
Bw3	0.26-0.38	31.1	52.1	16.8	29	1.537	1 m sbk	Common fine to coarse roots throughout
BC	0.38-0.60	31.6	50.1	18.3	38	1.637	massive	Few medium roots throughout
C	0.60**-1.78	25.5	28.7	45.8	60	1.652	massive	

\* indicate depth where rock starts

\*\* indicate depth where dense layer starts

# Rock fragments are all shale channers of 2-150 mm thick, many are soft or very soft

### Pedality is described using ped grade, ped size, and ped shape. 1, 2, 3 for weak, moderate, and strong ped grade, respectively; vf, f, m, and c for very fine, fine, medium, and coarse ped size, respectively; gr, sbk for granular, and subangular blocky ped shape, respectively. Massive means not soil structure developed.

Table 4-2 : Summary of soil moisture sensor responses at different depths during the infiltration experiment in the Rushtown soil transect.

Sensor # (depth in cm)	Initial soil water content(m <sup>3</sup> /m <sup>3</sup> )	Max. soil water content <sup>a</sup> (m <sup>3</sup> /m <sup>3</sup> )	Drainage Water content <sup>b</sup> (m <sup>3</sup> /m <sup>3</sup> )	Recharge flux <sup>e</sup> (m <sup>3</sup> /m <sup>3</sup> /min)	Drainage flux <sup>f</sup> (m <sup>3</sup> /m <sup>3</sup> /min)	Recharge time <sup>c</sup> (min)	Drainage time <sup>d</sup> (min)	Percent increase between initial and max. Water content (%)
1 (10)	0.280	0.771	0.422	0.1228	0.0097	4	36	175.4
2 (20)	0.254	0.335	0.314	0.0135	0.0007	6	32	31.9
3 (20)	0.231	0.244	0.244	0.0003	n	40	n	5.6
4 (20)	0.292	0.333	0.332	0.0010	n	40	n	14.0
5 (30)	0.283	0.352	0.350	0.0022	0.0003	32	8	24.4
6 (40)	0.262	0.282	0.282	0.0005	n	40	n	7.6
7 (50)	0.242	0.246	0.247	n	n	n	n	1.7
8 (80)	0.284	0.289	0.287	n	n	n	n	1.8
9 (90)	0.155	0.162	0.162	0.0002	n	40	n	4.5

<sup>a</sup> Max. Water content: the highest soil water content during infiltration experiment

<sup>b</sup> Drainage water content: drained soil water content with its change less than 0.2 % compared to that at the end of the experiment

<sup>c</sup> Recharge time: time to reach the highest soil water content during infiltration

<sup>d</sup> Drainage time: time for soil water content to drop from the highest value to drainage water content

<sup>e</sup> Recharge flux: the difference between the max. water content and initial water content divided by the recharge time

<sup>f</sup> Drainage flux : the difference between the max. water content and drainage water content divided by the drainage time

n means not applicable.

Table 4-3 : Summary of soil moisture sensor responses at different depths during the infiltration experiment in the Weikert soil transect.

Sensor #	Initial soil water content(m <sup>3</sup> /m <sup>3</sup> )	Max. soil water content <sup>a</sup> (m <sup>3</sup> /m <sup>3</sup> )	Drainage water content <sup>b</sup> (m <sup>3</sup> /m <sup>3</sup> )	Recharge flux <sup>e</sup> (m <sup>3</sup> /m <sup>3</sup> /min)	Drainage flux <sup>f</sup> (m <sup>3</sup> /m <sup>3</sup> /min)	Recharge time <sup>c</sup> (min)	Drainage time <sup>d</sup> (min)	Percent increase between initial and max. Water content (%)
<b>5 cm depth</b>								
1	0.283	0.620	0.316	0.169	0.0138	2	22	119.1
2	0.475	0.585	0.541	0.028	0.0024	4	18	23.2
3	0.293	0.491	0.393	0.050	0.0049	4	20	67.6
<b>10 cm depth</b>								
4	0.251	0.449	0.359	0.099	0.0045	2	20	78.9
5	0.202	0.494	0.326	0.073	0.0076	4	22	144.6
6	0.206	0.617	0.332	0.206	0.0157	2	18	199.5
<b>20 cm depth</b>								
7	0.369	0.386	0.385	0.001	0.0001	16	18	4.6
8	0.123	0.256	0.208	0.033	0.0027	4	18	108.1
9	0.240	0.433	0.375	0.048	0.0032	4	18	80.4

<sup>a</sup> Max. water content: the highest soil water content during infiltration experiment

<sup>b</sup> Drainage water content: drained soil water content with its change less than 0.2 % compared to that at the end of the experiment

<sup>c</sup> Recharge time: time to reach the highest soil water content during infiltration

<sup>d</sup> Drainage time: time for soil water content to drop from the highest value to drainage water content

<sup>e</sup> Recharge flux: the difference between the max. water content and initial water content divided by the recharge time

<sup>f</sup> Drainage flux : the difference between the max. water content and drainage water content divided by the drainage time

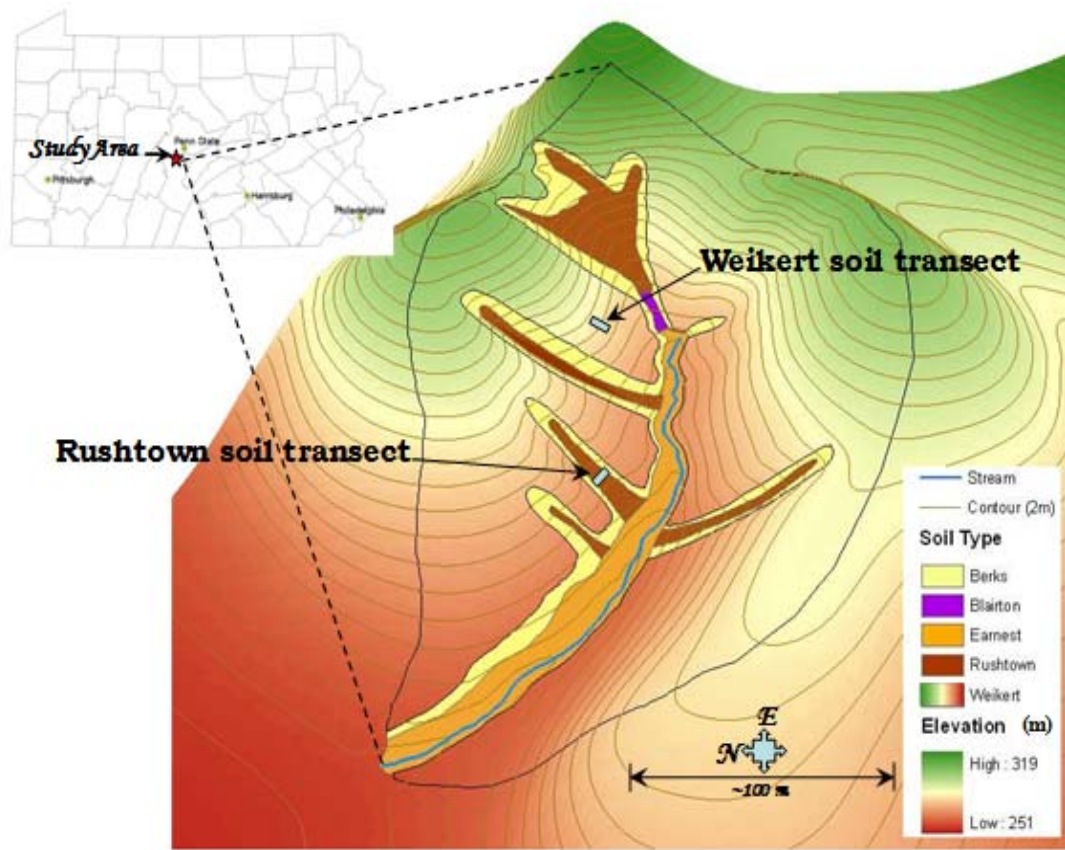


Figure 4- 1: An overview of the Shale Hills Critical Zone Observatory and the locations of two types of soils and hill slopes investigated

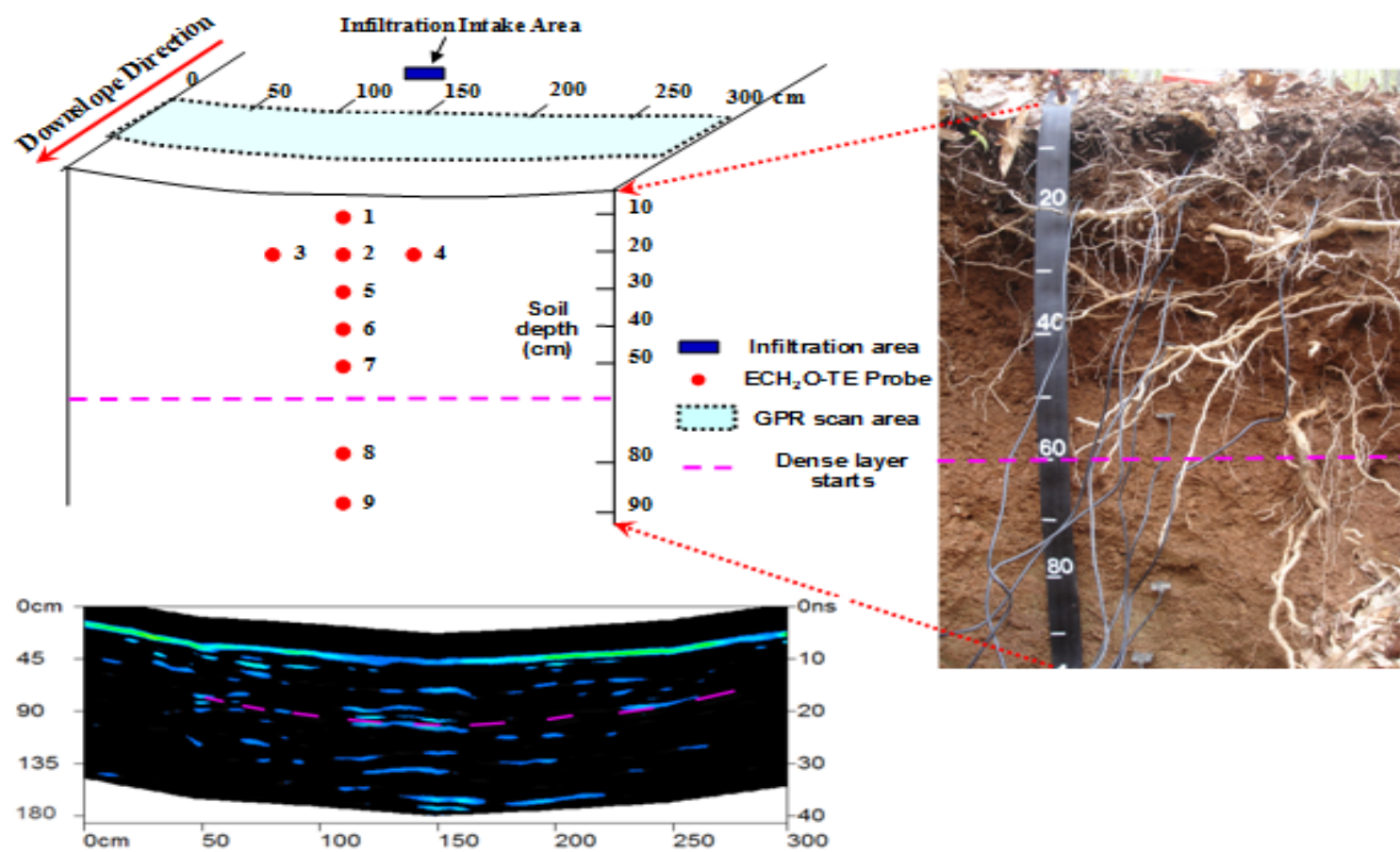


Figure 4- 2: Schematic of infiltration experiment setup in the concave (swale) hillslope with the Rushtown soil series and a downslope gradient of 15%. Photograph of soil pit shows protrude tree roots and a dense layer (pink dash line). Topography-corrected radargram

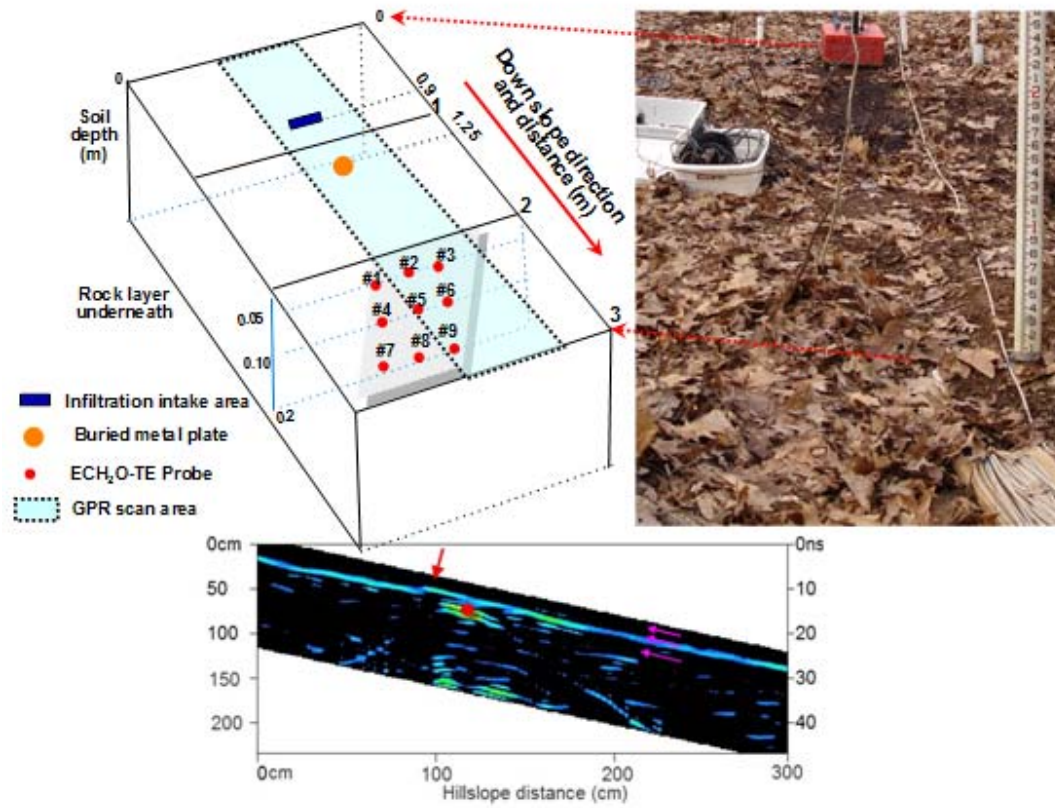


Figure 4- 3: Schematic of infiltration experiment setup in the planar hillslope with the shallow Weikert soil series and a downslope gradient of 30%. Topography-corrected radargram at the initial state before infiltration shows the slope gradient, infiltration intake

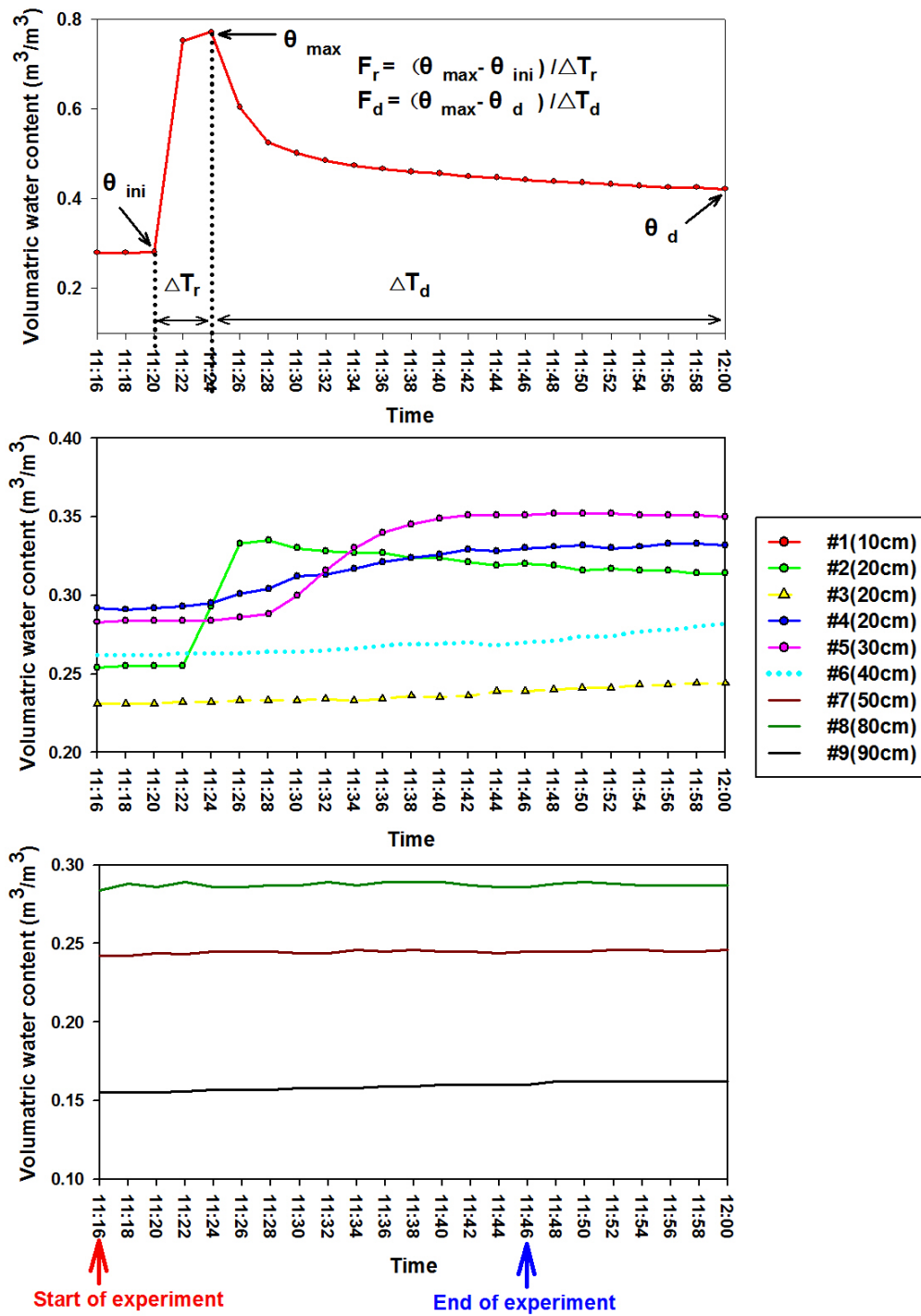


Figure 4- 4: Time series of soil moisture readings at different depths during the infiltration experiment in the Rushtown soil transect. Red arrow indicates the beginning of water infiltration and dark blue arrow indicates the end of the infiltration experiment. The top panel illustrates several wetting and draining parameters used in this study.

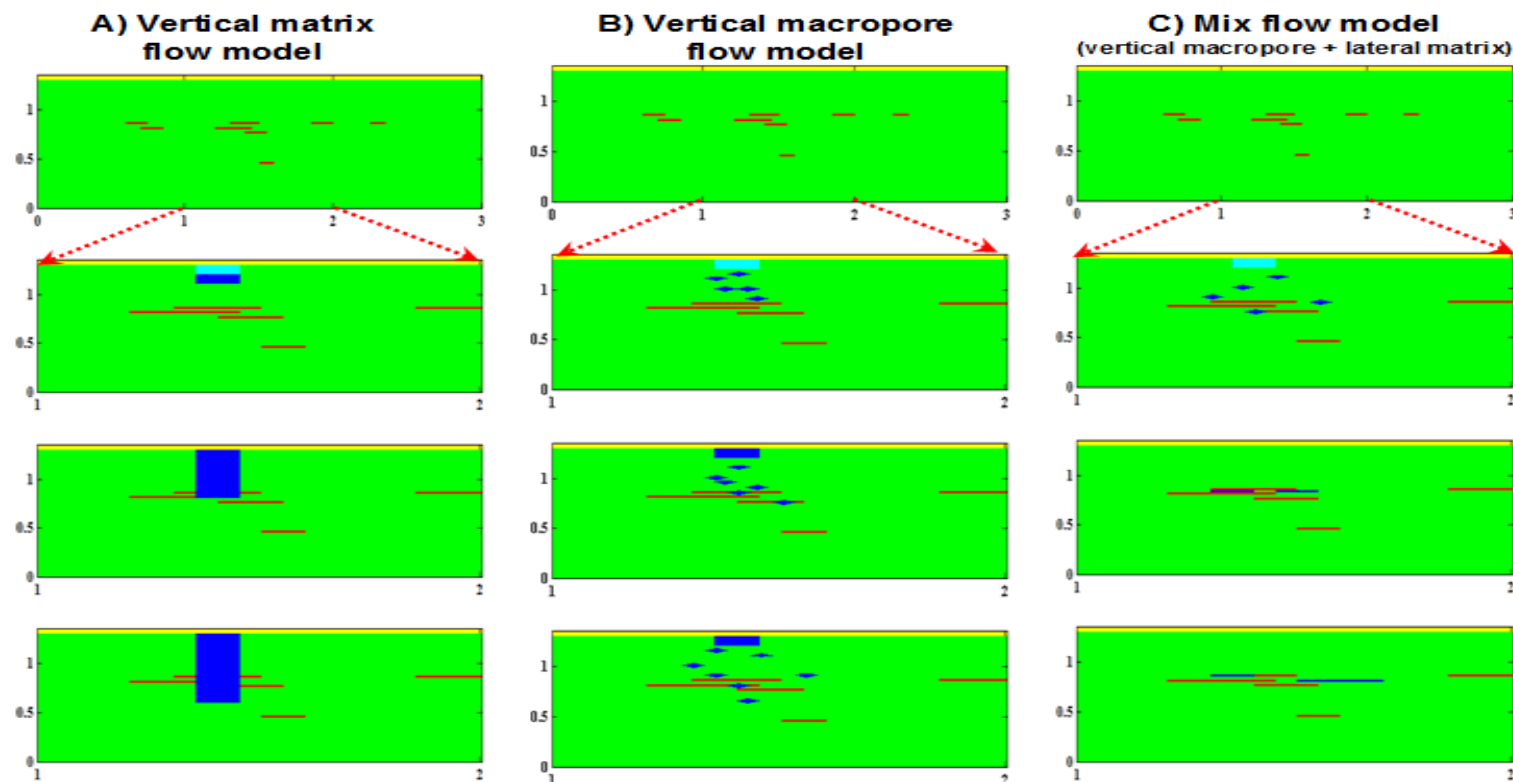


Figure 4- 5: Geometry of GPR simulations using different conceptual flow models for the Rushtown soil transect: A) Vertical matrix flow model; B) Vertical macropore flow model; and C) Combination of vertical macropore flow model and lateral matrix flow model. Conceptual flow processes after infiltration ceases is indicated from top to bottom to represent water distribution in 4, 15 and 30 minutes after infiltration, respectively. Yellow areas indicate air, green areas indicate background soil with  $\epsilon=13$ , red lines indicate restricting layer with  $\epsilon=16$ , blue lines indicate increased soil water content with  $\epsilon=20$  due to perched water, light blue and dark blue boxes indicate saturated zone and wetting zone with  $\epsilon=30$  and  $\epsilon=20$ , respectively, and blue dots indicate local increased soil water content caused by preferential flow with  $\epsilon=20$ . Note that for the initial condition the whole geometry is shown in all the models, but for the subsequent conditions after infiltration, only the zoom-in portion from 1 to 2 m of the survey line is shown

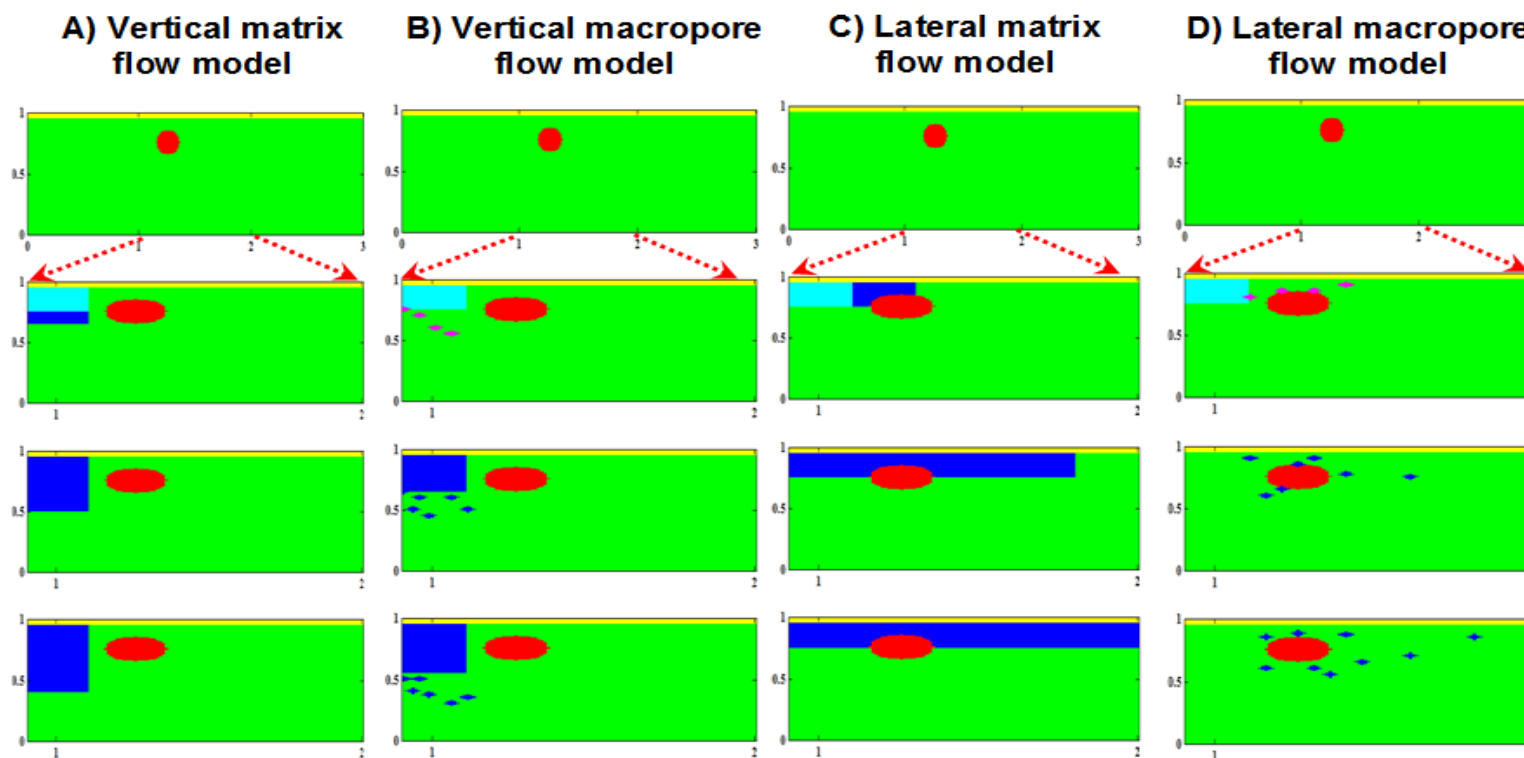


Figure 4- 6: Geometry of GPR simulations using different conceptual flow models for the Weikert soil transect: A) Vertical matrix flow model; B) Vertical macropore flow model; C) Lateral matrix flow model; and D) Lateral macropore flow model. Conceptual flow processes after infiltration ceases is indicated from top to bottom to represent water distribution in 5, 15, and 30 minutes after infiltration, respectively. Yellow areas indicate air, green areas indicate background soil with  $\varepsilon=13$ , red circles indicate the buried plate, light blue and dark blue boxes indicate saturated zone and wetting zone with  $\varepsilon=30$  and  $\varepsilon=20$ , respectively, and pink and blue dots indicate local increased soil water content caused by preferential flow with  $\varepsilon=55$  and  $\varepsilon=20$ , respectively. Note that for the initial condition the whole geometry is shown in all the models, but for the subsequent conditions after infiltration, only the zoom-in portion from 0.9 to 2 m of the survey line is shown.

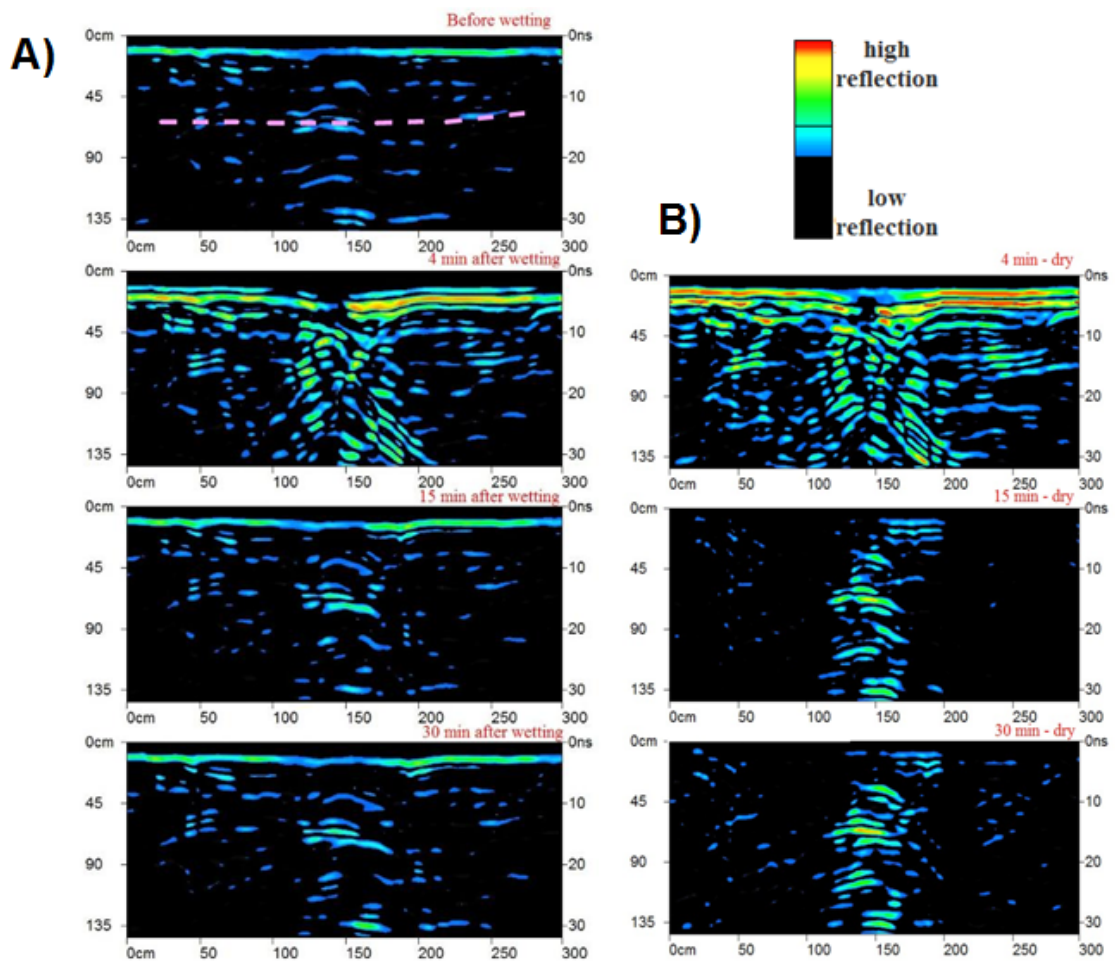


Figure 4- 7: A) Time-lapsed GPR images before and after the infiltration in the Rushtown soil transect. B) Differential radargrams between 4, 15, or 30 min after the infiltration, respectively, and that of initial condition before infiltration. Depth is converted using velocity of 0.09 m/ns.

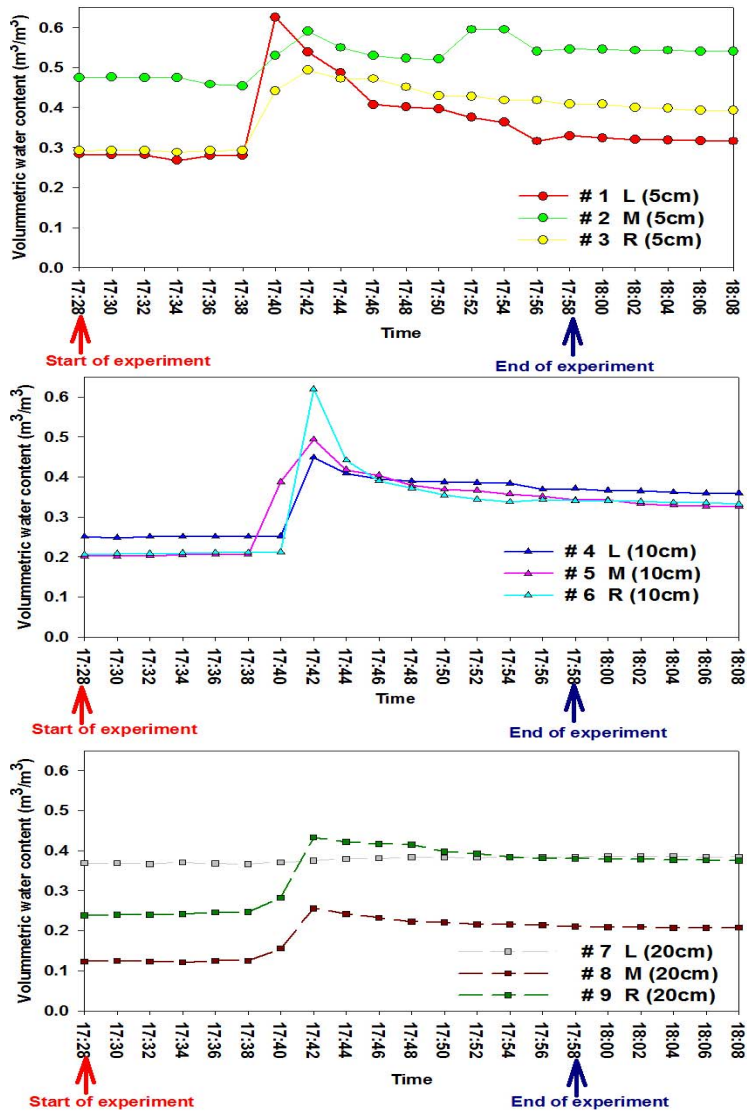


Figure 4- 8: Time series of soil moisture readings at different depths during the infiltration experiment in the Weikert soil transect. Red arrow indicates the beginning of water infiltration and dark blue arrow indicates the end of the infiltration experiment.

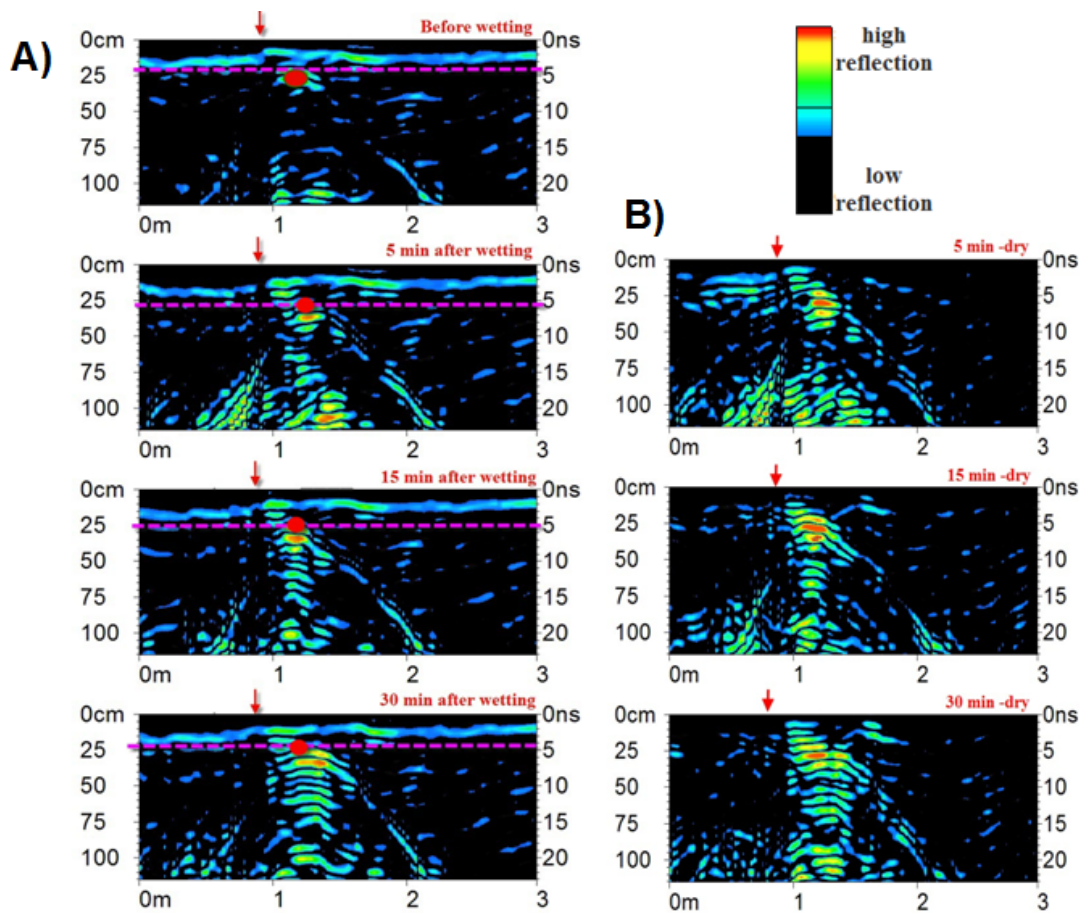


Figure 4- 9: A) Time lapse GPR images before and after the infiltration in the Weikert soil transect. Red arrow indicates the location of the infiltration intake area. Pink dash line is the two way travel time to the apex of hyperbola and red dot indicates the location of the buried metal plate. B) Differential radargrams between 5, 15, or 30 min after the infiltration, respectively, and that of initial condition before infiltration.



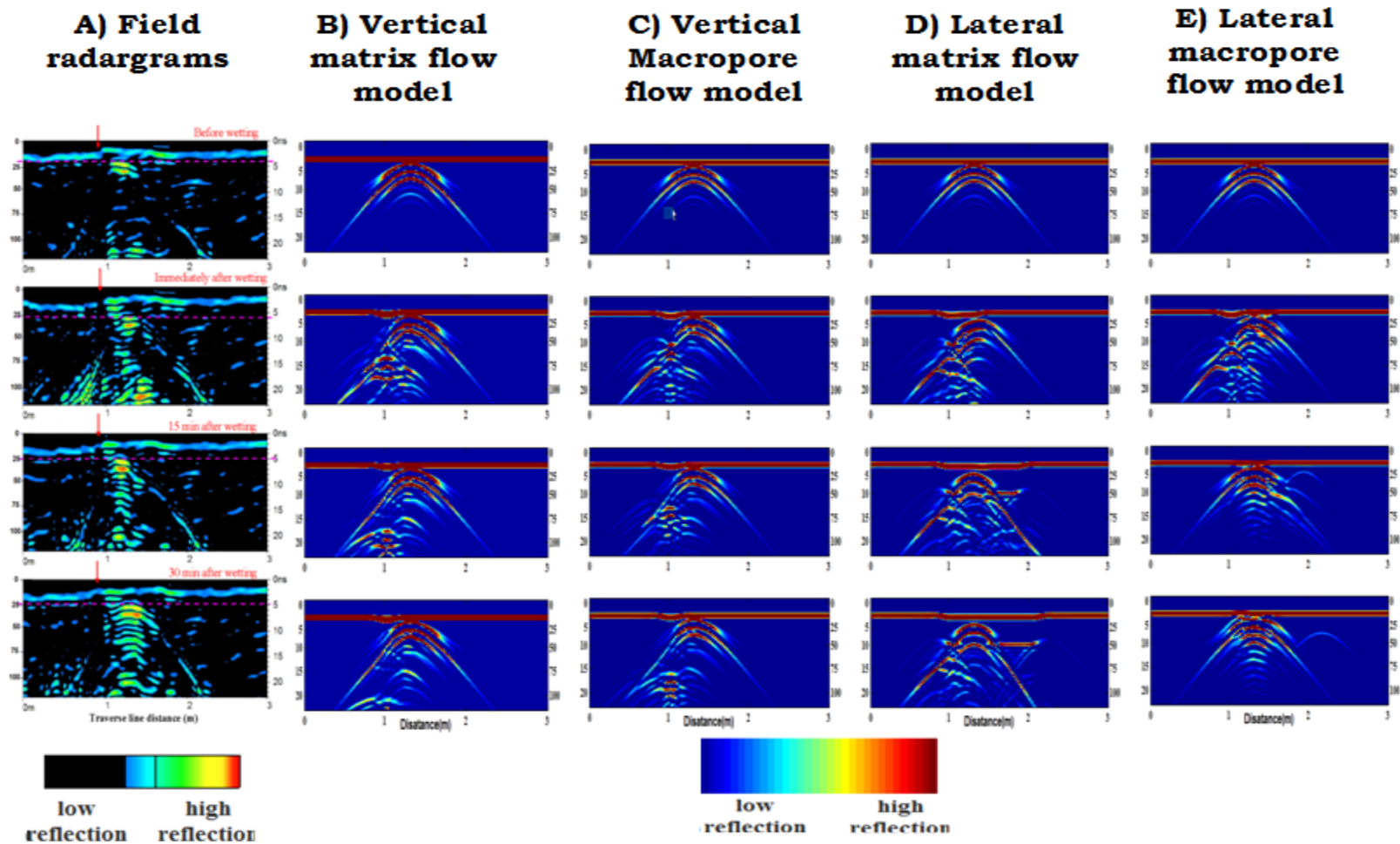


Figure 4- 11: Simulated GPR radargrams for the Weikert soil transect using four conceptual flow models and their comparisons to the real GPR radargrams.

## **Chapter 5**

### **Seasonal GPR Signal Changes in Two Soils and Hillslopes**

#### **Abstract**

Experimental evidence has shown that soil layering can significantly affect water movement. So detailed knowledge of the spatial distribution of soil layering structures are needed when estimating subsurface soil water movement. In this study, we used GPR combined with high resolution real time soil water content monitoring to compare the seasonal GPR signal changes at the interfaces of soil layers in two soils. The results indicate that in deep Rushtown soil, reflection in BC-C horizon became clearer as soil became wetter. High resolution real time soil water content monitoring and field observation indicate the increased reflection may be due to the lateral flow above and below BC horizon, which increase the contrast along interfaces. While in shallow Weikert soil, reflections in soil -bedrock interface and weathered-unweathered rock interface become intermittent as soil became wetter. The reason was likely to be non uniform distribution of water into bedrock fracture, which created locally strong contrast between soil and bedrock leading to point scatter of GPR reflection. The results also indicate optimal time to detect soil horizon in two soils. In addition, the results also indicate seasonal GPR survey with high resolution real time soil water content monitoring provided a useful methodology for improved understanding of hydrologic processes in the subsurface, which facilitates the formulation and test of different conceptualizations of subsurface network modeling.

## Introduction

Rainfall-induced subsurface water movement at the hillslope scale is an important process that contributes substantially to runoff (Hewlett and Hibbert, 1965; Whipkey, 1965; Weyman, 1973, Bonell, 1998, Kienzler and Naef, 2008). Among many factors that influence subsurface water movement, soil layering has significant impacts because significant changes in texture or density across the boundary of two adjacent layers could noticeably alter water distribution. For instance, Brown et al. (1999) found rapid delivery of water through O-horizon to stream during summer rainstorms through tracer experiment. By using crest piezometers along slope, Todd et al. (2000) identified the formation of perched water table at the clay rich B horizon during rainfall events and their results indicated the transient perched water table leading to saturated downslope flow through the more permeable upper soil layer. Lin and Zhou (2008) found bypass flow to the bedrock from the overlying shallow soil during dry season. Many researchers (Freer, et al., 1997, Weiler and McDonnell, 2004; Tromp-van Meerveld and McDonnell, 2006) have observed rapid lateral flow at the soil–bedrock interface. Consequently, detailed knowledge of the spatial distribution of soil layering structures are needed when estimating subsurface soil water movement. However, traditional methods have largely been destructive and/or based on point measurement, which is labor intensive and lack of spatial resolution.

GPR is a high-resolution geophysical technique that utilizes the transmission and reflection of high frequency (10–1200 MHz) electromagnetic waves. Application of GPR relies on contrasting electrical impedance of the media being investigated, which is primarily determined by dielectric and conductive properties of the material, its magnetic permeability, and its physical properties (Daniels, 2004). For most of natural soils, water content change is a main factor impacting GPR reflection because the dielectric constant of water is about 80 while that of dry soil is between 3 and 5 (Gish et al., 2002). Such a contrast between water and surrounding

drier soils make it possible to detect the seasonal signal change at the interface of different soil layers since water has different distribution pattern along the interface.

GPR has been widely used to detect soil horizons. Gish et al. (2002) used GPR to map the topography of restricting layer and combine this information with soil moisture data to infer the subsurface flow pathway. Gerber et al. (2007) applied GPR to detect Pleistocene periglacial slope deposit (PPSD) in a test site with different parent material and their results indicated that the condition at the test site may be applied to the field identification of PPSD. Grote et al. (2005) used GPR to detect reflection of a pavement with known depth and use this information to estimate soil water content and the results indicated that GPR data can be used to monitor water content in sub-asphalt layers. Truss et al. (2007) used time-lapsed GPR surveys to track vertical water movement in a karstic dissolution hole. Their results supported the conceptual model that water will move into surface depressions above a karstic dissolution hole which provided rapid pathway to the deeper subsurface.. Poisson et al. (2009) used GPR and other geophysical tools to image internal structure of a waste rock pile and the results of water infiltration monitored by GPR indicated preferential flow toward oxidized horizon at the east of test site, which had a fine particle size and high water retention capacity.

However, there is no study about the seasonal GPR signal changes at soil horizon interfaces and combined with high resolution real-time soil water content monitoring were seldom reported. Lunta, et al., (2005) used GPR to detect the buried object of known depth seasonally to estimate the soil water content. Their results indicate GPR estimated soil water content had an accuracy that was comparable with existing conventional methods such as neutron probe and TDR. However, event-based measurement of soil water content can not reveal seasonal soil water dynamics. Truss et al. (2007) compared GPR signals in two GPR events occurred at dry and wet conditions and their results indicated that an even distribution of water content

change throughout the entire oolite rock volume. However, lacking of measurement of soil water content may conceal flow processes implied by seasonal soil water content change.

GPR provides high spatial resolution compared with traditional point measurements and short period (several hours to several days) time-lapse GPR infiltration experiments offer valuable insight into flow pathways (Trinks et al., 2001; Freeland and Odhiambo, 2006; Saintenoy et al., 2008). However, these short period GPR investigations did not consider effects such as evapotranspiration and antecedent soil moisture on flow processes. In addition, artificial infiltration may not reflect the natural condition. Seasonal GPR signal changes under natural condition permit a broad time-frame to investigate these effects on hydrologic processes. By combining with high resolution of real-time soil moisture monitoring, flow path under different hydrologic conditions can be inferred. Explain why the seasonal GPR signal changes. The objectives of this study were to 1) investigate the effect of seasonal soil water dynamics on the GPR signal change at the identified soil layer interfaces in two contrasting soil-hillslopes, and 2) reveal hydrologic flow paths by combining seasonal GPR signal changes with high resolution real-time soil moisture monitoring.

## **Materials and Methods**

### **Study site and soils**

This study was conducted in the Shale Hills Critical Zone Observatory located in central Pennsylvania (Figure 5-1A), which is a small (7.9-ha) headwater forested catchment. The soils in this catchment were formed from shale colluvium or residuum and have a dominant texture of silt loam in the surface (with silty clay loam and clay loam in the B horizons in deeper soils).

We selected two hillslope grids with contrasting soils to compare seasonal GPR signals changes (Figure 5-1B and 5-1C). The first grid was located in the middle of a concave hillslope

(swale), with the soil identified as the Rushtown series. These are deep soils with  $> 2$  m depth to bedrock and local slope of about 15%. The second grid was located in the middle of a planar hillslope, with the soil identified as the Weikert series. These are shallow soils with depth to bedrock less than 0.5 m and local slope of about 30%. Table 5-1 lists the basic features of these two soils. Additional details about the soils studied can be found in Lin et al. (2006).

### **Experiment setup**

At the Rushtown soil in the swale, a 4.5 by 3.7 m survey grid was established perpendicular to the downslope direction (Figure 5-1B and 5-1C). For accurate repeatability of survey locations, GPR survey lines were scanned along a fixed rope that was anchored in the ground by PVC tube installed permanently at the starting and ending points of the marked survey line. The marked interval of survey lines was 0.31m. At the Weikert soil in the planar hillslope, a smaller grid of 2 by 0.7 m was also established along a downslope direction to improve repeatability of locations, and the marked interval of survey lines was 0.1m.

To understand the effect of seasonal water dynamics on the GPR signal, the two GPR grids were located close to two permanently installed automatic soil water moisture monitoring sites (Figure 5-1B and 5-1C), which were established in September 2006. When establishing these sites, a soil pit was excavated and an array of sensors was installed at different soil horizon based on the *in situ* observations and laboratory analysis of soil properties. These sensors include soil moisture sensors EC-5 (Decagon Devices, Inc., Pullman, WA) and TE525-WS tipping-bucket rain gauges (Texas Electronics Inc., Dallas, TX), which were connected to CR-10X datalogger (Campbell Scientific Inc., Logan, UT) with 10 minutes interval of recording data. The locations of soil moisture sensors installed at each site are illustrated in Figure 5-1D and 5-1E. The corresponding soil physical properties of the profile are listed in Table 5-1.

### **GPR instrument and survey**

The TerraSIR Subsurface Interface Radar (SIR) System-3000 (Geophysical Survey Systems, Inc., Salem, New Hampshire) with a 400-MHz antenna was used in this study. The 400-MHz was chosen after our in situ testing with a series of antenna frequencies (ranging from 200 to 900 MHz). The 400-MHz frequency provided the optimal balance of image quality and convenience of operation given the site conditions. The four GPR surveys at the two soils were conducted on October 20<sup>th</sup>, November 10<sup>th</sup>, 2008, April 24<sup>th</sup> and May 27<sup>th</sup>, 2009.

All GPR data collected were processed using the GPR-SLICE version 7.0 software (Geophysical Archaeometry Laboratory, Woodland Hills, California). The radargrams are processed in the exactly same way. The basic data processing steps included: (1) drift removal of direct current voltage to remove signal drift from zero value; (2) zero time adjustment to find the true ground surface reflection, (3) same gain factor applied for the consistent comparison.

### **Subsurface Layer identification**

The strength of a GPR reflection is a function of the contrast in dielectric constant across the reflecting boundary, and can be quantified by the reflection coefficient as:

$$r = \frac{\sqrt{\varepsilon_U} - \sqrt{\varepsilon_L}}{\sqrt{\varepsilon_U} + \sqrt{\varepsilon_L}} \quad 1)$$

Where  $\varepsilon_U$  and  $\varepsilon_L$  are the respective dielectric constants for the upper soil layer and soil layer below. Reflection coefficients range between 1 and -1. Positive sign indicates polarity is + - + while negative sign indicates - + -, a reversal in the polarity of the reflected signal.

Topp et al. (1980) showed that soil dielectric constant  $\varepsilon$  can be expressed as a function of water content as:

$$\varepsilon = 3.03 + 9.3 \theta + 146.0 \theta^2 - 76.7 \theta^3 \quad 2)$$

For low-loss media (i.e. soils with low salinity and clay content), the electromagnetic

wave velocity  $v$  of the soil can be related to the dielectric constant by

$$v = \frac{c}{\sqrt{\epsilon}} \quad 3)$$

where  $v$  is propagation velocity of electromagnetic wave in soil,  $c$  is free space electromagnetic velocity (0.3m/ns) .

When the wave velocity is known, the depth can be estimated by:

$$d = \frac{vt}{2} \quad 4)$$

Where  $d$  is depth and  $t$  is two way travel time

Subsurface layers were identified by comparing GPR reflection data with field soil profile observations and soil water content monitored in the profile. First, we pick up the major reflections in the radargrams. Then soil water contents measured by EC-5 sensors were used to estimate dielectric constant. In Rushtown soil, soil water content above BC horizon is depth - average water content over the Oe, A, Bw1, Bw2 and Bw3 horizon. In Weikert soil, soil water content above R horizon is depth -average water content over Oe, A, Bw and C. After that, the propagation velocity of electromagnetic is estimated using equation 3 and further converted to depth using equation 4. At last, we compared the depth of reflections on radargrams with soil profile data and validated the indentified soil horizons. Figure 5-2 and 5-3 illustrate the soil water content and the estimated reflection coefficients using equation 2) along interface in Rushtown and Weikert soil respectively.

## Results and Discussion

### Layer validation

The identified layer boundaries for Rushtown site and Weikert site are illustrated in Figure 5-4 and Figure 5-5 using GPR data collected on Oct.20<sup>th</sup>, 2008. Here we select one line for each site to demonstrate layer boundaries because other lines show similar pattern. In the Rushtown site, a strong reflection occurs at about 9ns and a less strong and discontinuous reflection occurs at about 17-21ns. By comparing soil water content data recorded at the same time when GPR surveys were conducted, we found that soil water content in BC layer was distinctively lower than the layer above and below. We infer these reflections are the corresponding Bw3-BC interface and BC-C interface. To confirm this inference, the average dielectric constant and velocity above BC-C interface was determined by applying equation 2 and 3 using the average soil water content from A to BC layer. The average velocity was 0.11m/ns. By applying equation 4, the estimated depths at two reflections were about 50cm and 95-115cm respectively, which is very close to the soil profile (45cm and 90cm) in the soil pit nearby.

In the Weikert site, two reflections were also observed in the radargrams at about 6-9 ns and 15-18 ns respectively. By comparing soil water content data, the first reflections at 6-9 ns is most likely to be the soil bedrock interface because the soil water content in the R horizon is also distinctively lower than that in the above soil horizons. Using methods mentioned above, the average velocity above R horizon is 0.1m/ns and the estimated depths at first reflections were about 30- 45cm, which is consistent with soil profile at soil pit nearby (37cm). As for the second reflections, we interpret as unweathered rock, which is consisted of massive fractured rock compared to the plate-like weathered rock in the R horizon. A exposure soil pit upslope the survey grid in Weikert soil also support this explanation (Figure 5-6).

### **Seasonal GPR signal change in the deep Rushtown soil**

Figure 5-7A shows the GPR reflection profiles obtained at the same survey line for the four GPR events and the corresponding soil water content dynamics when the GPR survey was conducted were shown in Figure 5-7B. The soil water content showed a general trend from dry condition to wet condition from October, 2008 to May, 2009. Figure 5-2 summarizes water content change for the four GPR events.

With the increasing of soil water content, the GPR reflection profiles show following patterns:

1) The reflection at Bw3-BC interface (cyan dash line) became stronger and more hyperbolas and crisscross shape occurred near this interface as increasing of soil water content. The stronger reflection can be explained by the reflection coefficient at Bw3-BC interface. Figure 5-2 show a trend of increasing reflection coefficient from dry to wet condition. The hyperbolas are caused by the point sources, which is likely to be the tree roots. Field log (Table 5-1) indicated the coarse tree root throughout the Bw3 horizon and we did see the protrude tree roots along the survey lines. During wet condition, these tree roots may form the preferential path for water redistribution, which leading to point diffraction in the radargrams. The most prominent crisscross pattern occurred on May 27<sup>th</sup>, 2009, which was conducted after a small rainfall event. The crisscross pattern and multiple hyperbolas dominated in the radargram. This effect was also reported by Truss et al. (2007), who found irregular rock surface and tree roots caused small scale preferential flow leading to multiple hyperbolic scatterings in GPR images.

2) The reflection at BC-C interface (red dash line) became more clear and continuous as soil water content became wet. On October 20<sup>th</sup>, 2008, the reflection at BC-C interface showed an intermittent linear pattern, while on April 24<sup>th</sup> and May 27<sup>th</sup>, 2009, the reflection at BC-C interface displayed a stronger and continuous linear pattern. The more clear reflections at BC-C interface can also be explained by reflection coefficient between BC and C horizon. As illustrated

in Figure 5-2, the reflection coefficients between two horizons increased as soil became wet, which increase the reflection strength detected by GPR. The continuous line reflections indicate that soil water may move along boundaries between BC and C horizon, which cause continuous dielectric contrast along the boundaries that can be detected as line pattern by GPR. In the four GPR events across dry to wet period, the soil water content in BC horizon is always lower than that in C horizon (Figure 5-7B) and the seasonal soil water content from Oct., 2008 to May, 2009 at ten minutes interval also show the BC horizon has lower water content than that in C horizon (Figure 5-8 A). Soil sample analyses indicate BC and C horizon show similar vertical hydraulic conductivity and both horizons have lower vertical hydraulic conductivity than the upper horizon. All these evidence indicate that soil water may not infiltrate through the BC horizon and perched at BC-C interface to form the continuous dielectric contrast between two horizons. However, the C horizon has higher lateral hydraulic conductivity than that in BC horizon (table 5-1), which indicates that lateral flow from upslope may contribute to the increasing of soil water content in C horizon. Figure 5-8B demonstrates potential lateral flow contributing to the increase of soil water content in C horizon. Three days after a rainfall event, soil water content in C horizon show a big increment, while the soil horizon above only show small increment. This indicates vertical infiltration can't support increased amount of water in C horizon and lateral flow from upslope will contribute. Thus, the line reflection between BC and C horizon in the wet condition may be due to the lateral flow into C horizon, which cause continuous dielectric contrast at the interface.

#### **Seasonal GPR signal change in the shallow Weikert soil**

Figure 5-9A show seasonal GPR radargrams in Weikert soil. With the increasing of soil water content, the GPR reflection profiles show following patterns:

- 1) The reflection at soil-bedrock interface (CR-R) showed that more point scatters appeared in radargram as soil became wet, which made the interface less continuous and difficult to pick up. This is obvious when comparing radargram on October, 2008 with that on April,

2009(Figure 5-9A). On October 20<sup>th</sup>, 2008, radargram showed a clear and continuous reflection at soil-bedrock interface, while radargram on April 24<sup>th</sup>, 2009 showed intermittent strong reflection along the interface. The reason may be due to the heterogeneous distribution of water along soil-bedrock interface when soil became wet, which lead to local increase of reflection coefficient and form the local strong reflection in radargram. Although the reflection coefficient estimated by soil moisture sensors showed an increasing trend as soil became wet (Figure 5-3), the point measurement only reflected local contrast. Combining GPR with point measurement showed potential to reveal subsurface heterogeneity at larger scale.

2) The reflection at weathered and unweathered bedrock interface became less discontinuous along the interface and strong crisscross pattern occurred below the interface as soil became wet. When comparing radargrams at dry condition (October and November, 2008) with wet condition (April and May, 2009), the radargrams at dry condition show a clear and continuous reflection at the interface while at wet condition the line reflection seemed broke near 1m survey distance and a strong crisscross reflection occurred below. This pattern indicates an abrupt dielectric contrast existed at this position. The reason causing the abrupt dielectric contrast is likely to be the water infiltrating into the fracture of unweathered bedrock through the preferential path, which lead to diffraction of GPR wave since the water and rock has distinctively different dielectric value.

### **Implications for understanding hydrological processes in contrasting soils and hillslopes**

#### **Implication for understanding hydrological processes**

In the Rushtown soil, the BC horizon has a lower soil water content than the horizons above and below during both dry and wet periods, leading to dielectric contrast that can be detected by GPR. The reason for this is that the BC horizon has a higher bulk density and lower vertical saturated hydraulic conductivity as compared with the horizons above (Table 5-1), which make it less permeable to the percolating water. The hydrological implication for this is that water

would move laterally above this less permeable layer under slope gradient during a rainfall event, which is demonstrated in Figure 5-10. In Figure 5-10, soil water content in the Bw3 horizon (the horizon just above the BC horizon) showed a large increase during a rainfall event while the soil water content above and below this layer showed little response, indicating a lateral flow through the horizon above the BC horizon. The C horizon (just below the BC horizon) has similar bulk density and vertical saturated hydraulic conductivity as the BC horizon. However, the soil water content in the C horizon is higher throughout dry and wet periods (Figure 5-8 A). As explained earlier, this was due to lateral recharge from upslope areas. How did water move to the C horizon may be explained by the hydrological condition in the Weikert soil: Seasonal GPR signal changes in the Weikert soil indicate strong crisscross pattern occurred below the weathered-unweathered bedrock interface under wet condition, which indicate water has infiltrated into the fractured bedrock. As the infiltrated water in the bedrock could move laterally downslope under steep slope gradient, the lateral flow would contribute to higher soil water content in deeper horizons in downslope soils.

#### **Implication of seasonal GPR pattern**

The seasonal signal changes of GPR in two soils presented above illustrate the effect of soil horizon interfaces on soil water distribution, which cause the different GPR reflection patterns under a dynamic hydrological condition. Figure 5-11 illustrated the GPR reflection patterns in two soils using 3D format during the dry (October 20<sup>th</sup>, 2008) and wet (April 24<sup>th</sup>, 2009) condition. In dry condition, both radargrams in Rushtown and Weikert showed a linear reflection indicating a relatively uniform distribution of water. While in wet condition, both radargrams in Rushtown and Weikert showed point-scatter reflections, which indicate non-uniform distribution of water. One implication of such heterogeneous patterns is that we need “areal image” of subsurface soil moisture to link to point-based soil moisture monitoring to explain spatial distribution of soil water. Another implication of seasonal GPR pattern change

indicates the optimal time to apply GPR to identify the soil horizon. In Rushtown soil, reflection in BC-C horizon is more apparent in wet condition than that in dry condition. On the contrary, in Weikert soil, reflection at weathered-unweathered bedrock interfaces is more apparent in dry condition than that in wet condition. Figure 5-12. A and B illustrate the indentified BC-C horizon in Rushtown at wet condition (April 24<sup>th</sup>, 2009) and weathered-unweathered bedrock interfaces in Weikert soil at dry condition (October 20<sup>th</sup>, 2008).

### **Implication for hydrological modeling**

Existing of soil horizon affects soil water distribution both laterally and vertically. These horizons may function as important “nodes” in subsurface flow network. In certain conditions, such as high antecedent soil moisture content, strong and/ or long duration rainfall, the horizons may be activated and deliver water both laterally and vertically. In our example, water may infiltrated into bedrock fracture below shallow Weikert soil and move laterally. In addition, water may perched above BC horizon in Rushtown soil during rainfall event and lead to water moving along the above layer. This implied effect of soil horizon and threshold behavior need to be considered when conceptualizations of subsurface network modeling.

### **Summary and conclusion**

Four repeated GPR surveys were conducted during dry to wet periods in two different soils located in contrasting hillslopes. In the deep Rushtown soil, the horizon interfaces of the Bw3- BC and BC-C were detected by GPR. However, under wet condition, the Bw3- BC interface showed more crisscross patterns and hyperbola shapes, which indicated preferential water distribution along tree roots. The BC-C interface showed more continuous line reflection under wet condition than dry conditions because of the increases reflection coefficient when wet. Based on the soil layer properties and real-time soil water monitoring data, the increased

reflection coefficient at the BC-C interface could be attributed to lateral recharge from upslope areas to the C horizon.

In the shallow Weikert soil, the soil-bedrock interface and weathered-unweathered interface showed a clear line reflection in GPR radargram during dry period. However, during wet period, the soil-bedrock interface showed intermittent local strong reflection, which was likely caused by preferential water distribution near the interface. Near the weathered-unweathered interface, strong crisscross patterns occurred under wet condition, implying that water infiltrated into the fractures of the bedrock leading to abrupt dielectric contrast between water and the rock.

Based on the seasonal GPR signal changes, combined with real-time soil moisture monitoring, hydrologic flow paths in planar hillslopes with shallow soils and steep slopes can be inferred. Under wet condition, rainwater tended to infiltrate into the fractures of the underlying bedrock and moved downslope and then recharged deeper portion of the soils located in downslope areas.

The seasonal GPR signal changes also suggest that there is an optimal time for using GPR to detect soil layers. In the Rushtown soil, wet condition without rainfall event was optimal period for detecting the BC-C horizon interface by GPR. While in the Weikert soil, dry condition was optimal for detecting the soil-bedrock and weathered-unweathered interfaces by GPR.

Our results also indicate that the advantages of combining high resolution real-time soil moisture monitoring with repeated GPR surveys to reveal the point feature and spatial pattern. For instance, the point measurement of soil water content in Weikert soil indicate increasing reflection coefficient between weathered-unweathered interfaces as it is becoming wetter. However, the radargrams did not show more clear linear reflection along the interfaces. This indicate that point measurement can't explain the spatial heterogeneous of water distribution. In

addition, high resolution of real time data revealed potential lateral flow at Bw3 horizon and C horizon, which made up the temporal resolution of seasonal GPR survey.

### References

- Bonell, M. 1998. Selected challenges in outflow generation research in forests from the hillslope to headwater drainage basin scale, *Journal of the American Water Resources Association* 34, 765–785.
- Birken, R., Versteeg, R. 2000. Use of four-dimensional ground penetrating radar and advanced visualization methods to determine subsurface fluid migration. *Journal of Applied Geophysics* 43, 215–226.
- Daniels, J. J., R. Roberts, Vendl, M. 1995. Ground penetrating radar for the detection of liquid contaminants. *Journal of Applied Geophysics* 33, 195-207.
- Freeland, R. S., Odhiambo, L. O. 2006. Subsurface characterization using textural features extracted from GPR data. *Transactions of American Society of Agricultural and Biological Engineers*. 50, 287–293.
- Freer, J., McDonnell, J. J., Beven, K. J., Brammer, D., Burns, D., Hooper, R. P., and Kendall, C. 1997. Topographic controls on subsurface storm flow at the hillslope scale for two hydrologically distinct small catchments, *Hydrological Processes* 11, 1347–1352.
- Freer, J., McDonnell, J. J., Beven, K. J. et. al. 2002. The role of bedrock topography on subsurface storm flow. *Water Resources Research* 38(12), WR000872.
- Giannopoulos, A. 2005. Modelling ground penetrating radar by GprMax. *Constr. Build. Mater.* 19, 755–762.

- Gish T. J., Dualaney W. P., Kung K.- J. S., Daughtry C. S. T., Doolittle J. A., and Miller P. T. 2002. Evaluating use of ground-penetrating radar for identifying subsurface flow. *Soil Sci. Soc. Am. J.* 66, 1620-1629.
- Hewlett, J. D., and A. R. Hibbert. 1965. Factors affecting the response of small watersheds to precipitation in humid areas, Paper Presented at International Symposium on Forest Hydrology, Pa. State Univ., University Park.
- Huisman, J. A., Hubbard, S. S., J. D. Redman, and A. P. Annan. 2003. Measuring Soil Water Content with Ground Penetrating Radar: A Review. *Vadose Zone Journal* 2, 476–491.
- Jérôme Poisson, Michel Chouteau, Michel Aubertin, Daniel Campos. 2009. Geophysical experiments to image the shallow internal structure and the moisture distribution of a mine waste rock pile. *Journal of Applied Geophysics* 67, 179–192.
- Lin, H. 2006. Temporal Stability of Soil Moisture Spatial Pattern and Subsurface Preferential Flow Pathways in the Shale Hills Catchment. *Vadose Zone Journal* 5, 317-340.
- Lin, H.S. 2010. Linking principles of soil formation and flow regimes. *Journal of Hydrology*. (In press)
- Lin, H. and Zhou X. 2008. Evidence of subsurface preferential flow using soil hydrologic monitoring in the Shale Hills catchment. *European J. Soil Sci.* 59, 34-49.
- Liu, L., He, K., Xie, X. 2007. Image enhancement with wave-equation redatuming: application to GPR data collected at public transportation sites. *J. Geophys. Eng.* 4, 139–147.
- Lunta, I.A., S.S. Hubbards, Y. Rubin. 2005. Soil moisture content estimation using ground-penetrating radar reflection data. *J. Hydrol.* 307, 254–269.
- Grasmueck, M., R. W., and Heinrich Horstmeyer. 1996. 3-D ground-penetrating radar applied to fracture imaging in gneiss. *Geophysics* 61(4), 1050-1064.
- Trinks, I., Wachsmuth, D., H. Stümpel. 2001. Monitoring water flow in the unsaturated zone using georadar. *First Break* 19, 679-684.

- Truss S., Grasmueck M., Vega S., and Viggiano D. A. 2007. Imaging rainfall drainage within the Miami oolitic limestone using high-resolution time-lapse ground-penetrating radar. *Water Resources Research* 43, doi : 10.1029/2005WR004395.
- Ronald E. Y., Freeland, R.S., Ammons, J.T. and Leonard, L., L. 2001. Mapping agricultural fields with GPR and EMI to identify offsite movement of agrochemicals. *Journal of Applied Geophysics* 47: 251-259.
- Sakaki, T., Limsuwat, A. Kathleen M., and Tissa H. 2008. Empirical two-point A-mixing model for calibrating the ECH2O EC-5 soil moisture sensor in sands. *Water Resources Research* 44, W00D08, doi:10.1029/2008WR006870.
- Sidle, R., S. Noguchi, Y. Tsuboyama, and K. Laursen. 2001. A conceptual model of preferential flow systems in forested hillslopes: evidence of self-organization. *Hydrological Processes* 15, 1675–1692.
- Saintenoy, A., Schneider, S., Tuchoka, P. 2008. Evaluating ground penetrating radar use for water infiltration monitoring. *Vadose Zone Journal* 7, 208-214.
- Todd, M.S., Jeff, P.R., George M.H. 2000. Shallow subsurface storm flow in a forested headwater catchment: Observations and modeling using a modified Topmodel. *Water Resources Research* 36(9), 2575–2586.
- Tromp-van Meerveld, H. J. and McDonnell, J. J. 2006. Threshold relations in subsurface storm-flow 1. A 147 storm analysis of the Panola hillslope, *Water Resources Research* 42, W02410, doi:10.1029/2004WR003778.
- Weiler and McDonnell. 2004. Virtual experiments: a new approach for improving process conceptualization in hillslope hydrology. *J. Hydrol.* 285, 3-18.
- Weyman, D. R. 1973. Measurements of the downslope flow of water in a soil. *J. Hydrol.* 20, 267–288.

Whipkey, R. Z. 1965. Subsurface stormflow from forested slopes. *Bull. Int. Assoc. Sci. Hydrol.* 10, 74–85.

Table 5-1: Soil profile characteristics of the two soil series investigated in this study

Horizon	Depth (m)	Sensor installation depth (/m)	Soil texture	Saturated hydraulic conductivity		> 2mm rock fragment # (%)	Bulk density (g/cm <sup>3</sup> )	Pedality # (structure)	Roots
				Vertical cm/min	Horizontal 0.701				
<b>Weikert Series</b>									
Oe	0-0.05	0.05				22	0.425		Very many fine roots throughout
A	0.05-0.12	0.08	silt loam	1.863		29	0.960	2 f gr	Very many fine roots throughout
Bw	0.12-0.28	0.15	silt loam	2.280		20	1.260	2 f sbk	Common fine roots in cracks
CR	0.28-0.37	0.28	silt loam	0.409	0.701	90		1 f sbk	Few fine roots in cracks
R	0.37	0.38							
<b>Rushtown Series</b>									
Oe	0-0.05	0.05		6.374		11	0.425		Very many fine roots throughout
A	0.05-0.12	0.08	silt loam	0.432	0.684	34	1.807	3 f gr	Very many fine roots throughout
Bw1	0.12-0.17	0.15	silt loam	0.334	0.493	39	1.204	2 f sbk	Many fine roots throughout
Bw2	0.17-0.26	0.22	silt loam	0.528	0.262	28	1.292	1 m sbk	Common fine roots throughout
						29	1.537	1 m sbk	Common fine to coarse roots throughout
Bw3	0.26-0.45	0.40	silt clay loam	0.979	0.17				
BC	0.45-0.90	0.68	silt clay loam	0.087	0.259	38	1.637	massive	Few medium roots throughout
C	0.9-1.78+	1.22	silt clay loam	0.08	4.52	60	1.652	massive	

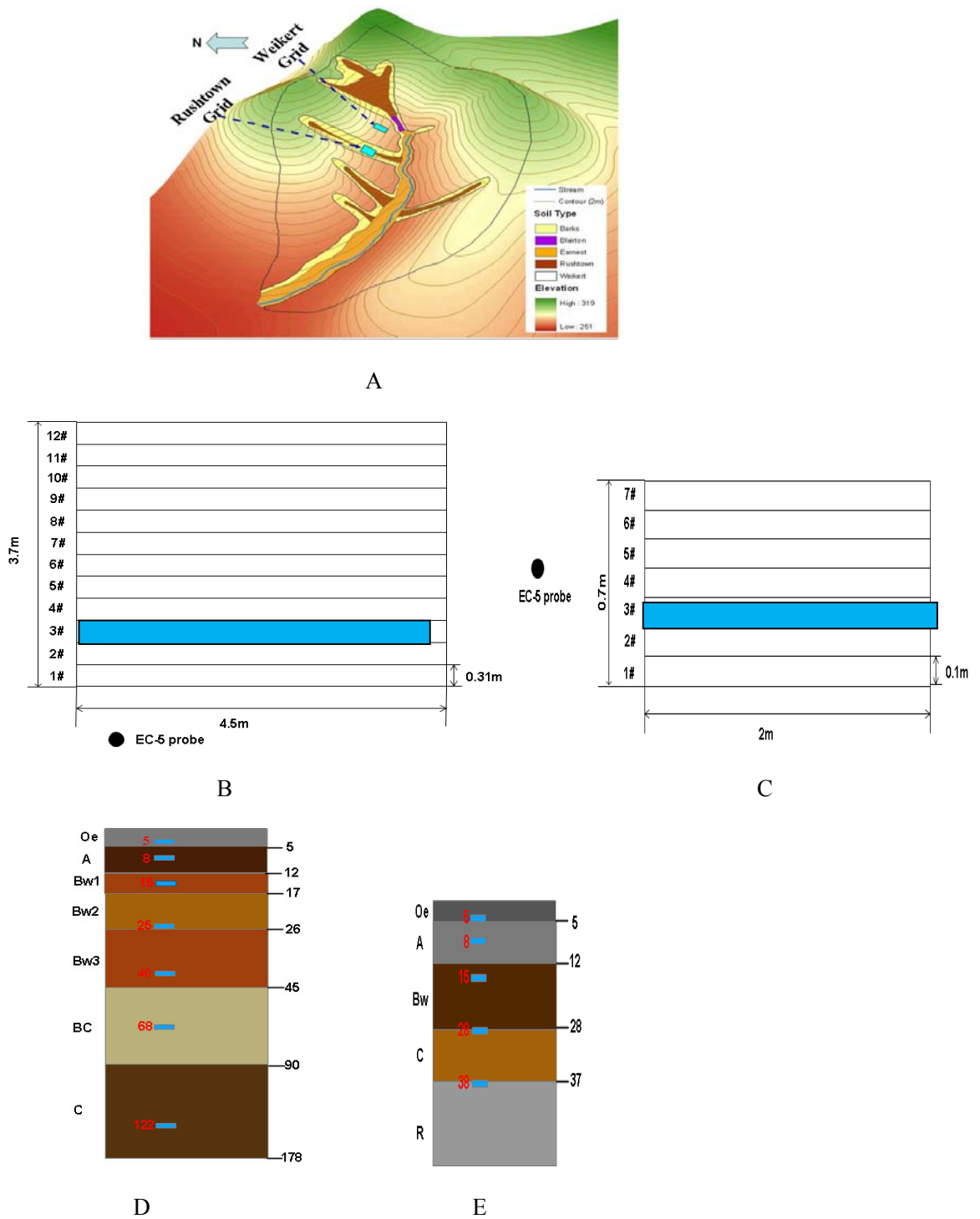


Figure 5-1: A. The study sites and locations of GPR survey grids. b) Layout of the Rushtown grid. C. Layout of the Weikert grid. D. EC-5 sensor location in Rushtown soil pit. E. EC-5 sensor location in Rushtown soil pit. (Black circle in B and C indicate soil pit. (black circle in B and C indicate soil pit installing EC-5 sensor, blue color in BC indicate survey line used in analysis)

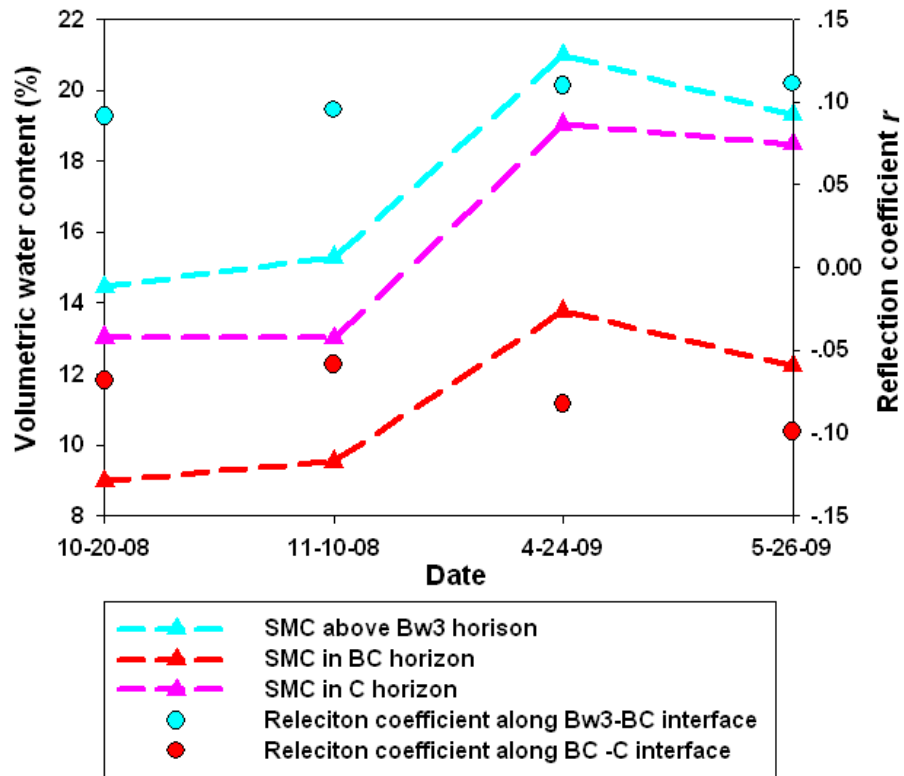


Figure 5-2: Reflection coefficient  $r$  change in Rushtown soil (triangle dash lines indicate soil moisture content (SMC), dots indicates reflection coefficients estimated using soil water content)

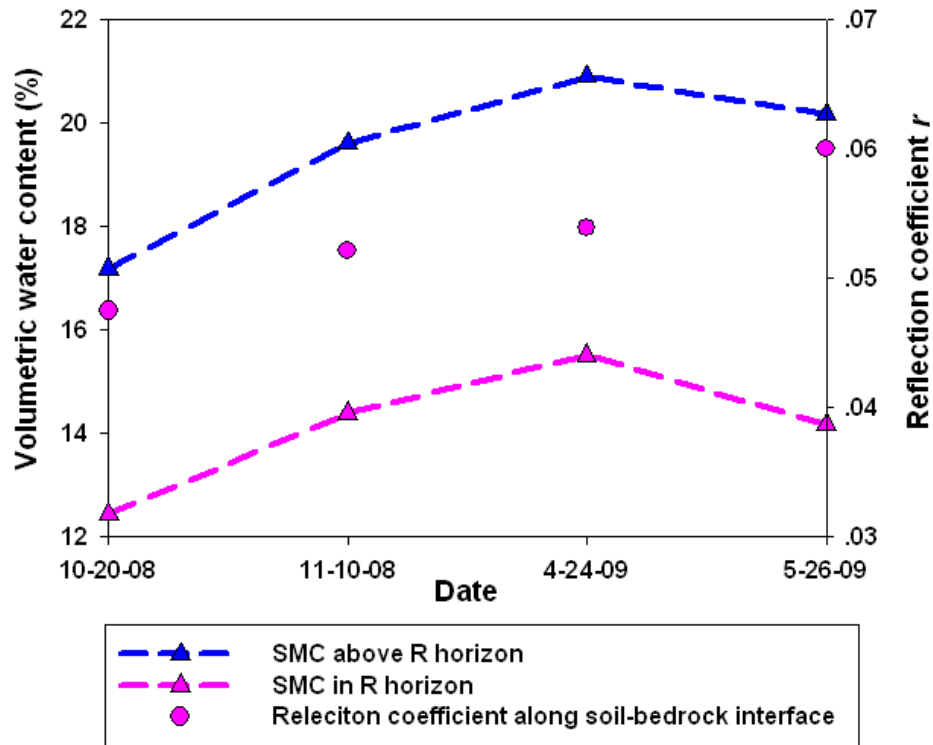
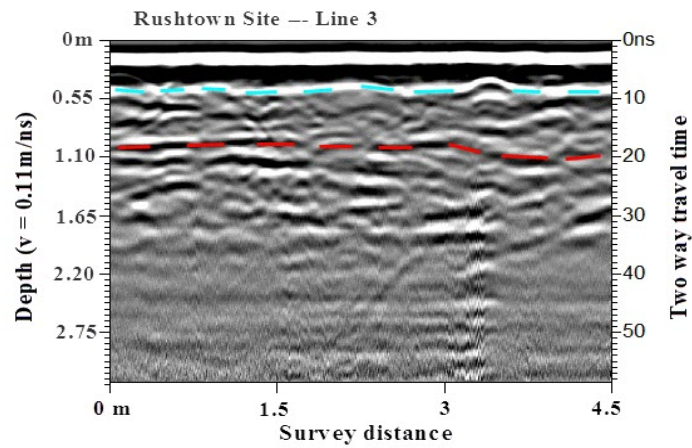
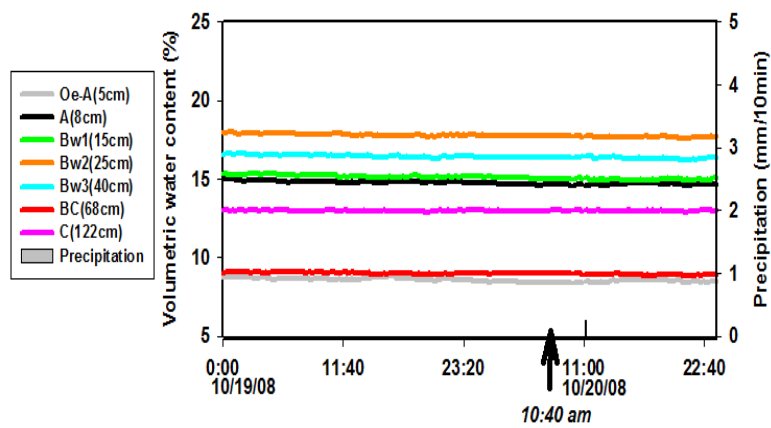


Figure 5-3: Reflection coefficient  $r$  change in Weikert soil (triangle dash lines indicate soil moisture content (SMC), dots indicates reflection coefficients estimated using soil water content)



A



B

Figure 5-4: A. Soil layers identified in the Rushtown soil (cyan dash line indicate Bw3-BC interfaces and red dash line indicate BC-C interfaces) B. the real time soil water content monitoring when GPR survey was conducted in Oct.2008.

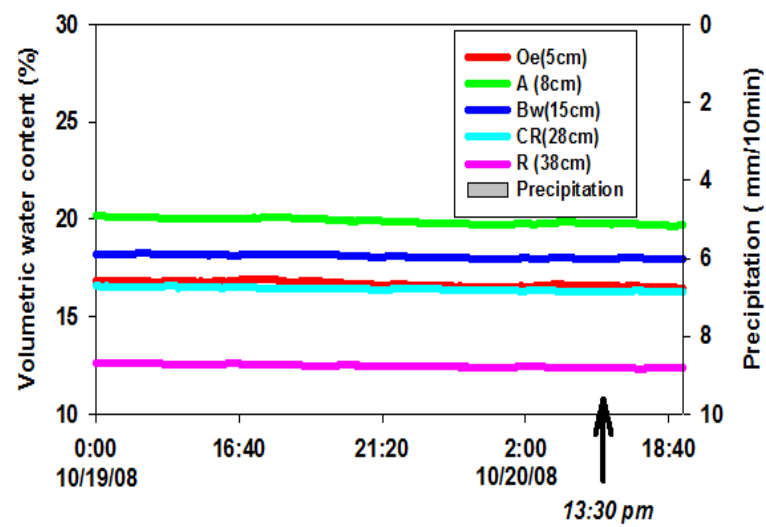
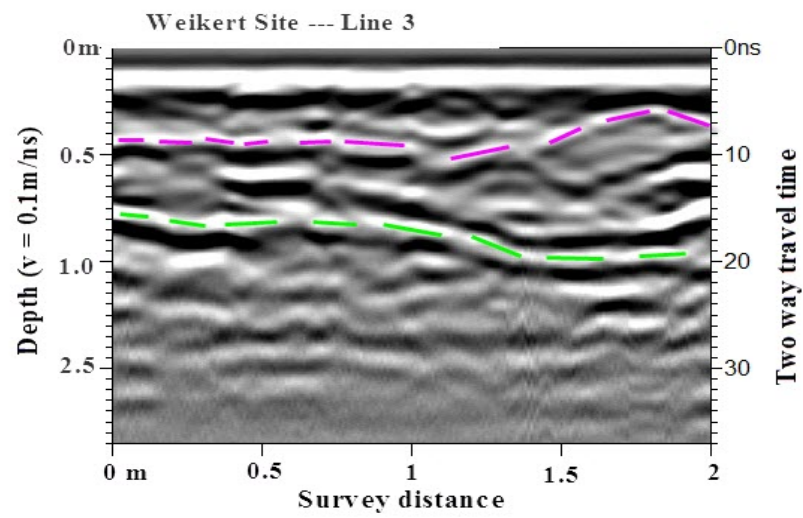


Figure 5-5: A. soil layers identified in the Weikert soil.( pink dash line indicate soil-bedrock interfaces and green dash line indicate weathered and unweathered rock interface. B. the real time soil water content monitoring when GPR survey was conducted in Oct. 2008.

A



B

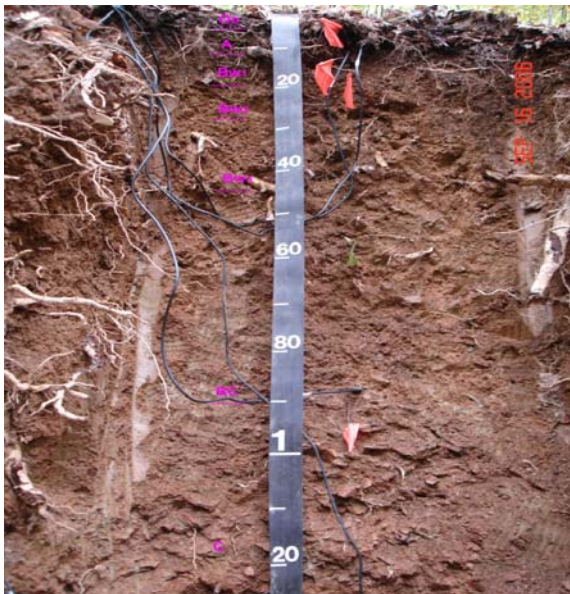


Figure 5-6: A. Photograph showing weathered rock and unweathered rock in Weikert soil. B. soil profile in Rushtown soil.

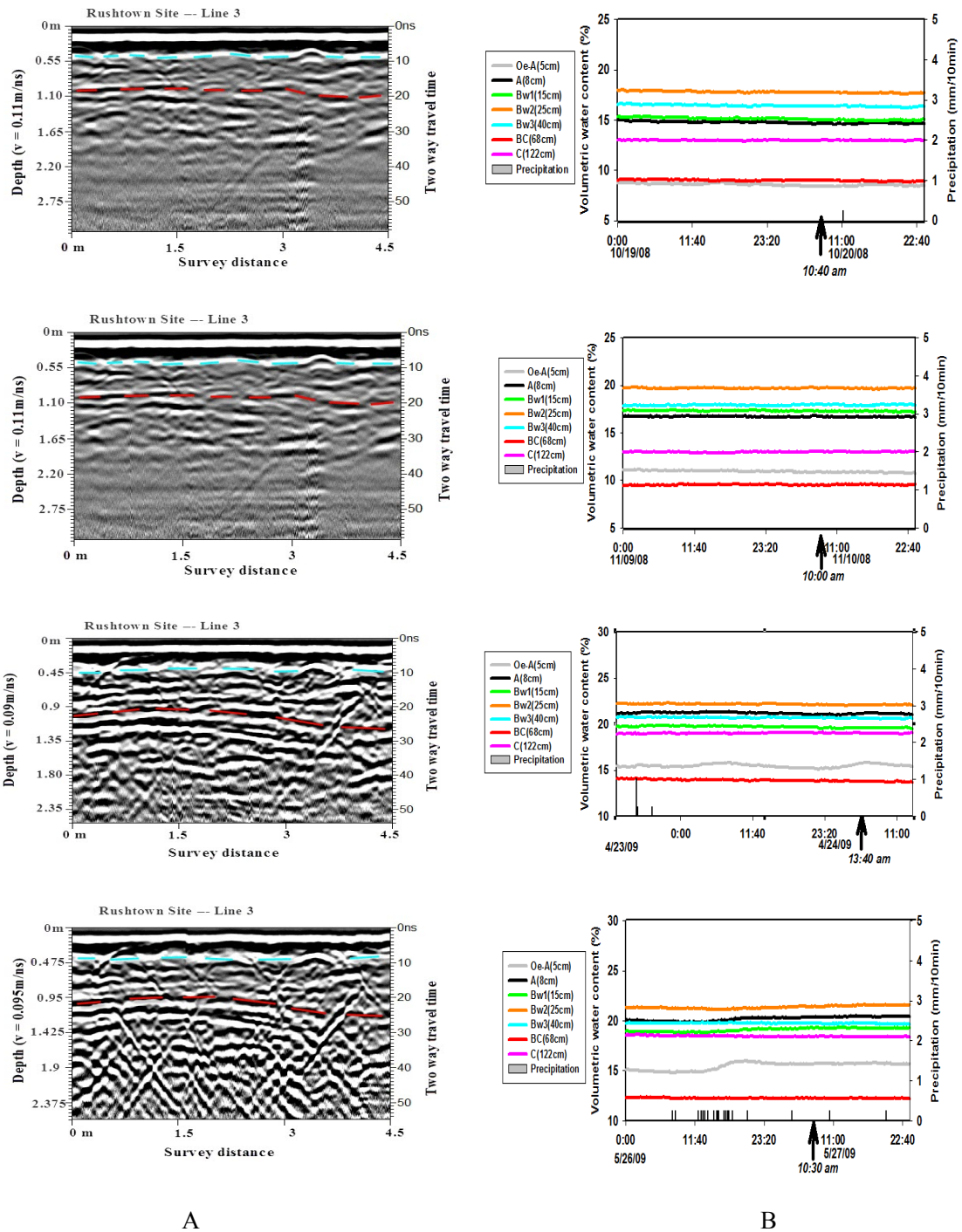
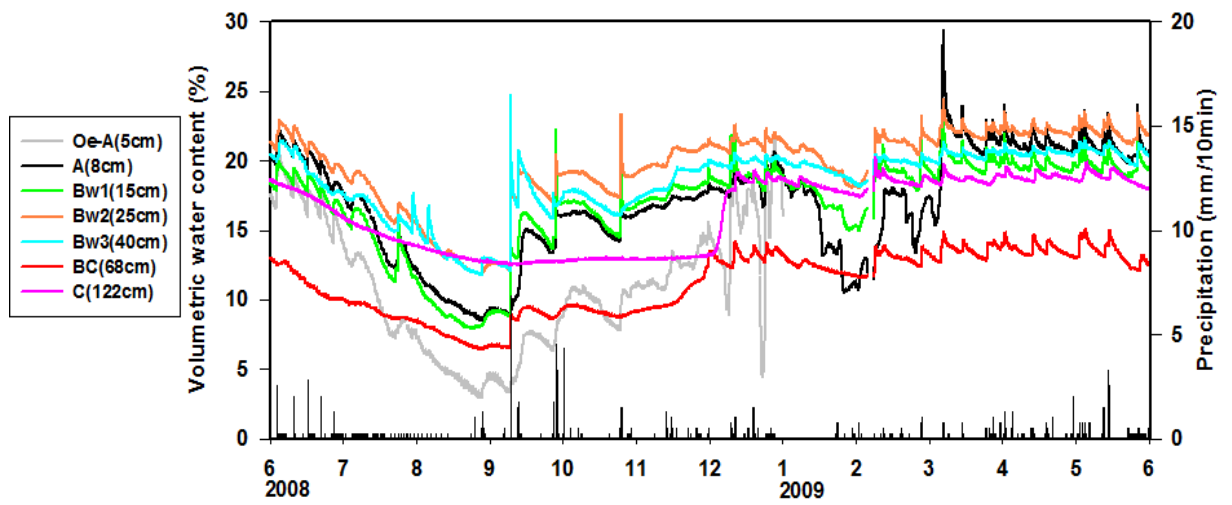
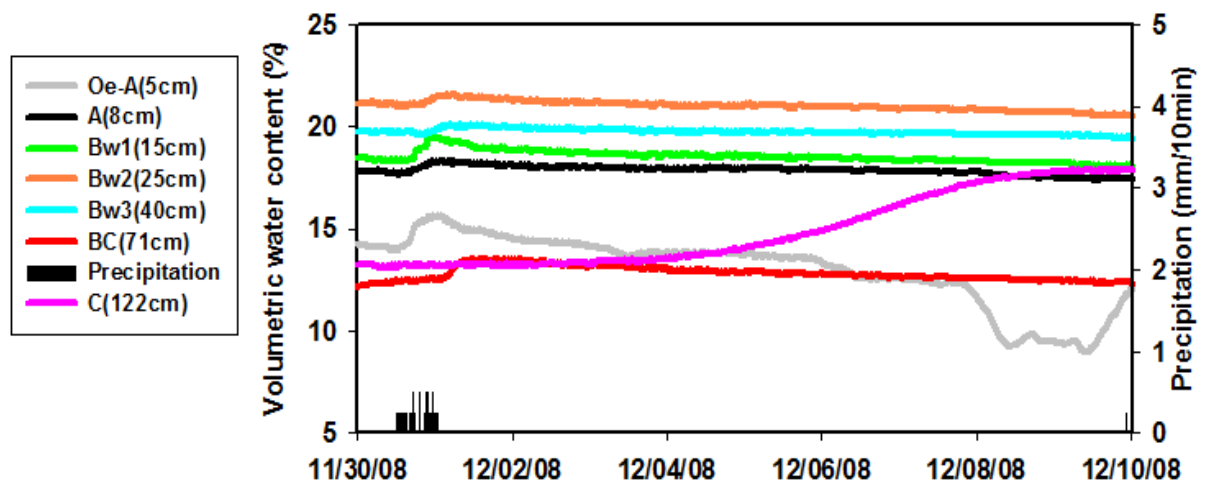


Figure 5-7: A. Seasonal GPR signal change in Rushtown soil (cyan dash line indicate Bw3-BC interfaces and red dash line indicate BC-C interfaces) B. Corresponding soil moisture content monitoring during GPR survey (black arrow indicate time when conducted GPR survey (black arrow indicate time when conducted GPR survey))

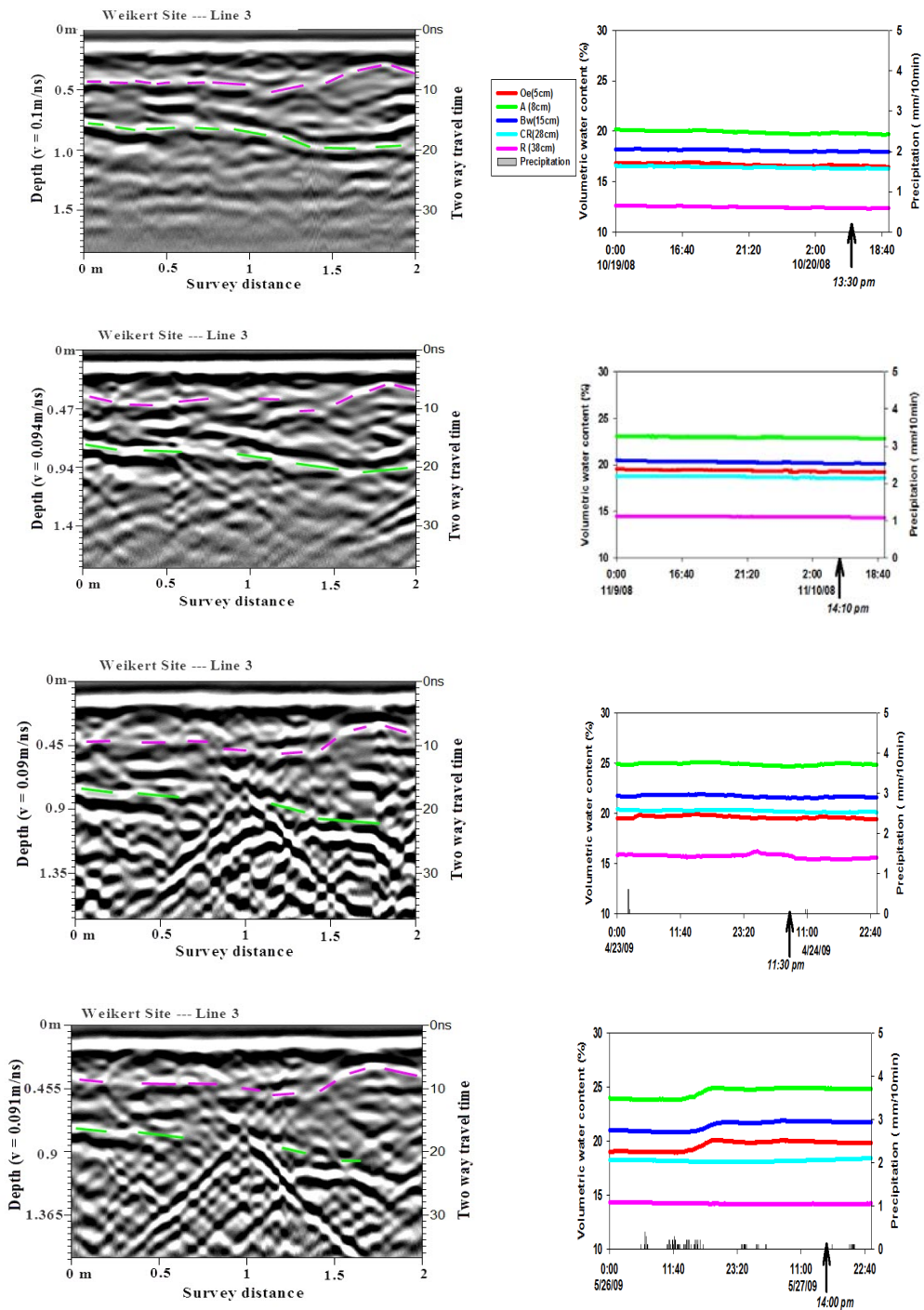


A



B

Figure 5-8: A. Seasonal soil water content monitoring in Rushtown soil. B. soil water content increase in C horizon



A

B

Figure 5-9: A. Seasonal GPR signal change in Weikert soil (pink dash line indicates soil-bedrock interfaces and green dash line indicates weathered and unweathered rock interface)  
 B. Corresponding soil moisture content monitoring during GPR survey (black arrow indicate time when conducted GPR survey)

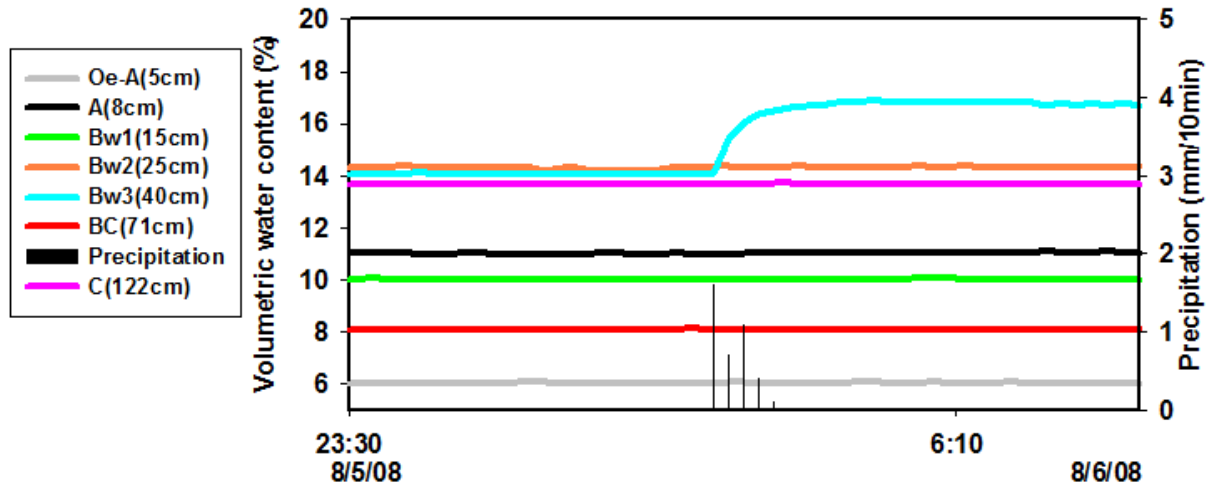


Figure 5-10: Illustration of lateral flow through Bw3 horizon in Rushtown soil

Dry condition (October 20<sup>th</sup>, 2008)

Wet condition (April 24<sup>th</sup>, 2009)

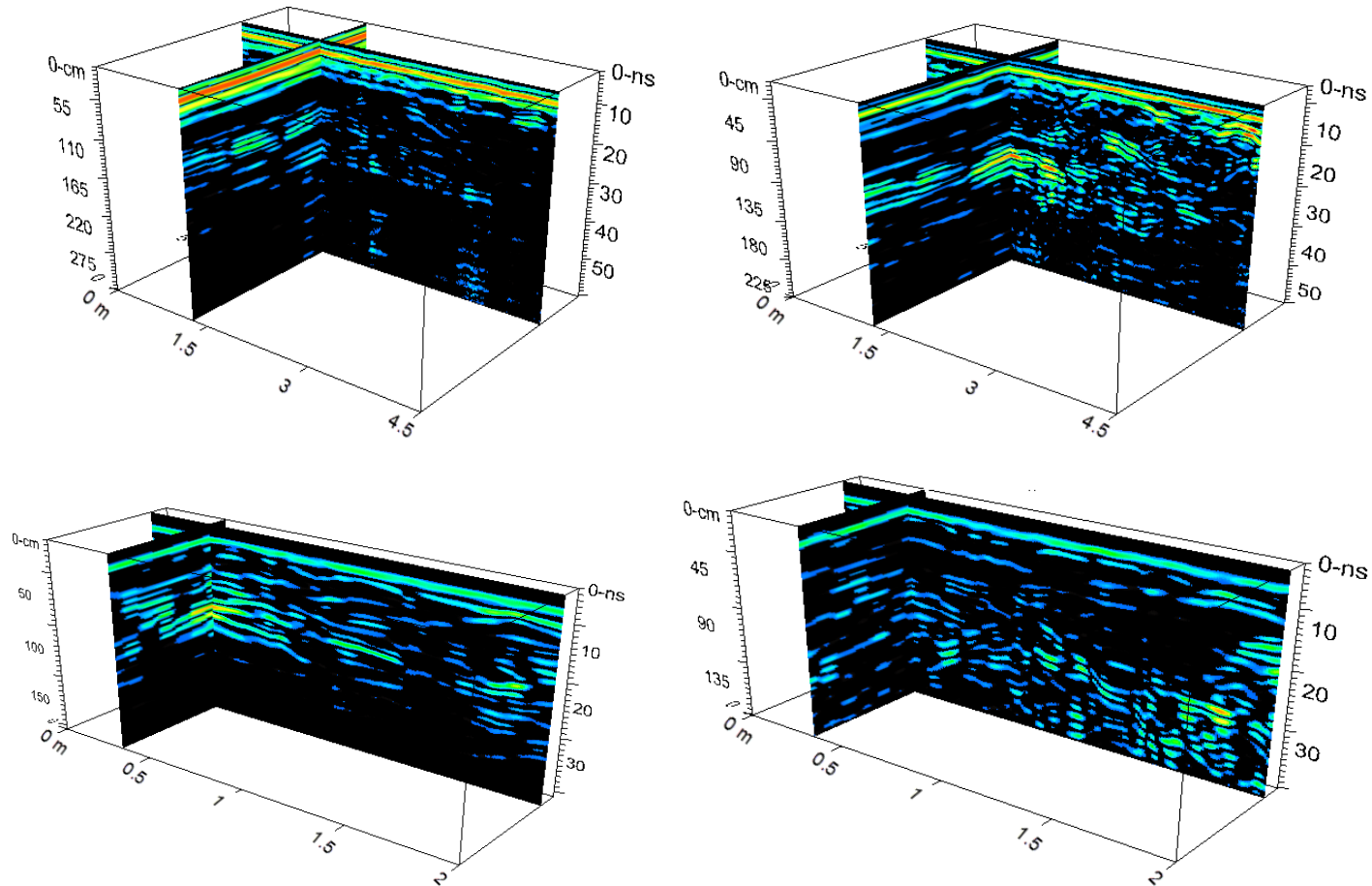


Figure 5-11: Wet and dry GPR pattern in Rushtown (top) and Weikert soil (bottom)

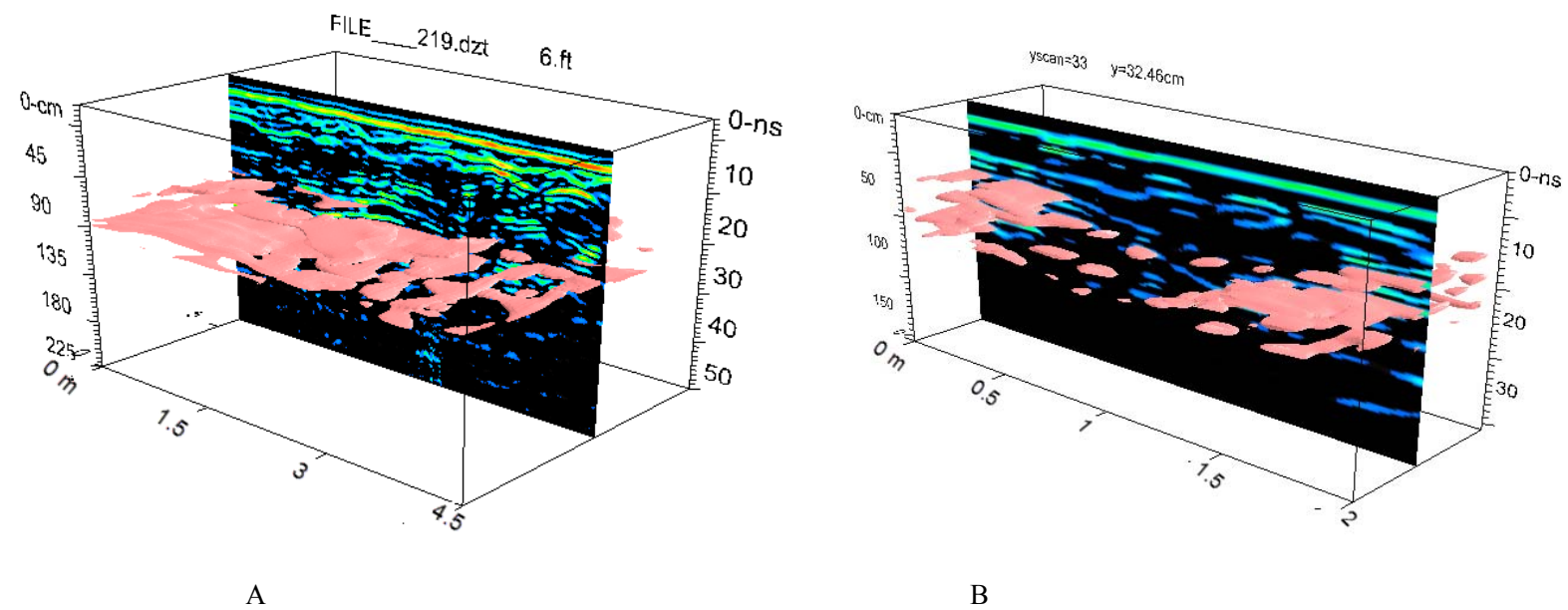


Figure 5-12: Optimal time to detecting soil horizon. A. BC-C interface in Rushtown soil at wet condition (April 24th, 2009) B. weathered-unweathered bedrock interfaces in Weikert soil at dry condition (October 20th, 2008) . Orange color indicate the explained

## **Chapter 6**

### **A MATLAB-based Software for Processing, Displaying, and Interpreting GPR Data**

#### **Abstract**

Ground penetrating radar (GPR) is a rapidly growing geophysical tool that has seen tremendous progress in the development of theory, techniques, and applications. The GPR provides a quick and nondestructive way to image subsurface spatial pattern and has become a valuable method of exploring shallow subsurface structures for scientists, engineers, and consultants. However, interpretation of GPR data involves the use of sophisticated software for processing. Although several commercial packages are available from GPR manufacturers or other commercial vendors, they are often expensive, platform dependant, and cannot be modified for specific needs of a user. As an alternative to commercial software, an open-source, free MATLAB-based software called TGPR has been developed in this study to process, display, and interpret GPR data that has potential for wide applications. The TGPR software can process both 2D and 3D GPR survey data and has the ability to batch process GPR surveys containing several profiles. With user friendly interfaces, the TGPR can interactively edit radargrams and manually or automatically correct topography. The TGPR also provides several utilities to enhance 2D and 3D visualization of GPR data, including 1) trace view, wiggle view, and image view of 2D data, 2) slice view, cube view, and transparent view of 3D data, 3) ten built-in color tables to enhance image display, and 4) layer editing of 2D images. In addition, with structured programming, the TGPR can be easily expanded and customized.

## Introduction

Ground Penetrating Radar (GPR) is a high-resolution geophysical technique that utilizes the transmission and reflection of high frequency (10–1200 MHz) electromagnetic waves to investigate subsurface variation nondestructively. Compare with point-based measurements, GPR provides a quick and continuous image of subsurface spatial pattern. However, interpretation of GPR data involves the use of sophisticated software packages for processing. These packages are usually available from GPR manufacturers or other commercial vendors. Although highly advanced, commercial processing packages are built for generic use and not for solving special problem. When users have special requirements for solving their particular problems, they need to wait for the update if their requests can be incorporated into the next version. Expensive license costs also have prevented the broad use of commercially available GPR processing software.

Recently, several open-source GPR software appeared and provided a low cost alternative to commercial software. Radar Unix developed by Grandjean and Durand (1999) provide a complete processing of GPR data. Although it has easy graphical user interface (GUI), it runs on the Unix and Linux platform, which restricts its wider application by non-Unix or non-Linux users. The GPR data processing software written by Lucius and Powers (2002) provide some general processing of GPR data. However, this software runs in the Windows DOS mode without GUIs, which makes it difficult for the average users. The GP Workbench is a general-purpose geophysical data processing program written primarily for GPR (Oden and Moulton, 2006). However, it needs a third party software (Surfer, Golden Software, Inc., Golden, CO) to produce high quality image and the most processing of GPR focuses on one dimensional wave form data. The above-mentioned software are all written in C/C++ language, the change and reuse of these programs are limited for common practitioners since they require advanced computer skills.

The MATLAB provides a high level programming environment that includes graphics facility, vector syntax, and function library for common users to handle GPR data processing. With an appropriate development, it has the ability to adapt to changing research needs. Currently little GPR processing software is written in MATLAB (Witten, A.J., 1999; Conroy and Radzevicius, 2003; Tzanis, A., 2010). In this study, we develop a MATLAB-based, user-friendly GPR data processing and interpretation software packages, called TGPR. The TGPR has the ability to batch process time-lapse GPR surveys, which are repeated GPR surveys at the same location at different times. In addition, with organized structure in the program design, the TGPR has expandable and customizable abilities to meet changing research needs. This chapter describes the programming structure and major function of tis TGPR, and also provides several examples that demonstrate the capacity of the TGPR as compared to commercial GPR software.

### **Program structure**

The TGPR is a two-layered software system, in which the bottom layer consists of functions to process and display the data, while the top layer is user interfaces that organize these functions and streamline the flow of work. Figure 6-1 is the main interface and the entry point of TGPR and the menu items from left to right are the sequence to process and image data. Data importing and management are made through the file menu. Currently, only GSSI radar system is supported. Data processing is through edit, filtering and topo menu. Visualization and interpretation are through 2D radar and 3D radar menu. In each submenu, the process sequence is usually from top the bottom.

Tree view below menu bar demonstrates the data structure (Figure 6-1). Data are organized through the project. Each project can contain several surveys. Each survey can contain one or more survey profiles. Survey is the basic process unit in the TGPR, which means if a survey contains several survey profiles such as grid survey, the same process method will

automatically applied to all the profiles in this survey. Tree view in the left pane also provides entry point to manipulate data in the survey. When the survey name is clicked, the name will appear in the title bar of the main window, indicating data in the survey can be accessed and processed. Usually the project name is the date when the GPR survey is conducted and surveys can be a group of time –lapse data at same location or single survey at different location.

Physically data are store in the hard drive through the structure illustrated in Figure 6-2. Under application program TGPR, the folder GPRProc is working directory which story the processed data and basic information about survey. GPRProc folder contains a project initial file Projects.ini and several folders with name same as the project name in the tree view. Project initial file is text file storing basic information for all the projects created by the program such as project name, date created project and brief description of project. In each project folder, there are an initial file with same name as project name and several folders with same name as survey name. The initial file documented all the surveys in this project. The survey folder contains geometry information about the survey (.ini file) and processed data according to the processing sequence. For example, edit folder stores the processed data using the utilities under edit menu, Top folder stores the processed data using the utilities under Topo correction menu and T3D folder stores three dimensional data.

## **Main features**

### **2D or 3D survey**

The TGPR support both 2D and 3D GPR survey. 2D survey is one single survey line and 3D survey is parallel survey lines in a rectangular area. TGPR assumes both surveys are conducted in the local coordinate system and coordinate information should be provided when project is created. In the 3D survey, The X-axis is the longitudinal direction and the Y-axis is normal to the direction of the X-axis. Z-axis indicates the two travel time of electromagnetic

wave or depth. The parallel survey lines can be at the same direction or zigzag direction. In the current development stage, the interval between survey lines should be the same.

### **Interactively editing**

TGPR provide friendly interface for user to edit the GPR radargram. Figure 6-3A illustrates the interface to edit marker. During a survey, marker errors will occur from a variety of reasons. Tabular data in the top display the basic parameter settings when GPR survey was conducted such as number of samples, number of markers, marker position and time window. These tabular data are used for checking data consistency and potential errors. For example in the 3D survey the number of markers (# marker) of parallel survey lines should be same for all the lines, the tabular data provide the quick overview of markers information for each survey line. In addition, the red triangles in the bottom figure indicate the marker position. The user can interactively insert or delete markers for a particular radargram by mouse clicking and a small window will pop up and provide information about location that marker will be inserted or deleted. After update markers, the marker files which records the marker position will be generated for each survey line and used for interpolation to equal space between markers.

Thermal drift, electronic instability, cable length differences and variations in antenna air gap can cause ‘jumps’ in the air/ground wavelet first arrival, which is usually referred to as the time-zero point (Olhoeft, 2000; Nobes, 1999). Therefore, Time zero adjustment is used to discover the location of the ground surface reflection. TGPR provide interactive way for user to pick up time-zero position using particular criteria such as zero amplitude point or first positive peak. Figure 6-3B demonstrates that the time-zero is picked at 56<sup>th</sup> sample using first positive peak by mouse clicking the corresponding position at 575<sup>th</sup> trace.

The GPR surveys in Shale Hills are usually conducted without survey wheel. Therefore, the number of traces between markers is usually different duo to the variable speed during survey.

Marker interpolation is used to transform data collected in equal-time spacing mode, to data at equal-distance spacing, which means the number of traces between markers will be same

after interpolation. Figure 6-3C demonstrates marker interpolation. Tabular data in the top displays statistics about number of traces between markers and the start and end position of marker.

After reset the number of traces between markers, TGPR will produce equal spacing data as illustrated in the bottom figure.

Other utilities included in edit menu are dc removal, which will remove amplitude drift from zero value by subtract mean amplitude value from each value in the radar traces; devow which removes subsequent decay of low-frequency signal trend present in the data; Time varies gain which multiplied by a gain function combining linear and an exponential coefficients to compensate for amplitude loss due to spreading and attenuation.

#### **Manual or auto topography correction**

Sometimes when GPR surveys were conducted, the elevation data may not be measured. However, the survey operator may have conceptual elevation change in his mind. To reflect this topography change, TGPR provide tools to manually draw the topography with the mouse. Figure 6-4A illustrates manual topography correction by manually draw elevation. On the top of the figure, user can draw the elevation change (Y axis) along the survey line (X axis). Note the value in the Y axis is not the actual elevation data but conceptually reflect relative elevation change. The bottom figure demonstrated topography corrected radargram. In addition, when topography data is collected during GPR survey, the topography data can be directly imported and auto corrected. Figure 6-4B illustrated topography correction using topography data file. Note the topography data file is a text file with three columns delimited by comma. The columns are x, y, and z respectively indicating x, y coordinate and elevation z. The elevation can be relative or absolute as the import option will convert absolute elevations to relative measurements. After import topography file, the elevation change can be previewed on the top and the corrected radargram will be display on the bottom.

## **Filtering**

Filters are generally applied to the data to remove cultural (i.e., human-induced) or system noise and improve the visual quality of the data. Simple filters are often very effective at removing high/low-frequency noise, whilst sophisticated methods are more appropriate for specific problems. However, complex filters may not always be necessary as the filtering process changes the raw data and introduces an element of subjective bias (Basile et al., 2000). In the current stage, TGPR applied three simple filtering. The mean filtering takes the mean of the data across a specified time window and smoothes the data. The median filtering takes the median of the data across a specified time window. The background removal takes the mean of all traces and subtracts it from each trace.

## **2D radar display**

Before 2D display radargram, velocity is estimated by fitting the shape of hyperbola to the hyperbola detected on the GPR radargram. Figure 6-5A showed fitted hyperbola (red line) laying on the observed hyperbola on the radargram. The shape of hyperbola can be changed interactively by sliding the scroll-wheel in the middle of the mouse. The calculated hyperbola is plotted on the radargram using red line. When the fitted hyperbola match well with the observed hyperbola, the velocity can be determined and displayed in the red font.

After velocity is determined, the depth can also be estimated. 2D radargram display with time axis and depth axis is illustrated in Figure 6-5B. Currently TGPR provide 10 predefined color tables. User can select the corresponding color to fit research needs as well as to match particular printer. TGPR also provide an option to pick up anomalies on the radargrams with the mouse and store the locations of these anomalies. For example, the blue dash line in figure indicates a possible layer in radargram. Except for image view of data, TGPR also provide wiggle view of radargram (Figure 6-5C).

### **3D radar Display**

3-D data volumes are generated from parallel 2-D radargrams. The basic idea is extracting data along the z axis (time axis) for all parallel radargrams and then the extracted data is interpolated in the XY plane. Currently TGPR provides two interpolation methods to generate 3D volume. One is Cubic spline interpolation (cubic) and the other is Inverse Distance Interpolation (IDW). Figure 6A illustrates the interpolation used to generate 3D volume. The cell size is used to define resolution of volume. The smaller the cell size is, the finer the volume. However, with cell size decrease, the volume data will increase. In addition, during interpolation TGPR also displays the interpolation results and total time used for interpolation. After interpolation is completed, the volumes can be exported into a 3D data file and displayed in the slice view window.

The slice window controls the 3D data display (Figure 6B). The slice can be viewed in x,y and z direction. The position of these slices can be controlled with the sliders by moving the respective sliders to the appropriate position. 3D data can also be viewed through the cube. By set the x, y and z range the different part of cube can be displayed (Figure 6C). In addition, Color Saturation (contrast) and Translucence can be changed via the increase or decrease buttons. In combination with translucence and Color Saturation, increasing the contrast allows many features to stand out clearly (Figure 6D). The aspect ratio of the axes can be controlled as above, while the viewing angle can be changed with the Azimuth and Elevation sliders or freely adjusted.

### **Examples**

The data from Chapter 5 of this thesis are used as an example to demonstrate the capacity of the TGPR, which is then compared with commercial GPR software called GPR-SLICE (Geophysical Archaeometry Laboratory, Woodland Hills, California). For the Rushtown soil, the grid is 15 by 11 feet (4.5 by 3.7 m survey grid) and for the Weikert soil, the grid is 200

by 70 cm (2 by 0.7 m). The GPR grid surveys conducted under both dry (October 20<sup>th</sup>, 2008) and wet conditions (April 24<sup>th</sup>, 2009) are selected for processing. The data process methods are the same as that described in Chapter 5. Figures 6-7 and 6-8 compare the 2D radargrams processed by the TGPR and the GPR-SLICE, respectively, for two soils under dry and wet conditions. The 2D radargrams processed by the TGPR has very similar patterns with that processed by the GPR-SLICE: With the increasing of soil water content the Bw3- BC interface (cyan dash line) showed more crisscross patterns and hyperbola shapes and the BC-C interface (red dash line) showed more continuous line reflection in the Rushtown soil. In the Weikert soil, the soil-bedrock interface and the weathered-unweathered interface showed a clear line reflection in the GPR radargram during dry period. However, during wet period, the soil-bedrock interface showed intermittent local point reflection.

Figures 6-9 and 6-10 compare another 2D radargrams processed by the TGPR and the GPR-SLICE for the two soils under dry and wet conditions. Although there are some minor differences, the major patterns are similar. For example, in the Rushtown soil, both processed data showed an intermittent linear reflection under dry condition and more strong and continuous reflection under wet condition. In the Weikert soil, both processed data showed a liner reflection above 20 ns under dry condition and more scatter reflection below 20 ns under wet condition. These minor differences may be caused by different GPR processing techniques such as different interpolation methods applied. As an example, when IDW was used for generating slice, some smoothing algorithm is applied in GPR-SLICE (Geophysical Archaeometry Laboratory, Woodland Hills, California, personal communication). As Cassidy (2009) point out, what really matters is that the final interpretation is valid, and although processing is important, ultimately, the key to good data interpretation is good data collection in the first place.

## Summary

As demonstrated in the above description and example, the TGPR provides relatively broad functionality to process, display, and interpret GPR data. Although the program is mainly used to process GSSI radar system (Geophysical Survey Systems, Inc., Salem, New Hampshire), the methods can apply to other GPR vendors.

One motivation for this development is to provide a low cost tool to display and interpret GPR data. With the popularity of the MATLAB in educational and research institutions, the graphical utilities and function libraries the TGPR provides make it easy for common users to generate straightforward GUIs and sophisticated 2D and 3D images.

Another motivation for the development is the flexibility for processing GPR survey data with customized functions. Based on the data structure the TGPR provides, the data can be processed in the batch modes rather than single file, thus greatly facilitating the processing of time-lapsed GPR survey data. The TGPR developed in this study provides an initial framework on which subsequent enhancements and modifications can be made. For instance, currently the TGPR only applies simple filtering, but more advanced filters such as frequency–wave number (FK) filter can be added later for investigating the soil-bedrock interface since this filter suppresses events with particular dip directions (Cassidy, 2009). In addition, with wide application of GPS in GPR surveys, automatic topography correction for GPR radargrams can be made to locate data in its correct spatial context.

## References

- Basile, V., Carrozzo, M.T., Negri, S., Nuzzo, L., Quarta, T. and Villani, A.V. 2000, A groundpenetrating radar survey for archaeological investigations in an urban area (Lecce, Italy). *Journal of Applied Geophysics*. 44:15–32.
- Cassidy, N. J. 2009. Ground penetrating radar data processing, modeling and analysis. In Harry, M.J., Ed. *Ground penetrating radar: theory and applications*. Elsevier Science, Oxford, UK. pp.141-146
- Conroy, J. P. and Radzevicius, S. J. 2003. Compact MATLAB code for displaying 3D GPR data with translucence, *Computers & Geosciences*. 29: 679-681.
- Grandjean, G. and Durand, H. 1999. Radar Unix: a complete package for GPR data processing. *Computers & Geosciences*, 25:141-149.
- Lucius, J.E. and Powers, M.H. 2002. GPR data processing computer software for the PC. USGS Open-File Report 02-166.
- Nobes, D.C. 1999. Geophysical surveys of burial sites: A case study of the Oaro urupa. *Geophysics*. 64: 357–367.
- Oden , C.P. and Moulton, C.W. 2006. GP workbench manual: technical manual, user's guide, and software guide. USGS Open-File Report 2006-1365.
- Olhoeft, G.R. 2000. Maximizing the information return from ground penetrating radar. *Journal of Applied Geophysics*. 43:175–187.
- Tzanis, A. 2010. matGPR Release 2: A freeware MATLAB® package for the analysis & interpretation of common and single offset GPR data. *FastTimes*, 15:17 – 43
- Witten, A.J. 2002. Geophysica: MATLAB-based software for the simulation, display and processing of near-surface geophysical data. *Computers & Geosciences*, 28: 751–762.

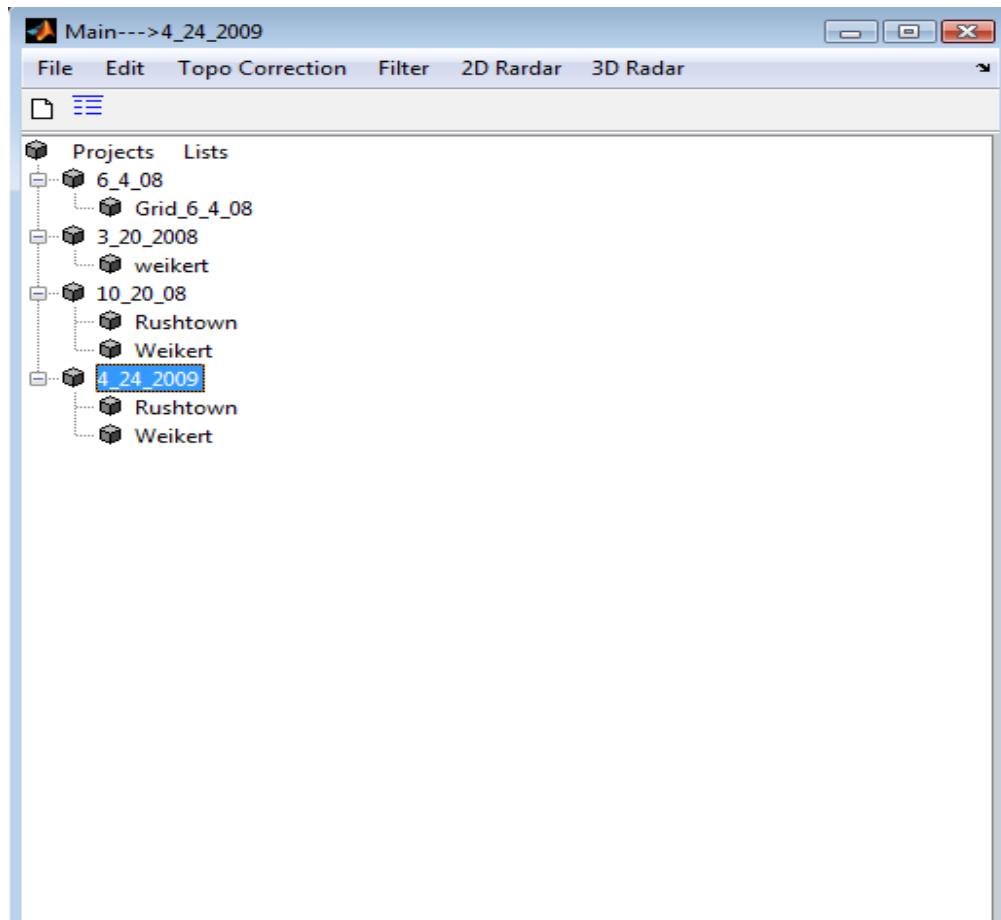


Figure 6-1: Main interface and the entry point of TGPR and data organization in the tree view

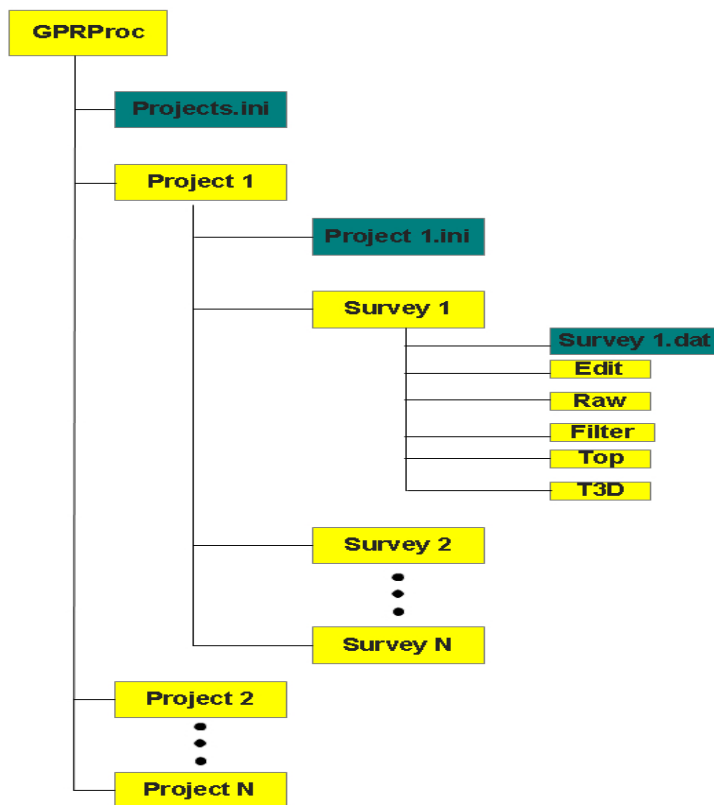
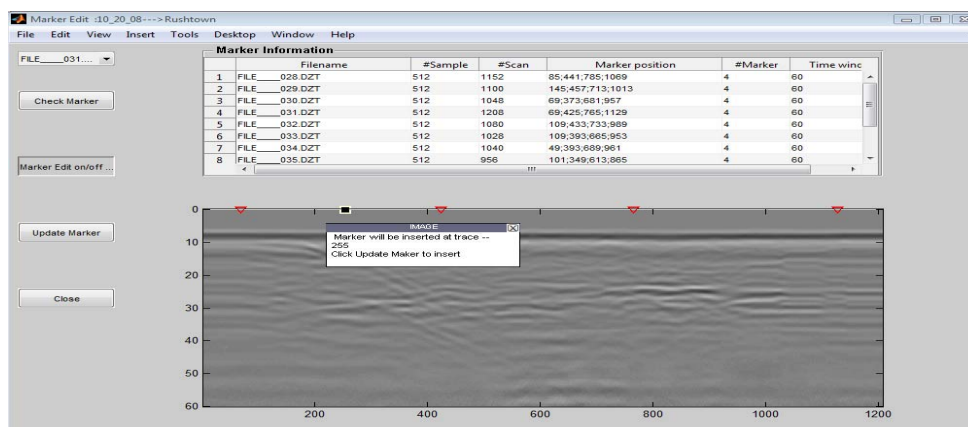
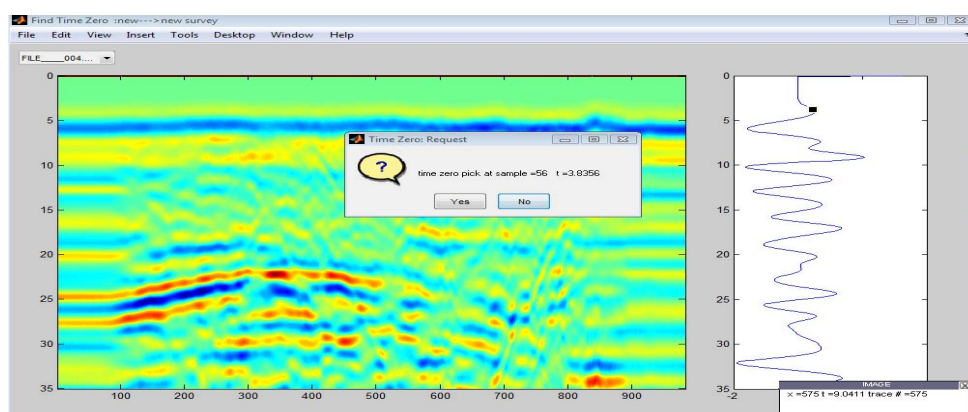


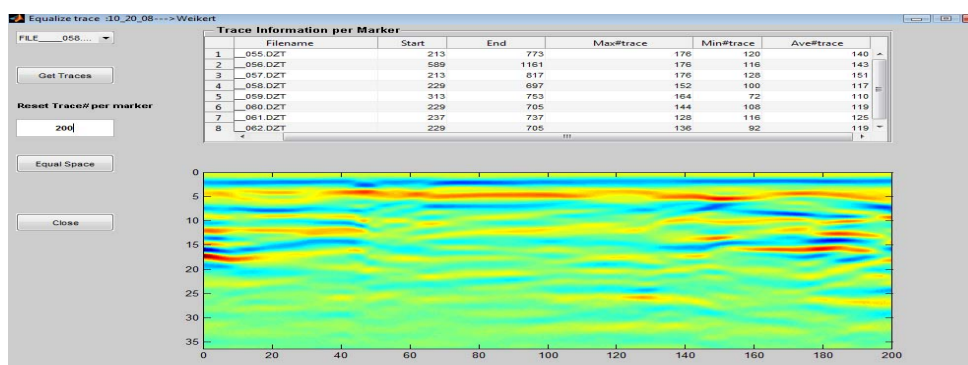
Figure 6-2: Physical data structure in the hard drive. (Yellow color indicates the folder, dark green color indicate information file about project, survey and survey geometry)



A

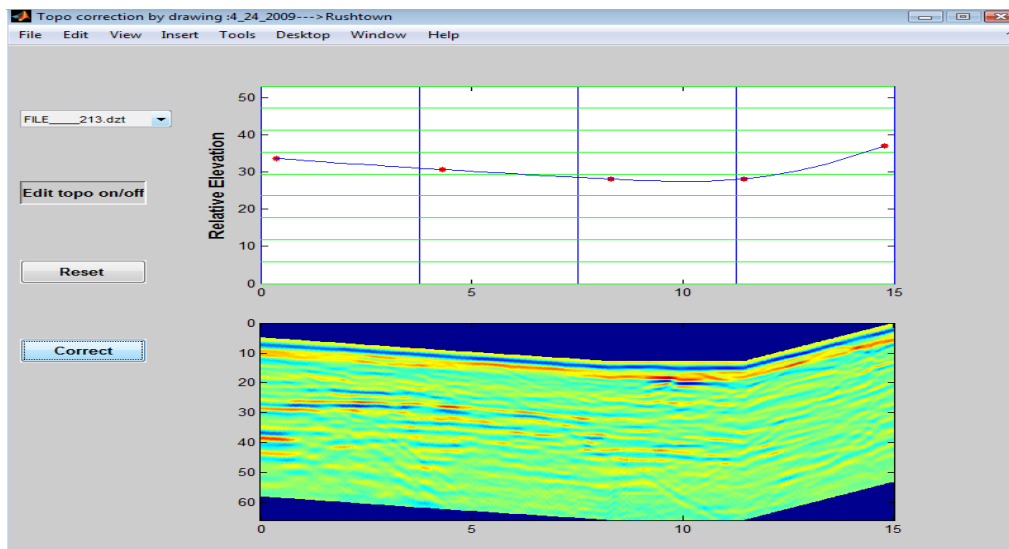


B

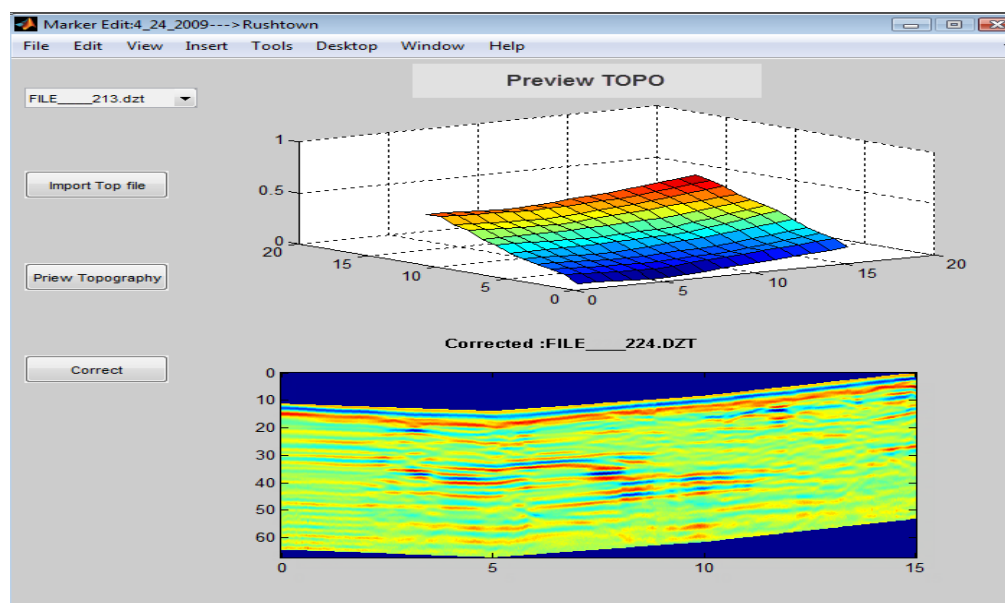


C

Figure 6-3: A. GUI of marker edit displaying marker information and interactively adding marker B. GUI of time zero adjustment displaying time zero pick at first positive peak C. GUI of marker interpolation displaying trace information and radargram after interpolation

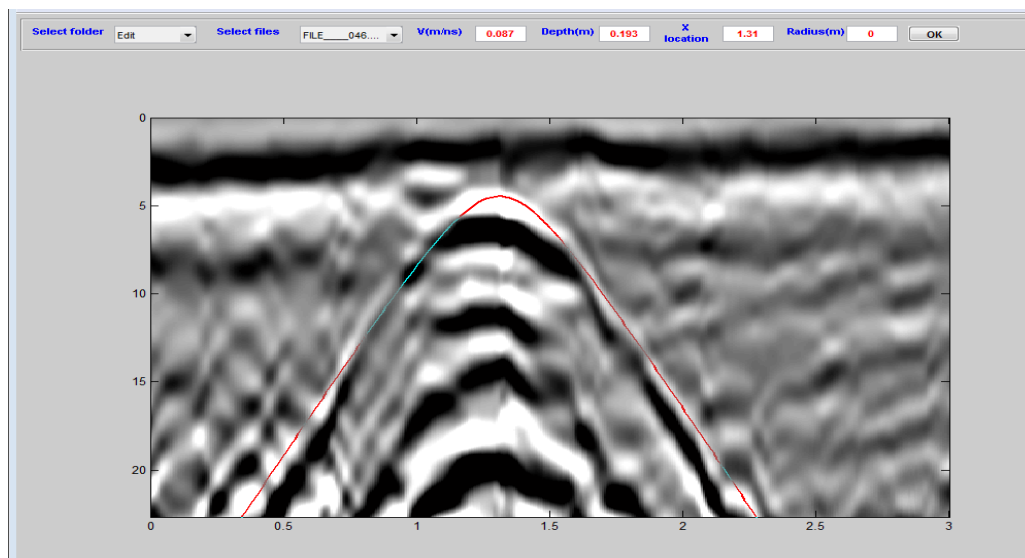


A

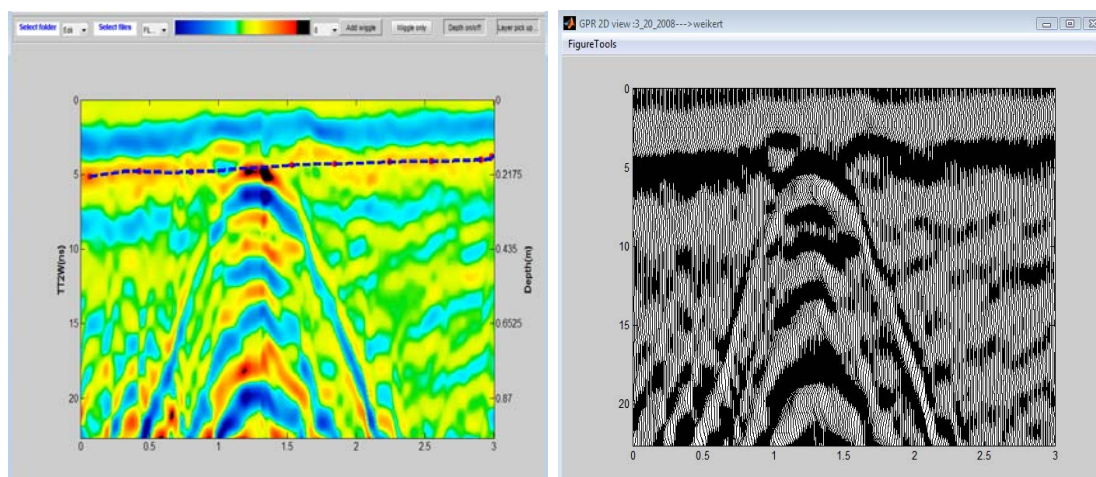


B

Figure 6-4: A. manual topography correction by drawing relation elevation line  
 B. automatic topography correction by importing topography data file



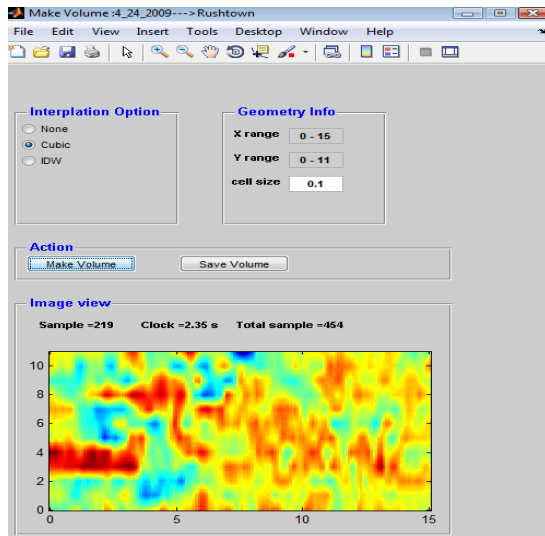
A



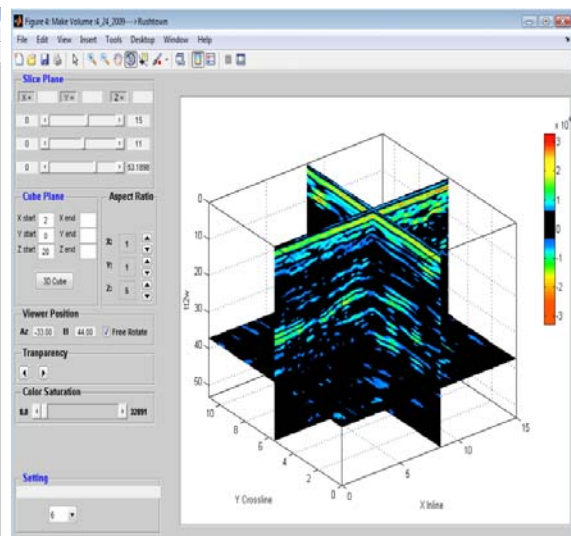
B

C

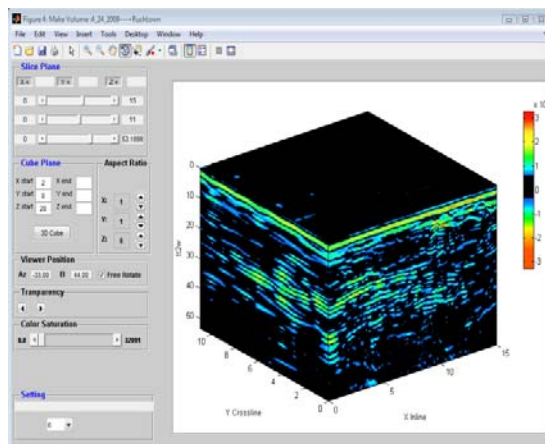
Figure 6-5: A. Interactive fitting of a diffraction hyperbola (red lines) with observed hypobola and velocity is displayed in red font. B. color display radargram with time axis and depth axis and the blue dash line indicate the presence of layer. C. wiggle display of radargram



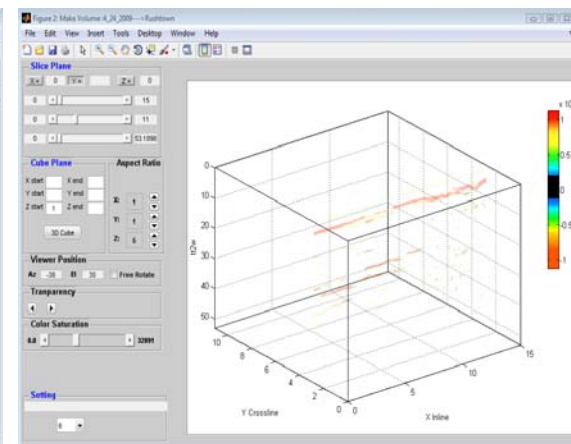
A



B



C



D

Figure 6-6: A. snap shot of interpolation along x-y plane  
 B. slice view along x,y and z direction  
 C. cube view of 3D data  
 D. slice view with increase color saturation and transparency

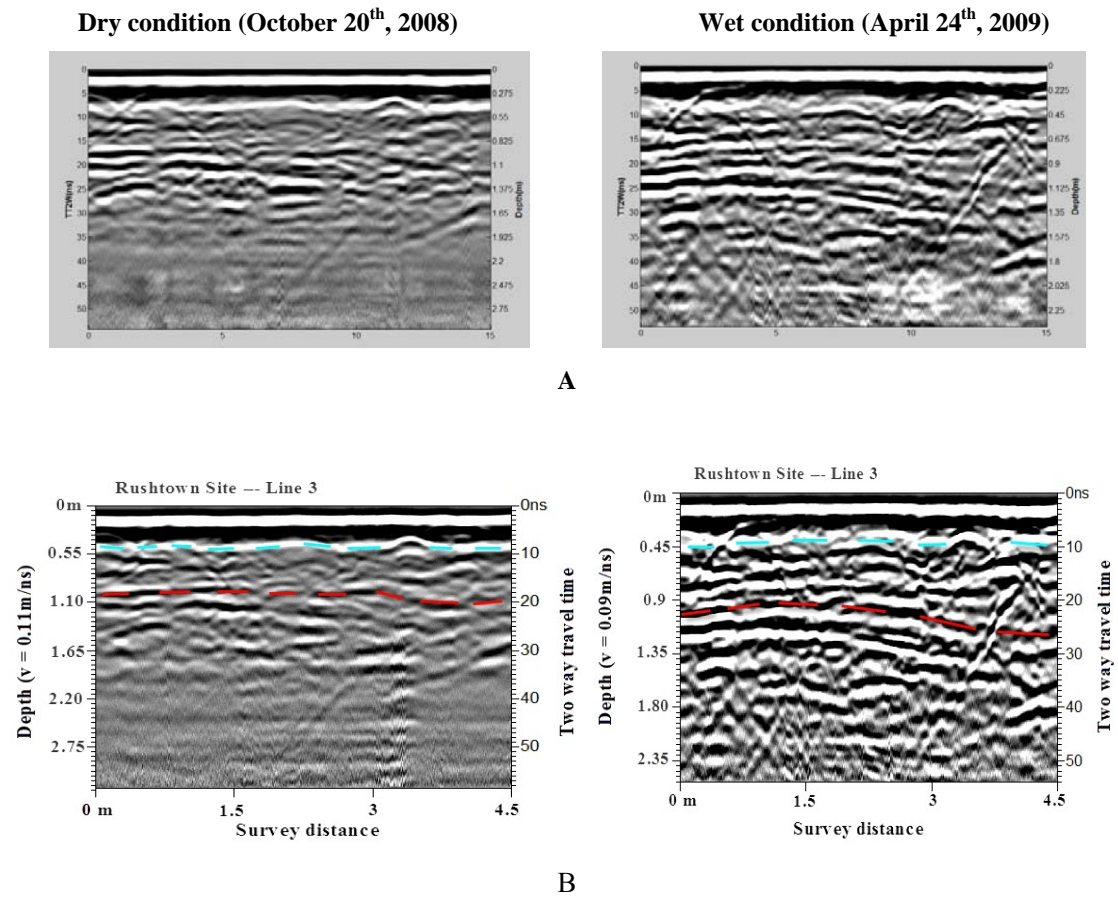


Figure 6-7: A. 2D radargrams of the Rushtown soil processed by the TGPR under dry and wet conditions; B. 2D radargrams of the Rushtown soil processed by the GPR-SLICE under dry and wet conditions (cyan dash line indicates the Bw3-BC interface and red dash line indicates the BC-C interface)

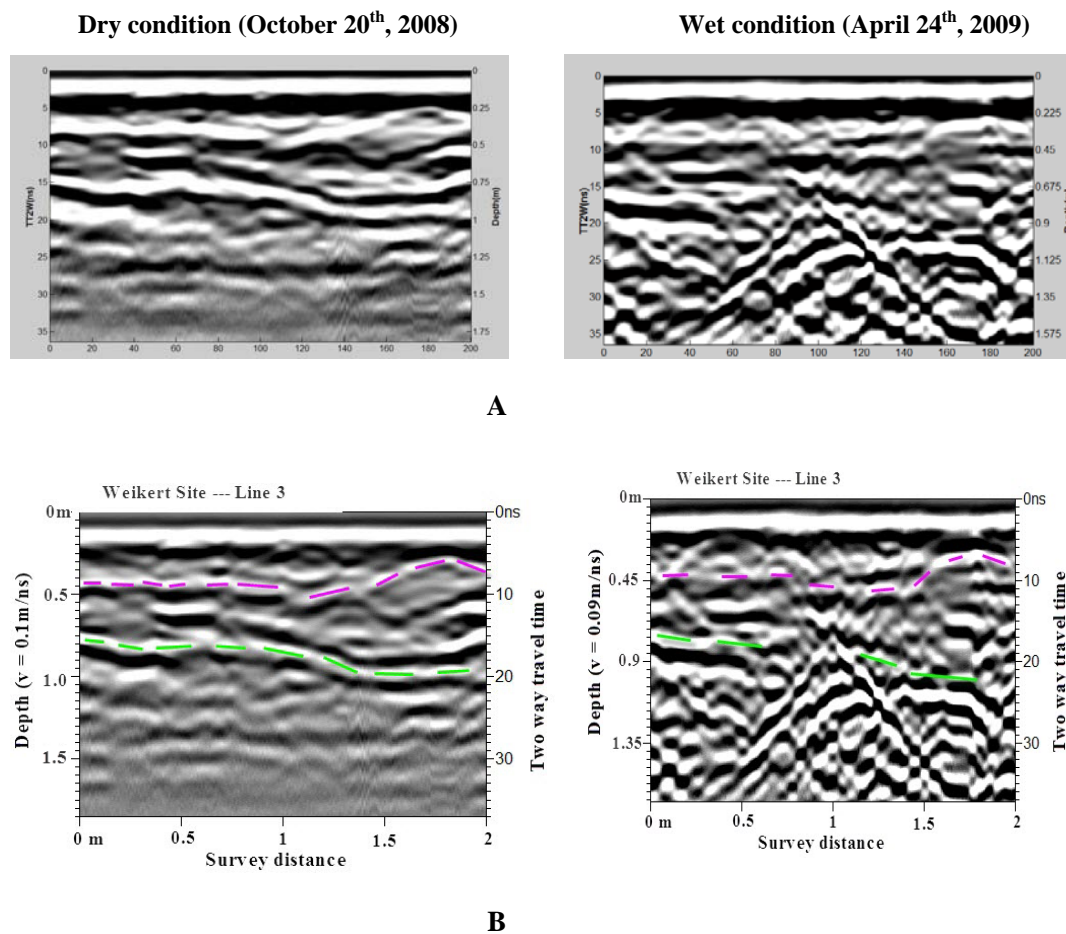
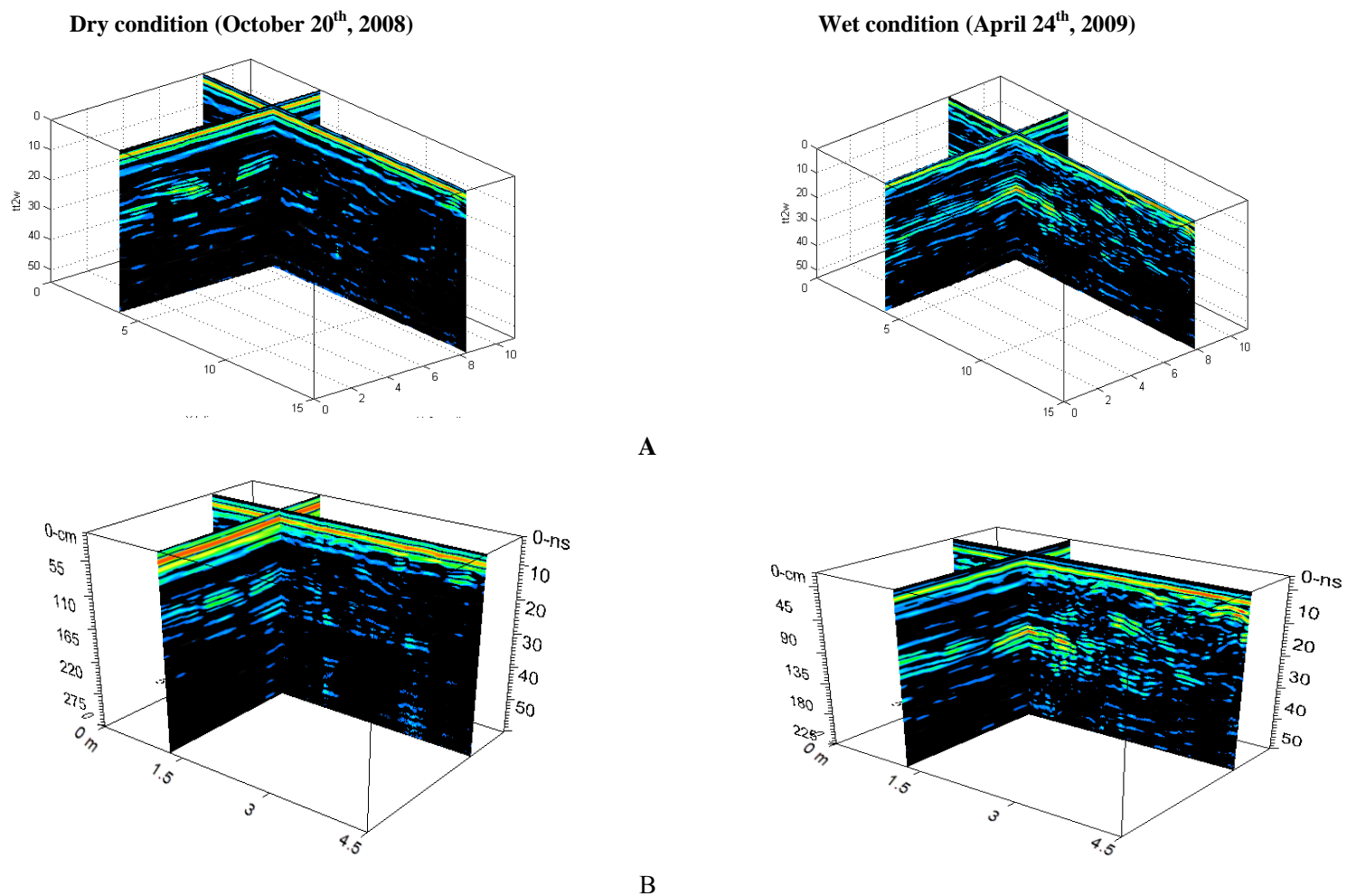


Figure 6-8: A. 2D radargrams of the Weikert soil processed by the TGPR under dry and wet condition. B. 2D radargrams of the Weikert soil processed by the GPR-SLICE under dry and wet condition (pink dash line indicates the soil-bedrock interface and green dash line indicates the weathered-unweathered rock interface)



**Figure 6-9:** A. 3D slice view of the Rushtown soil processed by the TGPR under dry and wet condition. B. 3D slice view of the Rushtown soil processed by the GPR-SLICE under dry and wet condition

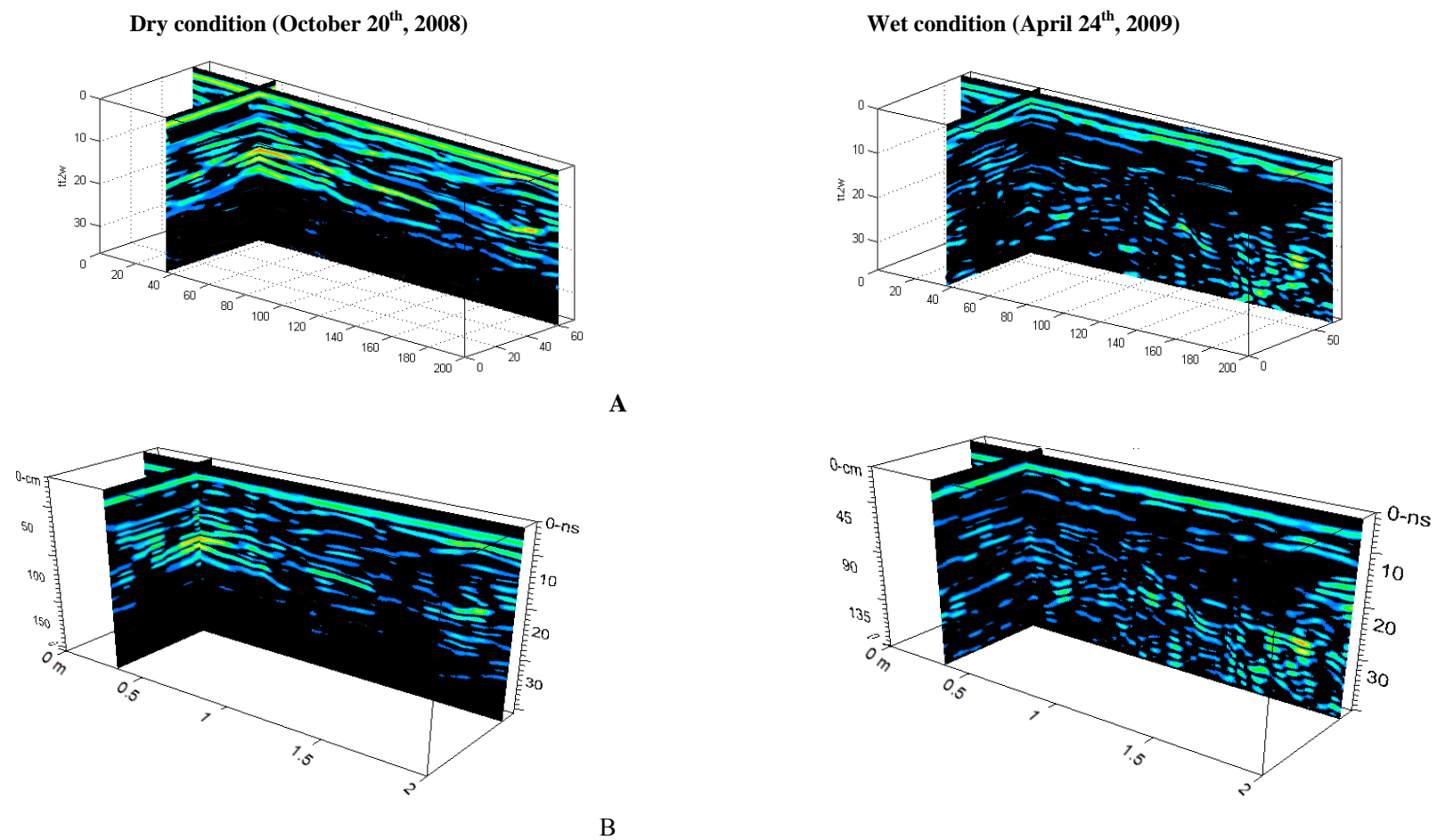


Figure 6-10: A. 3D slice view of the Weikert soil processed by the TGPR under dry and wet condition B. 3D slice view of the Weikert soil processed by the GPR-SLICE under dry and wet condition.

## **Chapter 7**

### **Overall Summary and Future work**

#### **Overall Summary**

The main goal of this study was to develop an integrated approach to combine hydrologic and geophysical data to elucidate the spatial and temporal patterns of subsurface flow in the Shale Hills Critical Zone Observatory (CZO). Extensive soil hydrologic monitoring and GPR surveys have been conducted in the past several years to investigate subsurface features, soil heterogeneity, hydrologic processes, and soil moisture patterns. Real-time high temporal resolution soil moisture monitoring data were used to identify the occurrence and frequency of subsurface lateral flow and seasonal soil moisture changes at the point scale where soil moisture sensors were installed. High spatial resolution GPR surveys provided spatial patterns of subsurface features and related flow pathways at the hillslope scale where continuous GPR scans were made.

The direct evidence of subsurface lateral flow was identified by comparing the storage change at each soil horizon and profile with rainfall inputs. It was found in this study that subsurface lateral flow was ubiquitous in all of the monitored sites. The active layers that favored the formation of preferential pathways were also identified and showed variation among different hillslope sites with different soil types. The occurrence of subsurface lateral flow showed seasonality and threshold behavior. Using the occurrence of subsurface lateral flow at the valley floor site as an indicator of hydrologic connectivity from the hilltop to the valley floor, the contribution of subsurface lateral flow to stream runoff were evaluated.

Time-lapse GPR surveys were combined with real-time soil moisture monitoring to identify subsurface flow pathways in two contrasting soil transects. The real-time soil moisture data were used to analyze subsurface flow processes and explain the observed GPR radargrams. Different conceptual models were compared in GPR simulations. By comparing simulated radargrams with the observed, the best matched pattern in radargram was used to confirm flow process. In the shallow Weikert soil with relatively steep slope, subsurface lateral macropore flow was dominant; whereas in the deep Rushtown soil with relative flat surface, a combination of vertical macropore flow and lateral matrix flow was dominant.

Seasonal GPR surveys in two hillslopes with different soil types were conducted during dry to wet periods. Even at the same location, the GPR reflection patterns showed seasonality. In the deep Rushtown soil, the reflection at the BC-C interface became clearer from dry to wet conditions. While in the shallow Weikert soil, the reflection at the weathered-unweathered interface become less clear from dry to wet conditions. The real-time soil moisture data were used to help explain the seasonal GPR signal changes and to infer hydrologic flow paths in the two soils. It was found that, under wet condition, rainwater tended to infiltrate into the fractures of the underlying bedrock in the shallow Weikert soil and moved downslope, which then recharged the deeper portion of the Rushtown soil. The seasonal GPR signal changes also suggest an optimal time for using GPR to detect soil layers: Wet condition without rainfall event is optimal time for detecting the BC-C interface in the Rushtown soil, while dry condition is optimal time for detecting the soil-bedrock and the weathered-unweathered interfaces in the Weikert soil.

The MATLAB-based software TGPR developed in this study is an alternative to commercially expensive software to process, display, and interpret GPR data. The TGPR can process both 2D and 3D GPR survey data and has the ability to batch process GPR survey data containing several profiles. With user friendly interfaces, the TGPR can interactively edit radargrams and manually or automatically correct topography. The TGPR also provides several utilities to enhance 2D and 3D visualization of GPR data, including 1) trace view, wiggle view,

and image view of 2D data, 2) slice view, cube view, and transparent view of 3D data, 3) ten built-in color tables to enhance image display, and 4) layer editing of 2D images.

### **Future Work**

Based on the investigations and findings of this study, the following are some suggested future research needs to further advance our understanding of landscape-soil-hydrology relationships across space and time:

1. The GPR surveys conducted in this study have mostly focused on small areas to reveal soil hydrologic processes. To understand complex subsurface across the catchment and to guide spatially-distributed hydrologic modeling, larger area surveys and/or the connection of small area surveys are needed;

2. The soil moisture analysis conducted in this study has focused on revealing the occurrence of subsurface lateral flow and the hydrologic connectivity in one concave hillslope. The 3D drainage flux needs to be further analyzed across space and time to quantify the contribution of various hillslopes (concave, convex, and planar) across the catchment to the stream discharge;

3. The soil moisture and GPR databases developed in this study have focused mostly on data management and display, but lack tools for analysis. An integrated hydrologic information system needs to be developed that can allow the analysis and modeling of the hydrologic and geophysical data;

4. The MATLAB-based GPR processing software developed in this study can be further enhanced to incorporate GPS in GPR surveys so that automatic topography correction for GPR radargrams can be made to locate data in correct spatial context.

# Vita

**Jun Zhang**

## EDUCATION

- Ph.D. in Soil Science  
Penn State University, University Park, PA 2011  
Dissertation: Integrated Approach to Identifying Subsurface lateral Flow in A Forested Catchment  
Advisor: Dr. Henry Lin
- M.S. in Soil Physics  
Institute of Soil Science, CAS (Chinese Academy of Science), Nanjing, China 2003  
Thesis: Application Inverse Method to Determine Soil Hydraulic Properties  
Advisor: Dr. Shaohui Xu
- B.S. in Agricultural Environment Protection  
Huazhong Agriculture University, Wuhan, China 2000

## PUBLICATIONS

- Zhang, J., Lin, H.S. and Doolittle, J., 2011. Seasonal GPR signal changes in two soil and hillslopes. *Geoderma* (in review).
- Zhang, J. and Lin, H.S., 2011. Subsurface lateral flow in the shale hills catchment as revealed by real-time soil moisture monitoring. *Journal of hydrology* (in review).
- Zhang, J., Lin, H.S. and Doolittle, J., 2010. Subsurface Lateral Flow as Revealed by Combined Ground Penetrating Radar and Real-Time Soil Moisture Monitoring. *Hydrological Processes* (in revision).
- Zhang, J., Xu, S., Liu, J., Zhang, J., Fan, X., 2007. Simulation of rice yield and nitrogen uptake using ORYZA 2000 (in Chinese). *Soils*. 39, 428-432
- Zhang, J., Xu, S., Liu, J., Zhang, J., 2006. Advance in modeling nitrogen cycling in farmland ecosystem. *Journal of irrigation and drainage* (in Chinese). 25, 85-88.